

# Carnegie Mellon University

## CARNEGIE INSTITUTE OF TECHNOLOGY

### THESIS

SUBMITTED IN PARTIAL FULFILLMENT OF THE REQUIREMENTS

FOR THE DEGREE OF Doctor of Philosophy

TITLE The Phosphorus Reaction in Oxygen Steelmaking: Thermodynamic  
Equilibrium and Metal Droplet Behavior

PRESENTED BY Andre N. Assis

ACCEPTED BY THE DEPARTMENT OF

Materials Science and Engineering

Richard J. Fruehan 8/15/14  
ADVISOR, MAJOR PROFESSOR DATE

Sridhar Seetharaman 8/19/14  
ADVISOR, MAJOR PROFESSOR DATE

Gregory S. Rohrer 9/03/14  
DEPARTMENT HEAD DATE

APPROVED BY THE COLLEGE COUNCIL

Vijayakumar Bhagavatula 9/12/14  
DEAN DATE

# **The Phosphorus Reaction in Oxygen Steelmaking: Thermodynamic Equilibrium and Metal Droplet Behavior**

Carnegie Mellon University  
Department of Materials Science and Engineering  
Pittsburgh, Pennsylvania

Andre N. Assis, Ph.D. Candidate

Professor Richard J. Fruehan, Advisor  
Professor Sridhar Seetharaman, Advisor

August 15, 2014



## Abstract

Low phosphorus content steels are essential for steel applications where high ductility is required, such as thin sheets, deep drawn, pipelines and automobile exteriors. In the past, phosphorus control was not considered a big challenge in steel production in the US because iron ores with low phosphorus contents were readily available and considered cheap. However, in the last decade, the iron ore price has risen by roughly 400% and lower cost iron sources generally have higher phosphorus content. In integrated steel plants, phosphorus removal usually takes place during the oxygen steelmaking process (OSM) but in Japan a intermediate step for hot metal dephosphorization is commonly used. There are various types of OSM furnaces but the most widely used remains the top-blown Basic Oxygen Furnace (BOF). The BOF slag can be recycled to a sinter plant or directly to the blast furnace, ultimately increasing the phosphorus input in the process. In order to meet new demands for phosphorus control, it is necessary to improve our understanding on the thermodynamics and kinetics of the phosphorus partitioning reaction between slag and metal melts during steelmaking. Therefore, the present work has been divided in three strongly correlated sections: phosphorus equilibrium between metal and slag; analysis of plant data; and observations of the reaction kinetics.

Phosphorus equilibrium between liquid metal and slag has been extensively studied since the 1940's. It is well known that  $\text{CaO}$  and  $\text{FeO}$  are the main slag constituents that help promote dephosphorization. On the other hand, dephosphorization decreases with temperature due to the endothermic nature of the reaction. Many correlations have been developed to predict the phosphorus partition ratio as a function of metal and slag composition as well as temperature. Nevertheless, there are



still disagreements in the laboratory data and the equilibrium phosphorus partition can be predicted with an uncertainty of a factor of up to 5. The first part of the present work focuses on generating more reliable equilibrium data for BOF-type slags by approaching equilibrium from both sides of the reaction. The experimental results were combined with two other sets of data from different authors to produce a new correlation that includes the effect of  $\text{SiO}_2$  on the phosphorus partition coefficient,  $L_P$ .

Although the quantification of phosphorus equilibrium is extremely important, most industrial furnaces do not operate at equilibrium, usually due to liquid slag formation, kinetics and time constraints. Thus, it is important to know how close to equilibrium different furnaces operate in order to suggest optimal slag compositions to promote dephosphorization. The present work analyzed four large sets of data containing the chemical compositions of both slag and metal phase as well as the tapping temperature of each heat. Each set of data corresponded to different furnaces: one AOD (Argon Oxygen Decarburization), two top-blown BOFs and one Q-BOP or OBM. It was found that the bulk slag composition can greatly “mask” the data due to solid phases coexisting with the liquid slag. The author used the software package FactSage to estimate the amount of solids in the slag and liquid slag composition. It was found that the AOD is the reactor closest to equilibrium, followed by the Q-BOP (OBM) and the two top-blown BOFs. It was noted that the stirring conditions and slag composition are two key variables to enable optimum phosphorus removal. Also, over saturating the slag with CaO and MgO does not seem to benefit the process to any extent.

Lastly, interesting observations on the behavior of small metal droplets reacting with slag are presented and discussed. It was found that dynamic interfacial phenomena at the metal-slag interface is likely to play a significant role in the kinetic

behavior of the system, due to the exchange of surface active elements, such as oxygen, which dramatically lowers the interfacial tension and cause spontaneous emulsification. Although this phenomenon has been studied, actual quantification of changes in interfacial area remain a challenge. The author developed an experimental method to enable better quantification of spontaneous emulsification and two sets of experiments were carried. One with an Fe containing 0.2 wt.% P and another in a P-free system where pure iron was oxidized. It was found that phosphorus did not play a role in spontaneous emulsification and it was rapidly removed before the onset of dynamic interfacial phenomena. Emulsification was maybe caused by de-oxidation of the metal after phosphorus removal took place and the metal became super saturated with oxygen by an unknown reason. The estimated surface area rapidly increases by over an order of magnitude during the beginning and intermediate periods of the reaction. The metal drop breaks into hundreds of small droplets, effectively emulsifying the metal into the slag. With time, the surface area decreases and the metal droplets coalesce. Similar results were observed for an Fe droplet being oxidized. Spontaneous emulsification takes place regardless of the direction of oxygen transfer and the changes in surface area are similar for both cases.

The last chapter describes the industrial relevance of the present work, summarizes the findings, revisits the hypotheses and presents potential future work where further research is encouraged.



## Acknowledgments

If someone asked me, back in 2009, if I would ever consider doing a PhD, I would have probably responded “no”. Now that 4 years have passed, every time someone asks me “*Should I pursue a PhD?*”, my answer is always a resounding “yes!”.

Well, isn’t it a bit funny how things turned out to be?

I have had the honor to work with two of the most brilliant and inspiring people I have ever met, my two advisors: Professor Richard J. Fruehan and Professor Sridhar Seetharaman. I am deeply grateful for your invaluable guidance and support. Thank you Professor Fruehan, for the history lessons on steelmaking, for the phone calls on Sunday morning and for all our fruitful discussions. Thank you Professor Sridhar, for suggesting innovative approaches, for the long Skype calls and for the Christmas parties at your house. What an honor it has been to work with both of you!

I am great appreciative for the Center for Iron and Steelmaking Research (CISR) and its industry members for their funding, interest and valuable insight on this project. This work would not be possible without their support.

I would also like to thank my thesis committee: Professor Chris Pistorius, also known as my *step-advisor*, for his willingness to help, for the valuable discussions and suggestions and for signing several order forms whenever Professor Fruehan was not around; Dr. Eugene Pretorius for the continued interest, support and input on this project since the beginning; And Professor Bryan Webler, for the brief, but interesting, discussions on new projects and ideas. Thank you all for your time and input on this project.

Special thanks to Mr. Jason Warnett, Mr. Stephen Spooner and Professor Mark Williams from The University of Warwick WMG for their key contributions on the XCT measurements and calculations.

I also want to share my deep gratitude for Professor David Laughlin, for great discussions on thermodynamics, for welcoming me to his group meetings and for providing huge amounts of pizza during these joyful weekly reunions.

To all the wonderful staff and faculty at the MSE Department, specially Roxann Martin, Jeanna Pekarcik, Angela Pusateri, Suzanne Smith, Amy Watts, Jason Wolf, Tom Nuhfer and Adam Wise. Thank you for all the countless times you were there to help.

I cannot forget all the wonderful MSE friends, colleagues and labmates: Prof. Jinxi Wu, Dr. Tetsuya Kaneko, Dr. Neerav Verma, Dr. June Bott, Dr. Erica Sampson, Carolyn Norwood, Dr. Stephanie Bojarski, Vignesh Sundar, Aditya Balasubramanian, Dr. Jiwon Park, Mohammed Tayeb, David Gildemeister, Aswin Tejasukmana, Daniel Shafrir and Alex Zwiren for all the help, night outs, great conversations about extremely relevant topics and everything else. This experience would never be the same without you.

I must thank my first mentor, Dr. Ronaldo Sampaio, for provoking me to pursue graduate school. Which would sequentially promote the happiest day of my life: my wedding. Thank you Prof. Ronaldo for believing and supporting my journey.

To all my Pittsburgh Brazilian friends, now considered family, for making the weekend days something to look forward for. The endless brazilian barbecues during summer, the wine nights during the winter and for simply being around and makeing me feel at home. Rodrigo, Fernanda, Luca, Idário, Soraya, Vinícius, Artur, Chris, Patrick, Mariana, Antônio, Rosa, João, Amanda, Fran, Curtis, Thomas, Telmo, Lu e Jennifer. You guys are the best.

To my parents, Carlos and Luiza, and my brother, Lucas, for the infinite support on this specific journey and basically since birth. There are no words to describe my eternal gratitude. You are the best family I could ever have. I love you all!

And finally, to my wife, Karina Assis, to whom I dedicate this work to. You gave me your hand, closed your eyes and said “*Let’s go*” leaving all the “*what if’s*” behind you and taking this leap of faith with me. Without you by my side none of this would have happened. You are my foundation and my strength. Eu te amo!

# Contents

<b>1</b>	<b>Introduction</b>	<b>1</b>
1.1	The Oxygen Steelmaking Process . . . . .	1
1.1.1	Historic Review of Modern Steelmaking Processes . . . . .	3
<b>2</b>	<b>Motivation</b>	<b>8</b>
<b>3</b>	<b>Technical Background</b>	<b>12</b>
3.1	The Phosphorus Reaction and Thermodynamic Equilibrium . . . . .	12
3.2	Phosphorus Refining in BOF Operation . . . . .	19
3.2.1	Overview of Typical Top-Blown BOF Operation . . . . .	20
3.2.2	Slag Formation Duration Oxygen Blow . . . . .	21
3.2.3	The Dephosphorization Mechanism in Oxygen Steelmaking . .	25
3.3	Kinetics of Phosphorus Removal . . . . .	29
<b>4</b>	<b>Objectives and Hypotheses</b>	<b>41</b>
<b>5</b>	<b>Phosphorus Equilibrium Between Liquid Iron and CaO-MgO-SiO<sub>2</sub>-FeO-P<sub>2</sub>O<sub>5</sub> Slags</b>	<b>42</b>
5.1	Introduction . . . . .	42
5.2	Technical Approach . . . . .	45

5.2.1	Raw Materials . . . . .	46
5.2.2	Furnace . . . . .	48
5.2.3	Crucible Selection . . . . .	50
5.2.4	Experimental Procedure . . . . .	51
5.3	Results . . . . .	56
5.3.1	Visual Observations . . . . .	59
5.3.2	Chemical Analysis Results . . . . .	59
5.4	Discussion . . . . .	62
5.4.1	Chemical Analysis Estimate and Correction . . . . .	62
5.4.2	Equilibrium Phosphorus Partition . . . . .	68
5.4.3	MgO Saturation . . . . .	83
5.4.4	Development of a New Correlation . . . . .	87
<b>6</b>	<b>Plant Data Analysis</b>	<b>94</b>
6.1	Introduction . . . . .	94
6.2	Technical Approach . . . . .	94
6.3	Results . . . . .	96
6.4	Discussion . . . . .	108
6.4.1	Impact of Dicalcium Silicate on Lp . . . . .	113
6.4.2	Summary of this chapter . . . . .	119
<b>7</b>	<b>Studies on Spontaneous Emulsification</b>	<b>122</b>
7.1	Introduction . . . . .	122
7.2	Technical Approach . . . . .	124
7.2.1	Raw Materials . . . . .	125
7.2.2	The Confocal Scanning Laser Microscope . . . . .	127
7.2.3	Experimental Procedure . . . . .	129



7.2.4	X-Ray Computed Tomography . . . . .	131
7.2.5	Chemical Analysis . . . . .	134
7.3	De-P Results . . . . .	135
7.3.1	3D Images . . . . .	135
7.3.2	Surface Area and Volume Measurements . . . . .	135
7.3.3	Chemical Analysis . . . . .	137
7.4	Oxidation Results . . . . .	141
7.4.1	3D Images . . . . .	141
7.4.2	Surface Area and Volume Measurements . . . . .	142
7.5	Discussion . . . . .	143
7.5.1	Dynamic Changes in Surface Area . . . . .	143
7.5.2	The Theories . . . . .	147
7.5.3	Volume Measurements . . . . .	167
7.5.4	Coalescence of Emulsion . . . . .	168
<b>8</b>	<b>Industrial Relevance, Conclusions and Potential Future Work</b>	<b>172</b>
8.1	Industrial Relevance of the Present Work . . . . .	172
8.2	Summary and Conclusions . . . . .	174
8.2.1	Phosphorus Equilibrium Between Liquid Iron and CaO-MgO-SiO <sub>2</sub> -FeO-P <sub>2</sub> O <sub>5</sub> Slags . . . . .	174
8.2.2	Plan Data Analysis . . . . .	175
8.2.3	Studies on Spontaneous Emulsification . . . . .	175
8.3	Hypotheses Revisited . . . . .	176
8.3.1	Phosphorus Equilibrium . . . . .	176
8.3.2	Plant Data . . . . .	177
8.3.3	Emulsification . . . . .	178

8.3.4	Potential Future Work . . . . .	178
-------	---------------------------------	-----

# List of Tables

1.1	Typical Hot Metal Composition. . . . .	2
1.2	Typical BF Slag Composition. . . . .	2
3.1	Example of Oxygen Batches in a BOF. [1] . . . . .	21
5.1	Chemical composition of the master alloy MA2. . . . .	47
5.2	Target and Final Master Slag Composition. . . . .	47
5.3	Calculated initial slag and metal compositions. . . . .	58
5.4	Reported values from chemical analysis for slag and metal. Species marked with “—” were not analyzed. . . . .	61
5.5	Corrected equilibrium chemical composition. Values with * are esti- mated based on the assumptions discussed in the text. . . . .	64
5.6	Average and standard deviation for P analysis in the metal. . . . .	66
5.7	Analysis results for an alloy containing more than 20ppm using ICP- MS, ICP-OES and GD-MS. . . . .	66
5.8	Analysis results for an alloy containing less than 20ppm using ICP-MS and ICP-OES. . . . .	67
5.9	Range of Slag Compositions Studied by the author and Tayeb. [2] . . .	71
5.10	$L_P$ and (T.Fe) data for regions 1, 2 and 3 from Figure 5.12. . . . .	73

5.11	Example calculation of how FeO impacts $L_P$ for dephosphorization and rephosphorization. . . . .	80
5.12	Change in $L_P$ due to furnace cooling at $-35^{\circ}\text{C}/\text{min}$ . . . . .	83
5.13	Change in $L_P$ due to furnace cooling at $-12^{\circ}\text{C}/\text{min}$ . . . . .	83
5.14	Change in $L_P$ with 5 wt.% increase in $\text{SiO}_2$ content. . . . .	90
6.1	Average, Minimum and Maximum Turndown Temperatures for AOD, Q-BOP or OBM, BOF 1 and BOF 2. . . . .	96
6.2	Number of heats for each reactor where CaO and MgO solid solutions (S.S.) were predicted as solid phases by FactSage. . . . .	97
6.3	Number of heats for each reactor where $2\text{CaO}.\text{SiO}_2$ was predicted as solid phase by FactSage. . . . .	97
6.4	Average chemical composition data for the steel and the slag for AOD, Q-BOP, BOF 1 and BOF 2. . . . .	100
7.1	Chemical Composition of the Master Slag Used for Kinetics Experiments.	126
7.2	Chemical composition of low oxygen master alloy. . . . .	126
7.3	Chemical Composition of the Phosphorus-free slag used in the oxidation experiments. . . . .	126
7.4	Temperature calibration data for CSLM. . . . .	129
7.5	XCT scanning parameters. . . . .	134
7.6	Raw data for surface area measurements. . . . .	137
7.7	Raw data for volume measurements. . . . .	137
7.8	Chemical analysis results for P and O using different techniques. . . .	138
7.9	WDS results and scan parameters. . . . .	139
7.10	Phosphorus content results from LA-ICPMS for 20s sample. . . . .	140
7.11	Oxygen content results from SIMS for 20s sample. . . . .	140

7.12	Surface area measurements for oxidation experiments. . . . .	142
7.13	Volume measurements for oxidation experiments. . . . .	143
7.14	Results for RHS of Equation 7.5. . . . .	153
7.15	Diffusion coefficient based on mass transfer. . . . .	154
7.16	WDS results for Self De-P experiments . . . . .	165

# List of Figures

1.1	Overview of the steelmaking process. [3]	3
1.2	Diagram of Bessemer vessel. Reproduced from [1].	4
1.3	Diagram of a top-blown BOF. Reproduced from [1].	6
1.4	Diagram of Open Hearth Process. Reproduced from [1].	7
1.5	Diagram of a bottom-blown BOF. Reproduced from [1].	7
2.1	Price history of dry metric ton of iron ore. [4]	9
2.2	Different BF-OSM routes. In blue hot metal pretreatment is used. In purple the OSM slag is recycled directly to the blast furnace. In green the OSM slag is recycled to a sinter plant and then the sinter is charged on to the blast furnace.	10
3.1	Change in metal composition during blowing. Reproduced from [1].	22
3.2	Change in slag composition during blowing. Reproduced from [1].	23
3.3	Different phosphorus removal profiles observed by [5]. Reproduced from [5].	27
3.4	Changes in droplet generation at different lance heights. [5]. Reproduced from [5].	28
3.5	Dephosphorization data from experiment 18. Reproduced from [6].	34

3.6	Diagram of both experimental setups used by Gaye et al. [7]. Reproduced from [7]. . . . .	36
3.7	Effect of oxygen activity on the equilibrium interfacial tension of different Fe-based alloys and slags at 1600°C. Dashed line for CaO-SiO <sub>2</sub> -FeO from [8]. Reproduced from [7]. . . . .	39
3.8	Interfacial tension as a function of time for Fe-Al alloy in CaO-Al <sub>2</sub> O <sub>3</sub> -SiO <sub>2</sub> slag. Reproduced from [7]. . . . .	40
3.9	Changes in droplet geometry as a reaction time proceeds for a iron drop containing 0.1wt.%P reacting with a slag initially containing 40 wt.% CaO, 30 wt.% SiO <sub>2</sub> , 30 wt.% Fe <sub>2</sub> O <sub>3</sub> . Reproduced from [9]. . . .	40
5.1	Comparison between Suito's [10, 11] and Basu's [12, 13] data at 1600°C	43
5.2	Revised Suito's correlation including Basu's data. . . . .	45
5.3	XRD of FeO synthesized from Fe <sub>2</sub> O <sub>3</sub> + Fe reaction. . . . .	49
5.4	XRD of FeO synthesized from Iron Oxalate. . . . .	50
5.5	Diagram of experimental setup. . . . .	51
5.6	Liquid slag predicted by FactSage using initial values from the first attempt to design a liquid slag with binary basicity of 3.0. . . . .	53
5.7	Liquid slag predicted by FactSage with binary basicity of 3.0 using iterative approach of adding more FeO as a slag flux. . . . .	54
5.8	Cross sectional area of a typical sample mounted in epoxy and polished.	60
5.9	Phosphorus mass balance uncertainty between initial target composition and final composition. . . . .	68
5.10	Initial and equilibrium phosphorus partition coefficient. . . . .	69
5.11	Comparison between present work, Tayeb's [2], Suito's [10, 11] and Basu's [12, 13] data. . . . .	70

5.12 Comparison between present work, Tayeb's [2], Suito's [10, 11] and Basu's [12, 13] data within the slag composition range defined in Table 5.9. . . . .	72
5.13 Schematic representation of two-dimensional structure of molten silicate slag (a) and depolymerization of the network by dissolution of metal oxides (b). Reproduced from [14] . . . . .	74
5.14 NBO/T <i>vs.</i> Lp. $\text{Fe}_t\text{O}$ contents in the slag range from 19 to 36 wt.%. Solid data from Tayeb et al. [2]. . . . .	75
5.15 Binary Basicity <i>vs.</i> Lp. $\text{Fe}_t\text{O}$ contents in the slag range from 19 to 36 wt.%. Solid black symbols from Tayeb et al. [2]. . . . .	76
5.16 $\text{Fe}_t\text{O}$ <i>vs.</i> Lp. CaO contents in the slag range from 40 to 52 wt.%. Solid data from Tayeb et al. [2]. . . . .	77
5.17 Example of time averaged temperature used for calculation of changes in $L_P$ due to furnace cooling. . . . .	84
5.18 MgO solubility as a function of binary basicity. . . . .	85
5.19 MgO solubility as a function of binary basicity and FeO content. . . . .	85
5.20 MgO saturation as as magnesiowustite as a function of binary basicity and FeO content at 1600°C. Reproduced from [1]. . . . .	86
5.21 Liquid fraction of slag predicted by FactSage for Suito's data. . . . .	88
5.22 Liquid fraction of slag predicted by FactSage for Basu's data. . . . .	89
5.23 Comparison between present work, Tayeb's [2] and Suito's [10, 11] using the new correlation from Equation 5.18. . . . .	91
5.24 Measured $L_P$ <i>vs.</i> Predicted $L_P$ for present work, Tayeb's [2] and Suito's [10, 11] data using the new correlation from Equation 5.18. . . . .	93



6.1	Schematics diagram of AOD [15](a), Q-BOP or OBM [16](b) and top-blown BOF [17](c) . . . . .	95
6.2	Histogram of the fraction of total monoxide present in the bulk slag in the form of MgO solid solution. . . . .	98
6.3	Histogram of the fraction of total monoxides present in the bulk slag in the form of CaO solid solution. . . . .	98
6.4	Histogram of the fraction of dicalcium silicate present in the bulk slag. . . . .	99
6.5	Contour and scatter plots for Actual $L_p$ vs. Equilibrium $L_P$ for AOD (6.5a and 6.5b) and Q-BOP (6.5c and 6.5d) for bulk slag compositions. Thickness of the contour lines are proportional to relative density of data. . . . .	102
6.6	Contour and scatter plots for Actual $L_p$ vs. Equilibrium $L_P$ for BOF 1 (6.6a and 6.6b) and BOF 2 (6.6c and 6.6d) for bulk slag compositions. Thickness of the contour lines are proportional to relative density of data. . . . .	103
6.7	Contour and scatter plots for Actual $L_p$ vs. Equilibrium $L_P$ for all furnaces studied using bulk slag compositions. . . . .	104
6.8	Contour plots for Actual $L_p$ vs. Equilibrium $L_P$ for AOD (6.8a and 6.8b) and Q-BOP (6.8c and 6.8d) for liquid slag compositions after FactSage correction. Thickness of the contour lines are proportional to relative density of data. . . . .	105
6.9	Contour plots for Actual $L_p$ vs. Equilibrium $L_P$ for BOF 1 (6.9a and 6.9b) and BOF 2 (6.9c and 6.9d) for liquid slag compositions after FactSage correction. Thickness of the contour lines are proportional to relative density of data. . . . .	106

6.10	Contour and scatter plots for Actual $L_P$ vs. Equilibrium $L_P$ for all furnaces studied after FactSage correction. . . . .	107
6.11	Superimposed Histograms of liquid slag fraction for each of the furnaces.	109
6.12	Scatter plot (6.12a) and contour plot (6.12b) of Actual $L_P$ vs. Equilibrium $L_P$ for the Q-BOP data containing monoxide phases predicted by FactSage for two MgO saturation levels: original FactSage prediction and twice the FactSage prediction; and bulk slag (6.12b). . . . .	112
6.13	$L'_P$ as a function of binary basicity. Data from [18]. . . . .	114
6.14	Impact of $L'_P$ on $L_P$ for BOF1 (6.14a) and Q-BOP (6.14b). . . . .	115
6.15	Scatter and contour plots for Actual $L_P$ vs. Equilibrium $L_P$ for Q-BOP corrected by FactSage (6.15a and 6.15c) and Q-BOP corrected by FactSage <i>and</i> with C <sub>2</sub> S partition taken into account (6.15b and 6.15d)	117
6.16	Scatter and contour plots for Actual $L_P$ vs. Equilibrium $L_P$ for BOF 1 corrected by FactSage (6.16a and 6.16c) and BOF 1 corrected by FactSage <i>and</i> with C <sub>2</sub> S partition taken into account (6.16b and 6.16d)	118
7.1	Diagram of CSLM experimental setup. (by Prof. Jingxi Wu) . . . . .	128
7.2	Heating profile used for each sample in the CSLM. . . . .	131
7.3	Schematic representation of image formation in the XCT process. . .	132
7.4	- Ball bar used as reference work piece in CT scans for voxel scaling to reduce measurement error. . . . .	134
7.5	Evolution of metal droplet geometry immersed in slag as a function of time for De-P experiments. . . . .	136
7.6	Measured oxygen concentration as a function of depth for the 20s sample.	141
7.7	Evolution of metal droplet geometry immersed in slag as a function of time for oxidation experiments. . . . .	142

7.8	Measured surface area of metal droplet for De-P experiments as a function of time. . . . .	144
7.9	Initial droplet weight vs maximum observed change in area. . . . .	146
7.10	Expected phosphorus concentration profile as a function of reaction time. Dotted line is only schematic. . . . .	149
7.11	Examples P-rich particles found in 0s sample. Secondary electron images taken at 20kV and 8000x. . . . .	150
7.12	Example of image processing to estimate area fraction of particles present in the metal matrix. . . . .	151
7.13	Analyzed phosphorus concentration profile as a function of reaction time.	152
7.14	Expected oxygen concentration profile as a function of reaction time.	157
7.15	Oxygen concentration and iron count rate as a function of depth . . .	159
7.16	Area, phosphorus and oxygen content as a function of reaction time. .	160
7.17	Measured surface area of metal droplet as a function of time for oxidation experiments. . . . .	161
7.18	Normalized surface area of metal droplet as a function of time for both sets of experiments. . . . .	162
7.19	Secondary electron images of Fe-P alloy heated in the absence of slag to evaluate the "Self-Dephosphorization" theory. . . . .	164
7.20	Measured droplet volume as a function of time. . . . .	168
7.21	Selected Isosurfaces for (a) 30 seconds sample and (b) 90 seconds sample.	169
7.22	Measured droplet volume as a function of time for oxidation experiments.	170

# Chapter 1

## Introduction

### 1.1 The Oxygen Steelmaking Process

In integrated steel plants, the steelmaking process starts with cokemaking and sintering followed by the Blast Furnace (BF). The BF is responsible for reducing the iron bearing charge such as iron ore, pellets or sinter and producing hot metal. The iron bearing raw materials, coke and fluxes are charged from the top of the reactor. A blast of hot air, enriched with oxygen and often combined with pulverized coal or natural gas is injected at the bottom of the furnace. The pulverized coal and coke react with oxygen to form carbon monoxide gas, which promotes the reduction of the iron oxides to metallic iron and provides energy. Due to the carbon rich environment in the blast furnace, the metallic iron becomes saturated with carbon and contains Si, Mn and P as impurities. The content of these impurities depends on the type of ores and fuel used. A typical composition of hot metal is shown in Table 1.1. The gangue from the ores, the ashes from coke and coal, and the charged fluxes, form a mixture of molten oxides called slag. A typical composition of blast furnace slag is shown in Table 1.2

Table 1.1: Typical Hot Metal Composition.

Element	Fe	C	Si	Mn	S	P
(wt.%)	94.5	4.5	0.40	0.30	0.03	0.07

Table 1.2: Typical BF Slag Composition.

Species	CaO	SiO <sub>2</sub>	MgO	Al <sub>2</sub> O <sub>3</sub>	Sulfur
(wt.%)	40	36	10	10	1

The residence time inside a Blast Furnace is of around 6 to 8 hours and, in the case of phosphorus, more than 96% of the total P input ends up in the hot metal.

After the BF, the hot metal is separated from the slag by simple density difference and normally is desulfurized in a separate process and later it proceeds to the Oxygen Steelmaking Process (OSM). In some plants, dephosphorization can also happen before the OSM, but this is generally not usual in Europe, North and South America. One of the most used reactors for oxygen steelmaking in the Basic Oxygen Furnace (BOF). The origin of the name BOF comes from the refractory lining and the additives made during furnace operation. In the BOF, hot metal and scrap are rapidly refined by the use of oxygen. The main goals of the BOF and other OSM operations are to lower the carbon, sulfur and phosphorus content in the metal bath, melt scrap and raise the temperature of the steel to around 1620-1640°C. [1]

During the beginning of the oxygen blow, fluxes are added to promote phosphorus, sulfur and refractory erosion control. These fluxes are rich in CaO and MgO and the two most used are burnt lime and dolomitic lime. CaO is mainly added to aid sulfur and phosphorus control and MgO is responsible for saturating the slag in order to minimize refractory erosion. [1] The dissolution of these fluxes, the oxidation of iron, manganese, sulfur and phosphorus results in highly basic slag. After the blowing

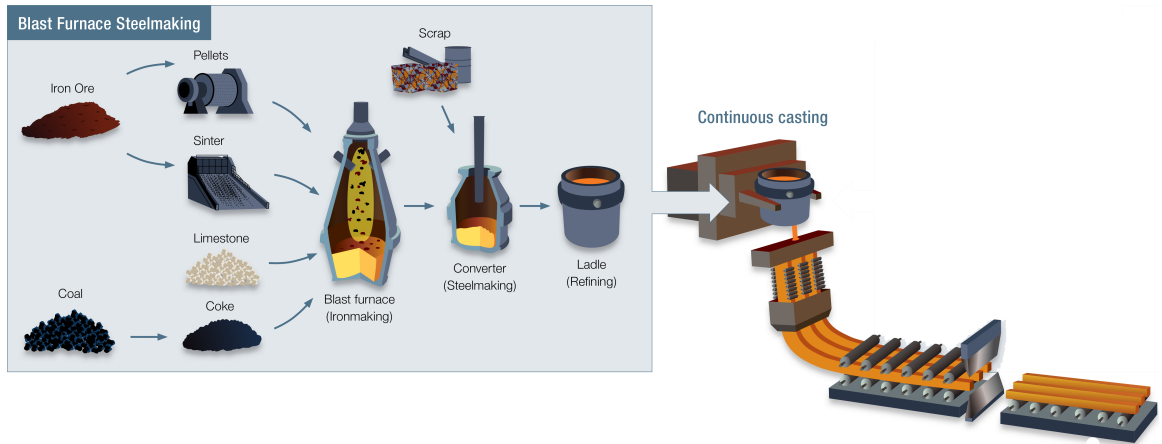


Figure 1.1: Overview of the steelmaking process. [3]

period, the slag floats on top of the metal bath and the steel is poured into a ladle and the slag is subsequently removed from the furnace.

After the BOF, the resulting product is called steel and it usually undergoes a secondary refining step. The goals of secondary refining are to fine-tune steel composition, temperature and inclusion content. This is achieved by flux injection, alloying, argon stirring, magnetic stirring and vacuum degassing processes. [1]

The steel is then poured into a tundish that feeds a continuous caster where the steel is cast. This concludes the steelmaking process and the subsequent operations include rolling, heat-treating, coating, etc. Figure 1.1 (reproduced from [3]) shows a schematic drawing of the combined BF, BOF, Ladle Furnace and Casting.

### 1.1.1 Historic Review of Modern Steelmaking Processes

Modern steelmaking processes began development during the second half of the 19<sup>th</sup> century with the Bessemer process and would evolve to a series of pneumatic steelmaking processes. The Bessemer process consisted of blowing air in a bottom-blown vessel lined with acid (siliceous) refractories through a bath of molten pig iron. Suf-

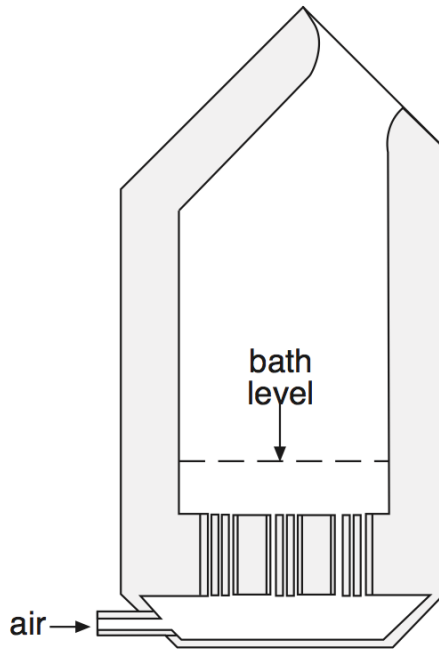


Figure 1.2: Diagram of Bessemer vessel. Reproduced from [1].

ficient heat was generated by the oxidation of impurities, such as silicon, manganese and carbon, that no external heat source was needed. This process worked particularly well with pig iron that was low in phosphorus, high in manganese and with adequate silicon. From 1870 to 1910, the majority of the steel in the world was produced by the Bessemer process. [19]

In Europe, the Basic Bessemer process or the Thomas process was patented in 1879. The process involved a basic lined vessel and a basic flux which made possible the refining of pig irons with high phosphorus content commonly found in various parts of Europe. The process was never used in the United States and saw a decline in production. By 1904, the open-hearth steelmaking process surpassed the production of the Thomas process, which continued to decline at a steady pace. [19]

The Siemens process, known as open hearth in the United States, was successfully demonstrated in 1868 and was initially known as the pig iron ore process. It was

constituted by a covered rectangular hearth which contained the pig iron and scrap charge. Combustion gas with excess oxygen would flow on top of the hearth and provide most of the energy required for refining the metal and oxygen to promote the oxidation of impurities in the bath. After passing the hearth, the gas was directed to one of two gas checkers where it would exchange heat with bricks and checkerwork. After 15 or 20 minutes the gas flow would switch directions and the checkers were used to preheat the gas and air to relatively high temperatures. This operation was repeated every fifteen to twenty minutes. Oxidation of impurities was promoted by both the oxygen of the air in the furnace and the iron ore added to the bath. These impurities were carbon, silicon and manganese. Obviously, a small amount of iron oxide was formed and would be part of the slag. The lining of the vessel was initially acid but later, due to the need of removing phosphorus, a basic lining of magnesite brick and dolomite would permit the addition of limestone and the formation of a basic slag. This was known as the basic process. The open hearth process became dominant in the United States. [1]

After World War II, the use of gaseous oxygen in the pneumatic process became commercially successful. This enabled steel to be produced at a fraction of the time required by the open hearth process. This resulted in the decline of the open hearth with the last facility US closed in 1991 in Utah. The first plants using top-blown oxygen reactors were in operation since 1952-53 at Linz and Donawitz in Austria. Bottom-blown basic vessels proved to be unsustainable due to the rapid deterioration of the refractory tuyere caused by the high temperatures attained during the process. On the other hand, blowing oxygen from the top was found to produce steel with high chemical and thermal efficiency. [19]

The most used top-blown process is commonly called basic oxygen process or BOP. Another common name refers to the reactor vessel as basic oxygen furnace or



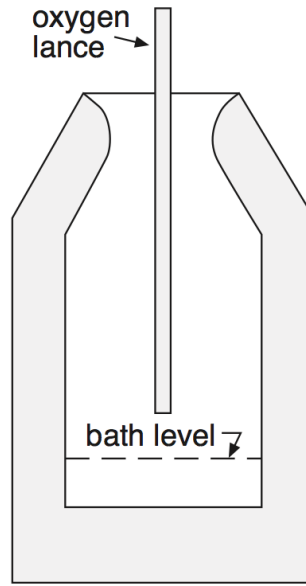


Figure 1.3: Diagram of a top-blown BOF. Reproduced from [1].

BOF. The process consists of a basic lined vessel where high purity oxygen is blown from a water cooled vertical top lance as shown in Figure 1.3.

During the 1970s, a bottom-blown process was successfully developed in Canada and Germany. The workaround to prevent the rapid deterioration of tuyere refractory was achieved by surrounding the oxygen gas by a sheath of another gas, usually propane or natural gas. This process is known as OBM in Europe and as Q-BOP in the United States. However, most of the steel made from hot metal uses the BOF or top-blown process which will be the major focus of this thesis.

Many other developments were made on oxygen steelmaking to better control the process. Vessels can often have bottom stirring coupled with the top injection of oxygen (combined blowing). The bottom gases are usually oxygen, argon or nitrogen and help stir the bath to provide better control over the reactions taking place during refining.

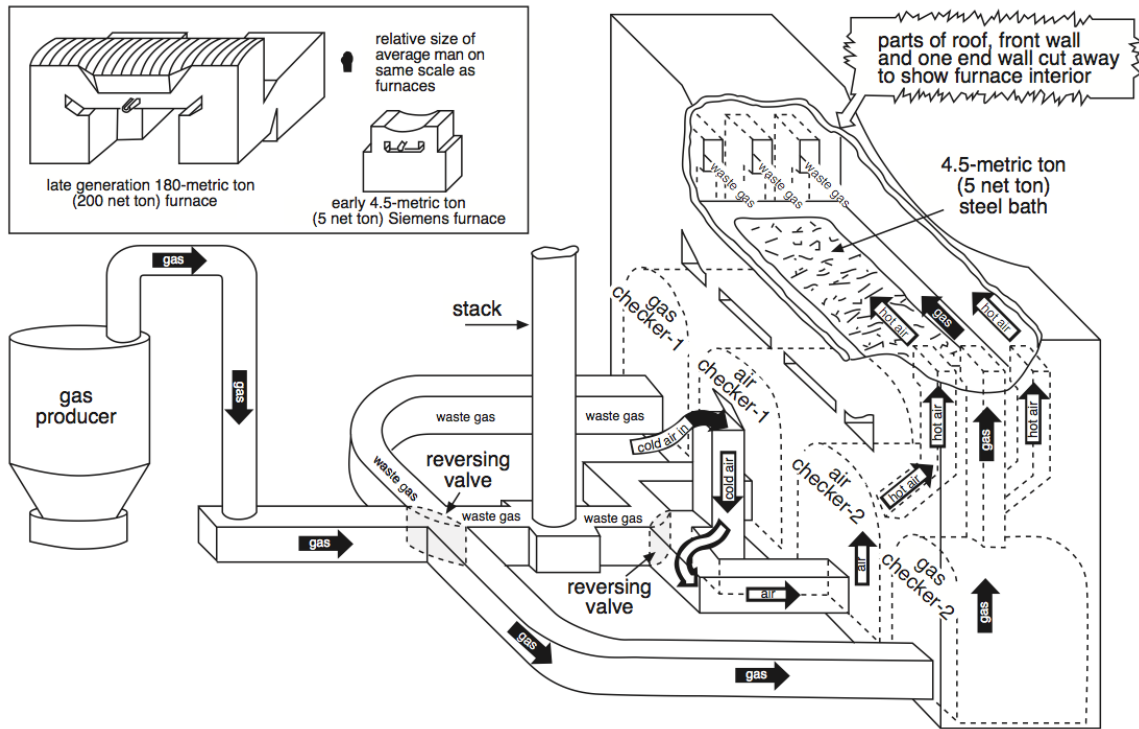


Figure 1.4: Diagram of Open Hearth Process. Reproduced from [1].

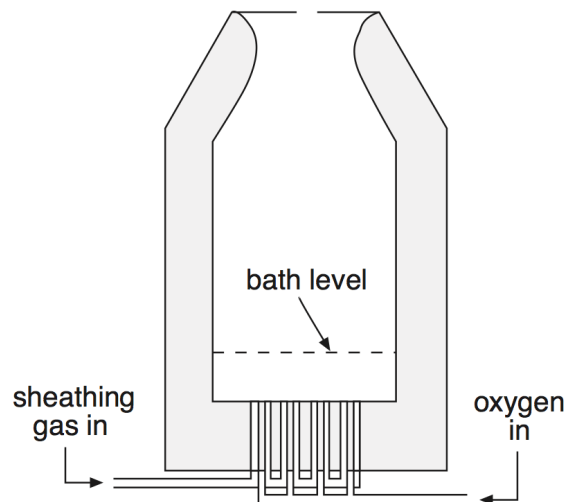


Figure 1.5: Diagram of a bottom-blown BOF. Reproduced from [1].

# Chapter 2

## Motivation

Low phosphorus content steels are essential for steel applications where high ductility is required, such as thin sheets, deep drawn, pipelines and automobile exteriors. Phosphorus' ability to strengthen and embrittle ferrite imposes restrictions on the maximum phosphorus content for the aforementioned applications. Many different strategies have been industrially implemented to help control the final phosphorus content in the steel but challenges in controlling phosphorus remain. [20]

The only source of phosphorus in steel is from the raw materials; thus, raw material selection is a way to maintain the phosphorus content within the desirable range. The iron ores available in the USA have phosphorus contents from 0.030wt.% to 0.060wt.%P. In South America, Brazilian ores have 0.035wt.% to 0.055wt.%P with low P ores usually present in the south and higher P ores in the north of Brazil; Venezuela and Peru both have contents around 0.090wt.%P. Australian ores have 0.025wt.% to 0.1wt.%P. Ores from Russia, Kasakistan and China have phosphorus content varying from 0.040wt.% to 0.150wt.%P. [20,21] In the past, phosphorus was not considered a big challenge in steel production because low P ores were readily available and considered cheap, since then, the price of iron ore has spiked. In the past

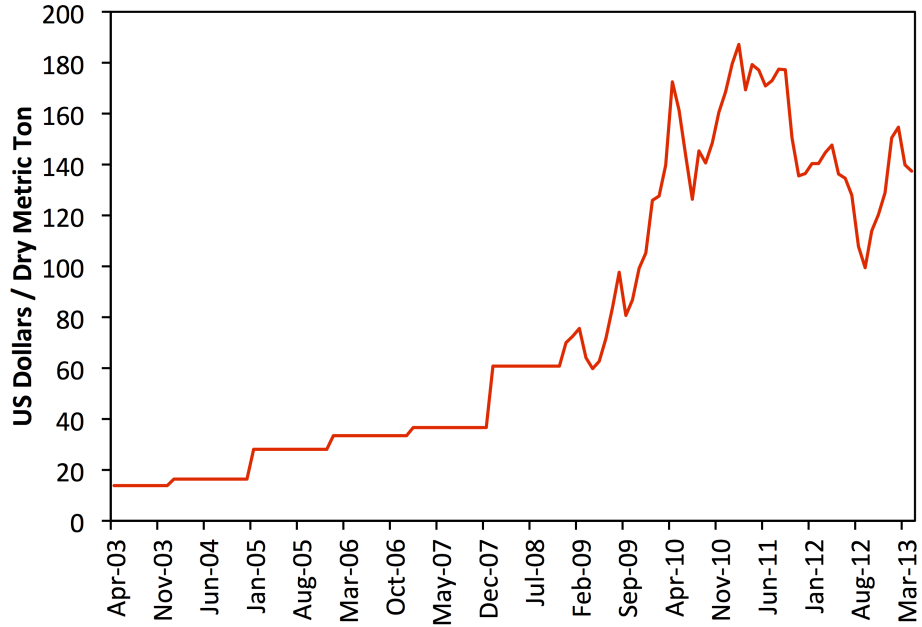


Figure 2.1: Price history of dry metric ton of iron ore. [4]

decade, iron ore price has risen by roughly 400% as shown in Figure 2.1. [4] Given this scenario, it is natural that companies start to look for less expensive iron ore sources. These sources often have higher phosphorus content. Therefore the removal of phosphorus in steelmaking demands greater efforts especially in plants where the quality of the raw materials used inevitably results in high phosphorus content in the hot metal. [21, 22]

A pretreatment of the hot metal after the blast furnace and prior to decarburization in the Oxygen Steelmaking Process (OSM) can be employed. The goal of the pretreatment is to remove sulfur and, sometimes, phosphorus and silicon. [20, 23] Hot metal dephosphorization is a common practice in Japan. In the United States and Europe hot metal pretreatment (HMPT) is limited to desulfurization. Dephosphorization is not attractive because it requires desiliconization, causing temperature loss, which reduces scrap melting in the OSM, and additional costs. [24]

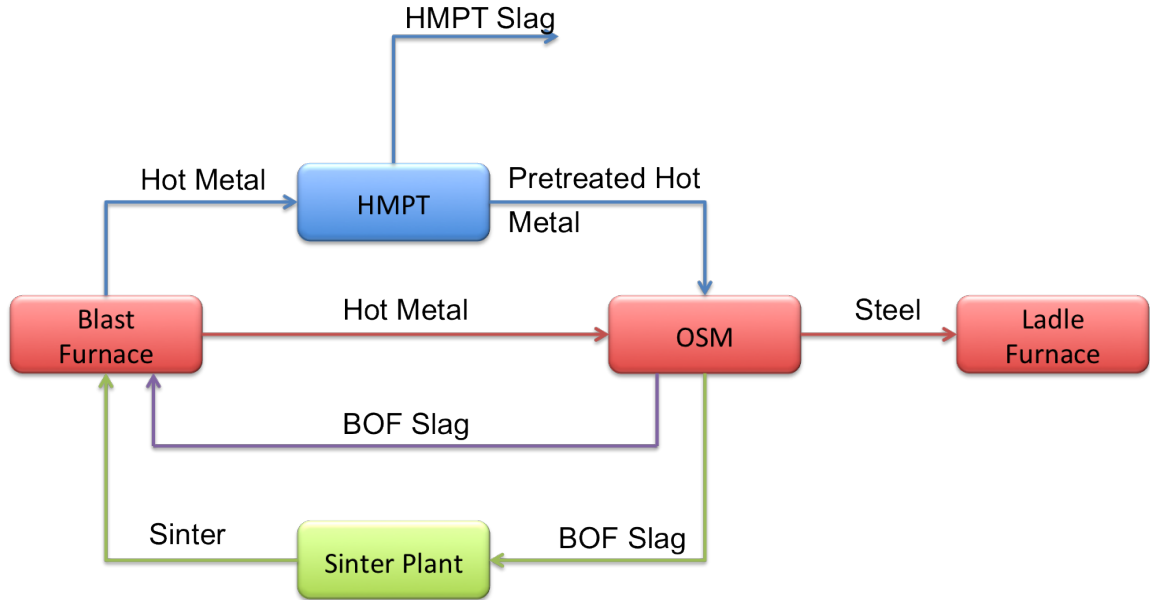


Figure 2.2: Different BF-OSM routes. In blue hot metal pretreatment is used. In purple the OSM slag is recycled directly to the blast furnace. In green the OSM slag is recycled to a sinter plant and then the sinter is charged on to the blast furnace.

Phosphorus can also be removed during the steel refining process. In fact, over 90% of the initial phosphorus in the melt can be removed in the BOF. The refining capacity of the slag depends of many variables such as slag and metal compositions, temperature, time and intensity of slag/metal stirring. [20]

In addition to P in the ores, phosphorous can enter the melt through recycled slag. A common practice is to recycle some of the OSM slag to a sinter plant or directly into the blast furnace. The sinter or the OSM slag is then fed to the blast furnace, inevitably increasing the phosphorus input on the process. The goal is to retrieve the iron and lime in the slag and to minimize slag disposal. [20, 23] Figure 2.2 compiles these different steelmaking routes where these techniques are employed.

Therefore, considering the industry needs for cheaper iron sources and the desire to recycle slag, it is necessary to improve our understanding on the thermodynamics

and kinetics of the phosphorus partitioning reaction between slag and metal melts during steelmaking. The available laboratory data does not correlate well with plant data and kinetics data is very limited. The goal of this project is to address these three topics using fundamentals to successfully predict equilibrium, model the kinetic behavior of phosphorus removal and suggest optimal slag compositions during OSM operation to maximize phosphorus removal.

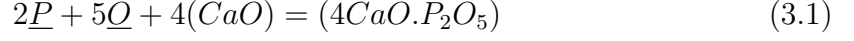
# Chapter 3

## Technical Background

### 3.1 The Phosphorus Reaction and Thermodynamic Equilibrium

Balajiva et al. [25] and Winkler et al. [26] conducted the first comprehensive studies on dephosphorization during the 1940s. Balajiva used an Electric Arc Furnace-like design where an indirect arc heated the metal and, as soon as the slag was added, a direct arc was applied to the slag. Balajiva's apparatus however was not able to maintain a constant temperature for more than 40 minutes, which is very low compared with the equilibration time reported by other authors. [10, 13, 27] Regardless of whether or not equilibrium was achieved, Balajiva et al. did observe that FeO and CaO are necessary slag constituents when dephosphorizing steel. They also observed that the dephosphorization reaction is exothermic and that the slag dephosphorization capacity decreases with temperature. Winkler and Chipman [26] used an induction furnace with two graphite electrodes placed above the bath to provide radiant heat to keep the slag molten. The experiments were carried out for 30 minutes. Chipman then

attempted to calculate an equilibrium constant for the desphosphorization reaction described by equation 3.1.

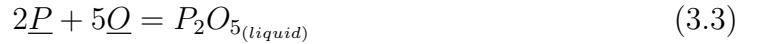


Where the underline designates species in solution in the steel for the 1 wt% standard state and curved brackets are species present in the slag. The equilibrium constant for (3.1) was given by:

$$K_P = \frac{a_{4CaO.P_2O_5}}{[a_P]^2[a_O]^5(a_{CaO})^4} \quad (3.2)$$

Winkler and Chipman [26] also observed that dephosphorization is enhanced by a decrease in temperature and increase in FeO content and basicity of the slag.

In 1953, Turkdogan and Pearson [28] pointed out that the unsatisfactory nature of the early studies were due to arbitrary methods employed to calculate the actual concentration of the reactants (free lime, ferrous oxide, etc.). These methods were merely empirical correlations and could be applied only to very narrow ranges of composition to describe equilibrium. In fact, they did not relate to the actual activities in the system and did not hold when conditions were changed. Turkdogan and Pearson proposed that it is satisfactory to consider the reaction taking place in its simplest form.



They also evaluated the change in free energy using an estimate of the entropy of fusion of  $P_2O_5$ , so that



$$\Delta G_T^\circ = -168000 + 133.0T \text{ (cal/mol)} \quad (3.4)$$

$$\log K_P = \frac{36850}{T} - 29.07 \quad (3.5)$$

$$K_P = \frac{a_{P_2O_5}}{[\%P]^2[\%O]^5} \quad (3.6)$$

Turkdogan and Pearson also computed the activity coefficient of phosphorus pentoxide. The activity coefficient was increased by silica and decreased by basic oxides such as CaO and MgO. [28]

During the 1980s Suito and coworkers [10, 11, 29, 30] did an extensive investigation on phosphorus partitioning in various slag systems. In 1981 Suito [10] studied the CaO-SiO<sub>2</sub>-MgO-FeO<sub>x</sub> system using MgO crucibles in the temperature range of 1550-1650°C. Although the experiments were carried out in magnesia crucibles, the MgO content in the slag did vary significantly pointing that the MgO dissolution from the crucible to the slag is much slower than the equilibration time used. They concluded that the phosphorus distribution ratio increased with increasing content of CaO in the slag and with decreasing temperature.

In 1982, Suito and Inoue [29] published a paper on the effect of calcium fluoride on phosphorus partition. The experiments were also carried out from 1550°C to 1600°C. Suito concluded that the effect of CaF<sub>2</sub> on dephosphorization is the same as CaO without raising the melting point of the slag. In 1984 they [30] published a study on the effects of barium and sodium oxides on phosphorus partitioning. They concluded that the CaO equivalencies of Na<sub>2</sub>O and BaO are 1.2 and 0.9 on weight percent basis respectively. Also in 1984 they [11] published an article about phosphorus distribution

in MgO-saturated slags of the system CaO-Fe<sub>t</sub>O-SiO<sub>2</sub>-P<sub>2</sub>O<sub>5</sub>-MnO. The same article proposed the last form of Suito's correlation:

$$\log \frac{(\%P)}{[\%P](T.Fe)^{\frac{5}{2}}} = 0.0720 \left[ (\%CaO) + 0.3(\%MgO) + 0.6(\%P_2O_5) + 0.6(\%MnO) \right] + \frac{11570}{T} - 10.520 \quad (3.7)$$

In 1985, Zhang et al. [31] proposed a different phosphorus partition correlation that included an additional temperature term and the effect of SiO<sub>2</sub>. The derivation used the formalism of Flood, Forland and Grjotheim (F.F.G.) [32] together with experimental data.

The F.F.G. treatment is based on the idea that molten slags are fully ionized. For a given anionic exchange reaction, the equilibrium constant can be defined as:

$$\log K_{mix} = \sum_i N_{Me_i^{2+}} \log K_{Me_i^{2+}} + f(\gamma) \quad (3.8)$$

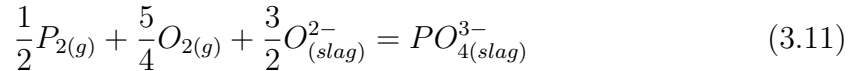
where  $K_{mix}$  is the equilibrium constant for the complex anionic reaction,  $N_{Me_i^{2+}}$  is the molar fraction of each cation present in the slag (Ca, Mn, Mg, Fe),  $K_{Me_i^{2+}}$  is the equilibrium constant for the formation of pure phosphates in the form of  $Me_3(PO_4)_2$  and  $f(\gamma)$  corresponds to a logarithmic function of all activity coefficients. [33] The final result from [31] is given by Equation 3.9.

$$\begin{aligned}
\log \frac{(\%P_2O_5)}{[\%P]} = & \\
2.5 \log (\%FeO) + \frac{1}{T} \left[ 162(\%CaO) + 127.5(\%MgO) + 28.5(\%MnO) \right] & \\
- 6.28 \times 10^{-4}(\%SiO_2)^2 + \frac{11000}{T} - 10.40 & \quad (3.9)
\end{aligned}$$

In 2000, Ide and Fruehan [27] revised Suito's correlation; specifically the MgO coefficient was found to be 0.15 instead of 0.30. These experiments were carried in CaO crucibles so that the MgO content could be varied. The revised Suito's correlation is given by:

$$\begin{aligned}
\log \frac{(\%P)}{[\%P](T.Fe)^{\frac{5}{2}}} = & \\
0.0720 \left[ (\%CaO) + 0.15(\%MgO) + 0.6(\%P_2O_5) + 0.6(\%MnO) \right] + \frac{11570}{T} - 10.520 & \quad (3.10)
\end{aligned}$$

In 2005, Lee and Fruehan [34] looked at phosphorus equilibrium between hot metal and low FeO containing slags relevant for new smelting processes, such as HIs melt. It was pointed out that phosphorus in the slag exists as a phosphate ion and that its formation can be expressed as a gas-slag reaction by



The results showed that the Log of the phosphorus partition increased with  $2.5 \log \%FeO$  as predicted by the thermodynamics and that increasing slag basicity also increases the partition coefficient as verified by other authors. [10–13, 25–27,

29, 30, 34–36]

In 2007 Basu and coworkers published two articles [12, 13] where they studied the phosphorus partition between liquid steel and  $\text{CaO-SiO}_2\text{-FeO}_x\text{-P}_2\text{O}_5\text{-MgO}$  slags at 1600°C and 1650°C. A horizontal tube furnace with  $\text{MoSi}_2$  heating elements was used to carry out the experiments. In the first article, the slag contained a FeO content of up to 15 wt.% [13], it was concluded that increasing the slag basicity  $((\text{wt.\%CaO})/(\text{wt.\%SiO}_2))$  up to 2.0 has a strong increasing effect on the phosphorus partition. However, the increase is much less pronounced with basicities above 2.5. It was also noticed that phosphorus partition ratio initially increased with increasing FeO content but then decreases after a certain level is reached. It has been proposed that this level is a function of slag basicity and temperature. The second article studied slag within the same previous system but with FeO contents between 15 and 25 wt.%. [12] It was found that most of the conclusions presented in the previous article hold. More specifically, the phosphorus partition was shown to be independent of FeO contents above 19 wt.%. Additionally, the phosphorus partition appeared to be lowered with an increase of MgO content at both temperatures.

In 2000, Turkdogan [35] revisited his assessment of  $\text{P}_2\text{O}_5$  activity coefficients in molten slags. It was found that for slags containing from 0.2 to 1.0wt.% of  $\text{P}_2\text{O}_5$  the activity coefficient,  $\gamma_{\text{P}_2\text{O}_5}$ , was given by Equation (3.12).

$$\log(\gamma_{\text{P}_2\text{O}_5}) = -9.84 - 0.142\left((\%CaO) + 0.3(\%MgO)\right) \quad (3.12)$$

It is important to notice that  $\log(\gamma_{\text{P}_2\text{O}_5})$  is a linear function of CaO and MgO content and that there is no temperature dependence on the above equation. For slag containing  $\text{P}_2\text{O}_5 > 10\text{wt.\%}$  it was found that  $\log(\gamma_{\text{P}_2\text{O}_5})$  was also a linear function of CaO but it had a temperature dependence as shown in Equation (3.13).

$$\log(\gamma_{P_2O_5}) = -\frac{34950}{T} + 3.85 - 0.058(\%CaO) \quad (3.13)$$

Basu et al. [22] also reviewed the activity coefficient of  $P_2O_5$  in slags using data from various authors and his own work. They found that expressing  $\log(\gamma_{P_2O_5})$  as a function of ionic fractions of the slag oxides yielded a better agreement with the data. In his correlation, the temperature dependence was very small, which agrees with the findings of Turkdogan for slags with low  $P_2O_5$  content. Basu's correlation is shown in Equation (3.14).

$$\begin{aligned} \log(\gamma_{P_2O_5}) = & -8.172X_{Ca^{2+}} - 7.169X_{Fe^{2+}} \\ & - 1.323X_{Mg^{2+}} + 1.858X_{SiO_4^{4-}} + \frac{340}{T} + 11.66 \end{aligned} \quad (3.14)$$

Where  $X_i$  corresponds to the ionic fraction of species  $i$ .

From the coefficients of Equation (3.14), it can be seen that increases in the concentrations of  $Ca^{2+}$ ,  $Fe^{2+}$  and  $Mg^{2+}$  result in a decrease of the activity coefficient of  $P_2O_5$  whereas  $SiO_4^{4-}$  has the opposite effect.

Other approaches to model phosphorus partition between steel and slag have been tried. In 2011, Yang et al. [37] proposed an exhaustive thermodynamic model based on the ion and molecule coexistence theory (IMCT) to predict phosphorus distribution ratio between  $CaO-SiO_2-FeO-Fe_2O_3-MnO-Al_2O_3-P_2O_5$  slags and molten steel. The IMCT assumes that the slag is composed of simple ions, such as  $Ca^{2+}$ ,  $Fe^{2+}$ ,  $Mg^{2+}$  and  $O^{2-}$ ; simple molecules,  $P_2O_5$ ,  $SiO_2$  and  $Al_2O_3$ ; silicates, aluminates and many others as complex molecules. Every ionic species takes part in reactions to form complex molecules from  $(Me^{2+}$  and  $O^{2-})$  ion couples and simple molecules and are under thermodynamic equilibrium. The possible phosphorus molecules taken into account were

$P_2O_5$ ,  $3FeO \cdot P_2O_5$ ,  $4FeO \cdot P_2O_5$ ,  $2CaO \cdot P_2O_5$ ,  $3CaO \cdot P_2O_5$ ,  $4CaO \cdot P_2O_5$ ,  $2MgO \cdot P_2O_5$ ,  $3MgO \cdot P_2O_5$  and  $3MnO \cdot P_2O_5$ . It was found that  $3CaO \cdot P_2O_5$  and  $4CaO \cdot P_2O_5$  had a contribution to the measured phosphorus partition of 96% and 4% respectively. All these studies have one major aspect in common: CaO and FeO play the major role in promoting dephosphorization.

In conclusion, phosphorus equilibrium has been extensively studied and many correlations have been developed. When slag species are considered, Equation 3.11 seems reasonable. The phosphorus partition ratio should be proportional to  $a_{O^{2-}}$  (CaO) and oxygen potential as  $FeO_t$  to the power of 2.5.

Correlations assuming the formation of  $P_2O_5$ , or  $P_2O_7^{4-}$  ionically, would require the P partition ratio to be  $\frac{(\%P_2O_5)}{[\%P]^2}$  and it has been found that polymerization of phosphorus does not occur extensively in the slags commonly found in steelmaking.

The discussion so far involved the phosphorus equilibrium between liquid iron and liquid slag. However, due to the multicomponent nature of slags, it is not uncommon to have possible solid phases in equilibrium with the molten slag. An extensive amount of work has been done on specific solid phases that are common in steelmaking slags. More specifically, studies have focused on slags containing  $2CaO \cdot SiO_2$  and CaO particles. [18, 38–42] These solid phases are commonly present in steelmaking slags during OSM operation and can play a role for dephosphorization since phosphates can be dissolved in them. This is further discussed in section 3.2.

## 3.2 Phosphorus Refining in BOF Operation

Previously in Chapter 1, OSM operation was explained superficially. This section focusses in providing a more detailed overview of the reactor.

### 3.2.1 Overview of Typical Top-Blown BOF Operation

The sequence of operations in the oxygen steelmaking process is heavily based on plant design and can vary widely in basic layout. Smooth flow of materials plays a key role in plant design and, therefore, the logistics of materials handling is very important for BOF operation. This however falls outside the scope of the present document and only a general overview of the main process operations are detailed in this section.

The hot metal from the blast furnace is poured in a torpedo shaped, refractory lined car commonly called torpedoes. Through railways each car arrives at the shop and the hot metal is transferred to a ladle. At this stage some shops perform hot metal treatment focussed on removing sulfur by usually adding lime and magnesium. To charge the BOF the vessel is rotated and tilted so that a crane can charge scrap metal before the hot metal is poured. Charging scrap before the hot metal avoids splashing and is considered a safer practice. Hot metal from the ladle is then poured into the furnace and this can take up to 5 minutes depending on the shop. The furnace is then set in the upright position so that the oxygen blowing can begin. Blowing usually takes between 15 to 25 minutes and oxygen is added in several batches that differ in lance height and oxygen flow rate. An example of the oxygen batches and its purpose is shown in Table 3.1. [1]

Flux additions are made soon after the oxygen blowing begins. These fluxes are important to control the phosphorus and sulfur capacities of the slag. Fluxes are rich in CaO and MgO usually from burnt lime and dolomitic lime respectively. CaO plays a big role in phosphorus and sulfur removal and MgO is added to saturate the slag with MgO and minimize corrosion on the refractory lining which is mostly made of MgO. Fluorspar ( $\text{CaF}_2$ ) is sometimes used when low FeO slags are present.

Table 3.1: Example of Oxygen Batches in a BOF. [1]

Batch N°	Lance Height, in	Oxygen Vol., Nm <sup>3</sup>	Purpose
1	150	850	Initiate oxidizing, heat generating reactions without touching solid scrap charge
2	120	1700	Increase reaction rates and control slag formation
3	90	11650	Promote optimum carbon removal rate and proper slag for the other reactions

FeO helps to dissolve CaO and low FeO levels make it hard to add lime and still ensure proper slag viscosity. Adding fluorspar is sometimes used to help dissolve lime without increasing the FeO content of the slag. Coolants such as iron ore and pellets can be added with the fluxes to modulate temperature and provide initial iron oxide to dissolve lime.

After the blow is finished, the vessel is rotated, samples are taken and sent for chemical analysis. If corrections are needed, reblow or addition of coolants may be required. When the heat is ready, the furnace rotates to the tapping side and the steel is poured through a taphole into a ladle. The slag floats on top of the steel and it is very important to minimize slag carryover. During tapping several alloy additions are made to achieve the proper chemistry once secondary refining begins. At this point the oxygen steelmaking process is complete and the ladle continues to a ladle arc furnace or degasser.

### 3.2.2 Slag Formation Duration Oxygen Blow

*‘A good steelmaker is a good slagmaker’* is a popular phrase in the steel community and very relevant in the context of oxygen steelmaking. Having a good control over



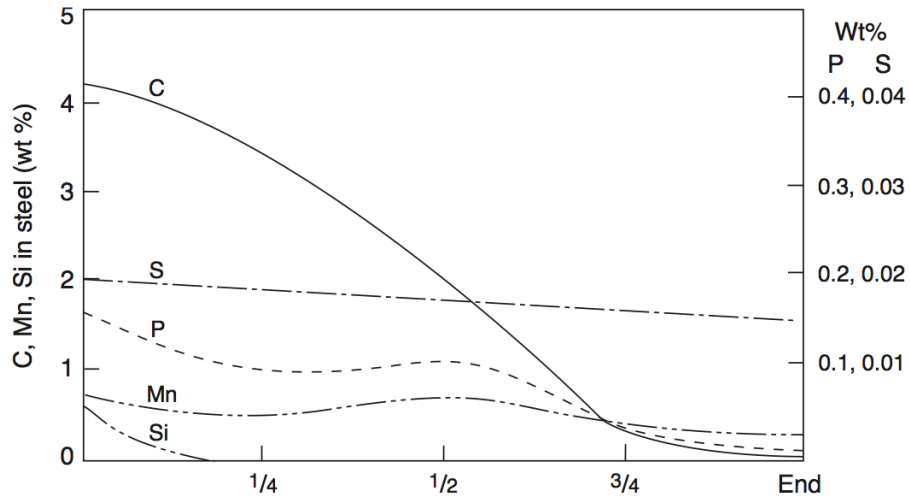


Figure 3.1: Change in metal composition during blowing. Reproduced from [1].

slag formation and composition enables optimum refining and minimizes the risk of having to reblow oxygen or make extra additions at the end of the heat. Several authors have studied the formation of slag during oxygen blow. [43–45]

During the beginning of the blow, the lance is kept high above the surface of the metal. During the first 3-4 minutes silicon from the metal rapidly oxidizes together with iron forming a slag rich in  $\text{FeO}$  and  $\text{SiO}_2$ . Significant amounts of lime and dolomitic lime are added into the furnace. As the blow continues, solid lime continuously dissolves into the liquid slag increasing the slag mass and basicity. As decarburization continues, the slag starts to foam and the  $\text{CO}$  gas generated reduces the  $\text{FeO}$  content in the slag. Close to the end of the blow, the decarburization rate decreases and iron oxidation becomes significant again. Throughout the blow the metal temperature steadily increases from  $1350^\circ\text{C}$  to  $1650^\circ\text{C}$  and the slag temperature is usually  $50^\circ\text{C}$  higher than the metal at the end of the blow. [1,44] Figures 3.1 and 3.2 illustrate the aforementioned changes.

The mechanism of lime dissolution is very relevant to BOF operation and phos-

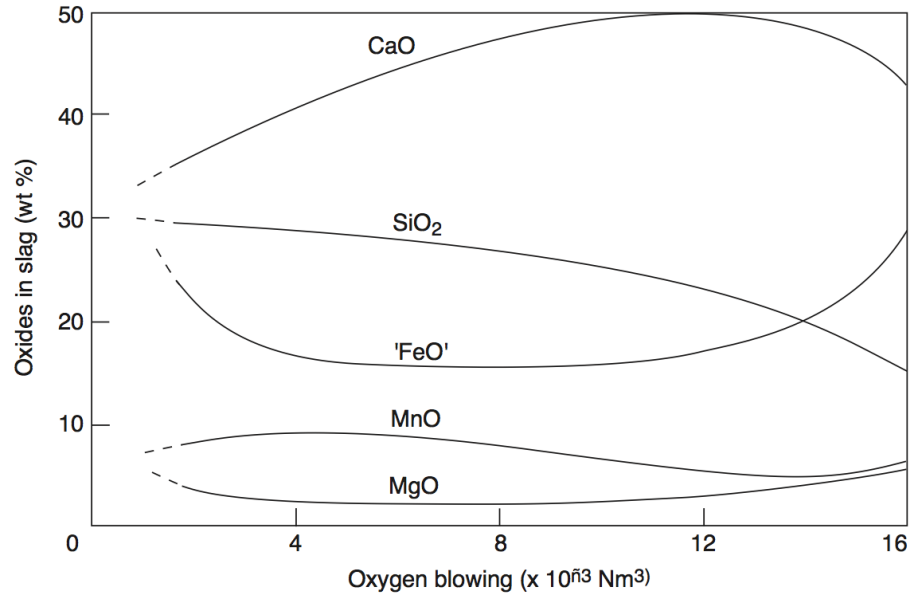


Figure 3.2: Change in slag composition during blowing. Reproduced from [1].

phorus removal. Achieving fast dissolution of lime during the BOP provides great opportunity to increase productivity, reduce process time and cost.

The dissolution mechanism of lime is a function of slag composition and the saturation level of dicalcium silicate. In oxygen steelmaking, the initial slag is rich in FeO and SiO<sub>2</sub>. When lime is first added and starts dissolving, a layer of dicalcium silicate, 2CaO·SiO<sub>2</sub>, forms around the solid particles and slows down the lime dissolution rate. [46] This solid layer can rupture and slag can further penetrate into the pores of the lime particle and continue dissolution. The slag penetration is a function of viscosity and pore size of the solid particle. [44]

Because in oxygen steelmaking there are often some solid oxide phases coexisting with the slag, it is important to understand how solid particles can influence phosphorus removal. Several studies have looked at the phosphorus solubility in different solid particles such as CaO, 2CaO·SiO<sub>2</sub> and 3CaO·SiO<sub>2</sub>. [18, 38–42]

In 2006, Suito and Inoue published a series of three articles related to phosphorus

partition between liquid slag and lime and dicalcium silicate particles. [18, 38, 40] In the first article, they investigated the phosphorus equilibrium between the  $\text{CaO-SiO}_2\text{-Fe}_t\text{O}$  and  $2\text{CaO}\cdot\text{SiO}_2$  system. It was found that the phosphorus partition between the  $2\text{CaO}\cdot\text{SiO}_2$  particles and the slag varied between 2 to 70 as the  $\text{Fe}_t\text{O}$  content and basicity in the slag increased. The temperature dependence of P distribution was found to be very weak and the  $2\text{CaO}\cdot\text{SiO}_2$  isolated particles showed complete uniform transformation to  $2\text{CaO}\cdot\text{SiO}_2\text{-3CaO}\cdot\text{P}_2\text{O}_5$  within 5 seconds.

Suito and Inoue looked at the phosphorus transfer from  $\text{CaO-Fe}_t\text{O-SiO}_2\text{-P}_2\text{O}_5$  slag to  $\text{CaO}$  particles. [40] They investigated the reaction mechanism immediately after  $\text{CaO}$  particles contact  $\text{P}_2\text{O}_5$  containing slags. It was found that upon contact with the  $\text{CaO-Fe}_t\text{O-SiO}_2\text{-P}_2\text{O}_5$  slag, the  $\text{CaO}$  particle was rapidly encapsulated by a layer of  $2\text{CaO}\cdot\text{SiO}_2\text{-3CaO}\cdot\text{P}_2\text{O}_5$  and a  $\text{CaO-Fe}_t\text{O}$  slag without  $\text{P}_2\text{O}_5$  being formed between the  $\text{CaO}$  particle and the  $2\text{CaO}\cdot\text{SiO}_2\text{-3CaO}\cdot\text{P}_2\text{O}_5$  solid solution.

In 2008, Kitamura et al. [42] proposed two possible routes for phosphorus transfer from slag to dicalcium silicate. First,  $2\text{CaO}\cdot\text{SiO}_2\text{-3CaO}\cdot\text{P}_2\text{O}_5$  would precipitate from the liquid slag after phosphorus is transferred from the metal phase. In the second proposed route, dicalcium silicate particles would already be present in the slag before phosphorus is transferred from the metal. Phosphorus would then diffuse into the precipitated, phosphorus-free, dicalcium silicate particle. It was found that the phosphorus transfer rate by the precipitation route was much faster than by the diffusion route. This points to the fact that having pre-existing dicalcium silicate particles does not necessarily improve phosphorus removal.

### 3.2.3 The Dephosphorization Mechanism in Oxygen Steel-making

During the blow in oxygen steelmaking a very dynamic environment is created. As the oxygen jet hits the surface of the slag and, subsequently, the molten metal, it creates a three phase gas-slag-metal emulsion, which drastically increases the total interfacial area available for several chemical reactions to occur between the phases. Metal droplets are continuously ejected from the bulk metal bath into the slag-gas mixture where they can react for a given amount of time. The generation of these metal droplets is very important for the kinetics inside the furnace and several studies have been published on the topic. [47–52]

The rate of refining, during oxygen steelmaking, is not only a function of the chemical kinetics but also a function of the residence time that a given metal droplet spends in the slag. [48] Brooks et al. [48] calculated the residence time of a metal droplet being ejected from the bulk metal traveling in a ballistic trajectory across the slag. The calculated residence time was less than 1 second which is too short for a given droplet to react to a significant extent. However, when Min et al. [51] studied the behavior of Fe-C droplets in slag, it was observed the formation of a gas“halo” while decarburization was occurring, which kept the metal droplet suspended in the slag for up to 200 seconds. Molloseau et al. [53] also observed the same behavior of Fe-C-S droplets which were kept suspended in the slag for up to 50 seconds. Based on these observations, Brooks et al. [48] modified the model to include the effect of decarburization on the apparent density of a metal droplet and was able to predict residence times consistent to the reported by various authors.

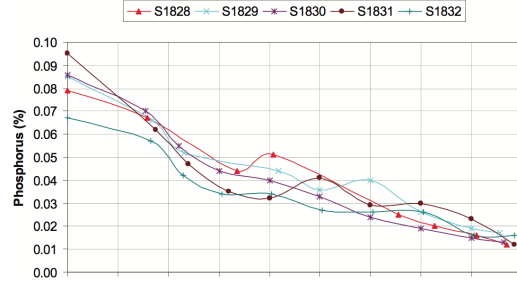
In 2011, Millman and coworkers [5] through the European Commission and the Research Fund for Coal and Steel, published a report entitled “*Imphos: Improving*

*Phosphorus Refining*". This report looked at samples simultaneously taken from a pilot 6 ton converter located at MEFOS in Lulea, Sweden. The report details the sampling tool design and goes through analysis of samples to determine the mechanism of phosphorus removal in the BOF. The sampling system was designed by Corus UK and consisted of individual stacked pots that were immersed in the pilot scale BOF and opened simultaneously to allow the collection of samples at the same time but at different heights inside the vessel. The report looked, among other topics, at metal/slag ratio profiles, size distribution of metal droplets in the slag/metal emulsion, phosphorus distribution at slag-metal interface and lime dissolution.

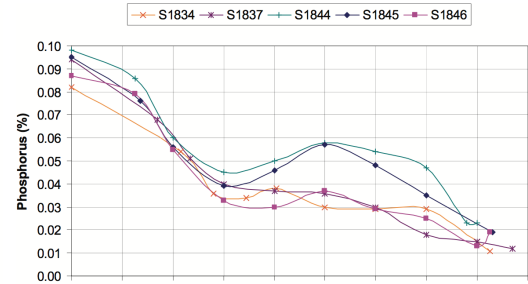
They defined five phosphorus removal profiles shown in Figure 3.3. For each of these profiles, the amount of metal and its chemical composition was studied for the slag/metal emulsion and for the bulk bath. It was found that the phosphorus content of the metal drops in slag was usually lower than or equal to the bulk bath, pointing to the fact that phosphorus removal was driven by dephosphorization of metal droplets present in the slag/metal emulsion rather than in the bulk bath.

One interesting observation was that, during the early stages of the blow, phosphorus removal in the emulsified droplets happened a lot faster than decarburization. Metal droplets were found to be extremely depleted in P ( $\ll 100\text{ppm}$ ) while still presenting well over 1 wt% C. This could be potentially related with the gas "halo" and emulsification observations by Min et al. [51] and Molloseau et al. [53], which could increase the residence time of droplets during the early stages of the blow giving it enough time to react with the highly oxidizing slag present, resulting in fast P removal if the droplet size is appropriate.

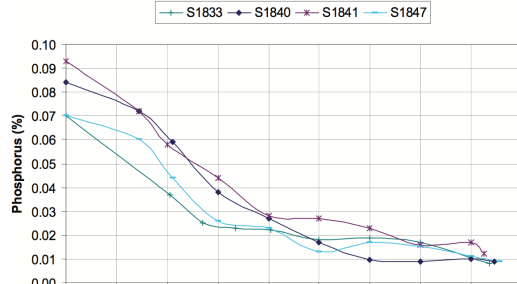
Since P removal is strongly related to the generation of metal droplets, there should be an ideal lance height during each stage of the blow to maximize droplet generation and create a good slag/metal/gas emulsion. Millman and coworkers [5]



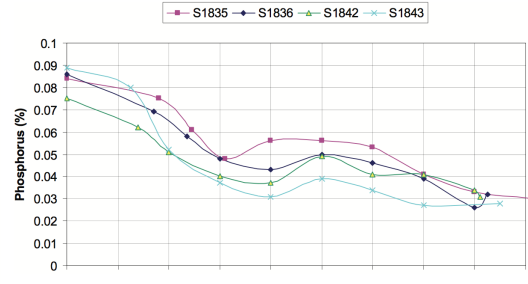
(a) Near-Constant Phosphorus Profile



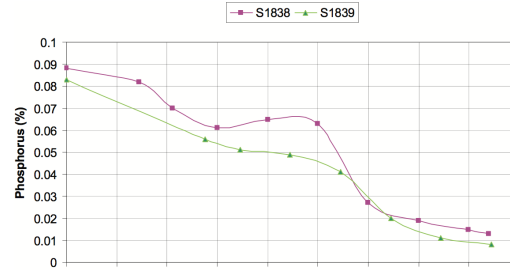
(b) Phosphorus Reversion Profile



(c) High Phosphorus Removal Profile

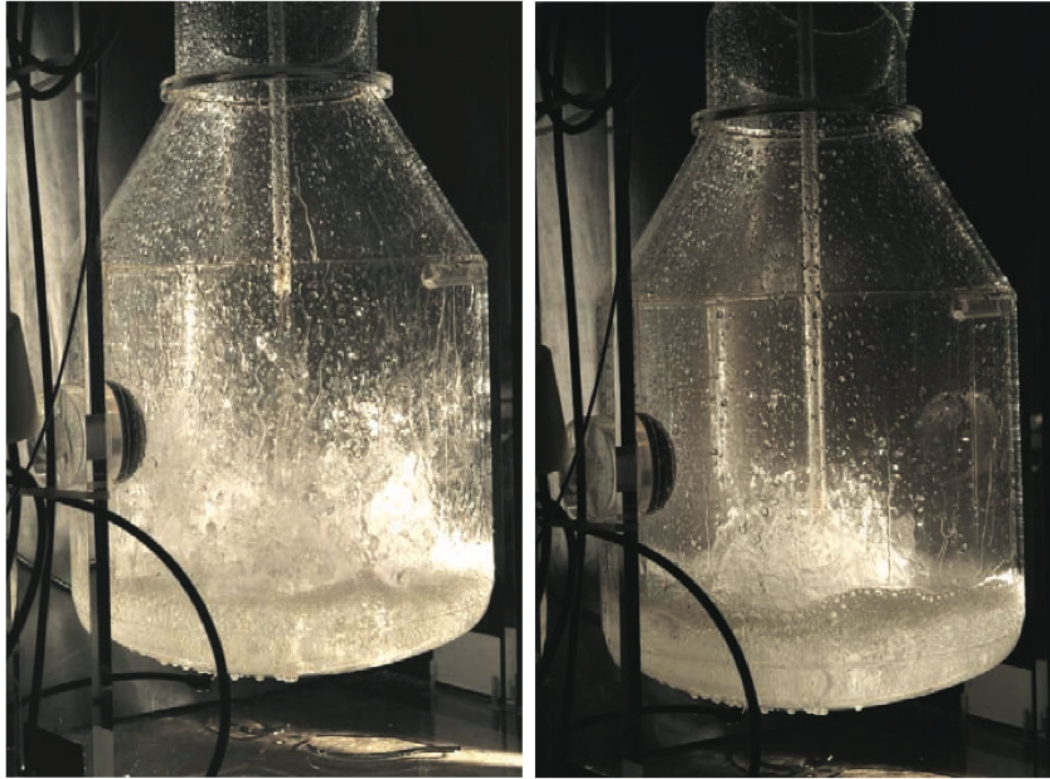


(d) Phosphorus Reversion and Slowdown Profile



(e) Reversion with Rapid Phosphorus Removal Profile

Figure 3.3: Different phosphorus removal profiles observed by [5]. Reproduced from [5].



(a) Droplet Generation: Maximum Lance Height (b) Droplet Generation: Lance Lowered by 30cm.

Figure 3.4: Changes in droplet generation at different lance heights. [5]. Reproduced from [5].

also investigated this using a 1:25 scale BOF model using water and air to simulate the metal bath and oxygen injection respectively. It was observed that as lance height decreases, fewer metal droplets are generated as shown in Figure 3.4.

The dephosphorization mechanism in oxygen steelmaking can be summarized as:

1. During the beginning of the blow, where the oxygen lance is kept high, good ejection of droplets is achieved and phosphorus removal happens fast.
2. As the blow continues and decarburization starts generating CO gas, FeO in the slag is reduced and the slag can become not oxidizing enough. Which can result in reversion of phosphorus into the melt as droplets are rephosphorized

and return to the bulk metal. This is specially important if dissolution of lime is not optimum.

3. Closer to the end of the blow, decarburization slows down and the FeO content in the slag increases favoring dephosphorization once again. This however, may not be enough to compensate for the possible reversion that occurred earlier.
4. Optimum results can be achieved by closely monitoring FeO and CaO in the slag. Iron ore additions can be helpful to maintain ideal FeO content to continue phosphorus oxidation in parallel with decarburization.

Overall, oxygen steelmaking is immensely complex with many factors playing an important role in primary steel refining. Slag formation, droplet formation, mass transfer, heat transfer and parallel chemical reactions are examples of key operational factors in the BOF. We are incapable of addressing all of these topics. As will be discussed later, this research is focussed on the reaction of a metal drop with liquid slag.

### **3.3 Kinetics of Phosphorus Removal**

While phosphorus equilibrium has been extensively studied as discussed in Section 3.1, the kinetic behavior of phosphorus removal has not been studied to the same extent. However, the same principles for other high temperature metallurgical reactions apply.

When P dissolved in iron contacts slag, there are several steps that take place during the dephosphorization reaction. These steps provide a basic illustration of the phenomenon and include:

1. Mass transfer in the metal phase of [P] and [O] towards the slag-metal interface;



2. Mass transfer in the slag phase of ( $\text{O}^{2-}$ ) towards the slag-metal interface;
3. Chemical reaction at the slag-metal interface for the formation of ( $\text{PO}_4^{3-}$ );
4. Mass transfer in the slag phase of ( $\text{PO}_4^{3-}$ ) away from the reaction interface.

Given the high temperatures that dephosphorization occurs, it is reasonable to assume that the chemical reaction at the interface is fast and at equilibrium. Therefore, the possible rate limiting steps are mass transfer in the metal or slag phases or both, if we assume there are not solid phases present in the slag capable of absorbing phosphorus.

In 1998, Monaghan et al. [54] published a study on the kinetics of dephosphorization of  $\text{Fe-C}_{(sat)}\text{-P}$  hot metal by oxidizing slags. They noted that one of the main challenges in studying dephosphorization of hot metal is to correctly quantify the driving force for the reaction due to the non-equilibrium oxygen potential at the slag/metal interface. This non-equilibrium occurs due to the decarburization of hot metal which lowers the oxygen potential in the metal. In such cases, the slag is at a high oxygen potential while the metal is at a low oxygen potential.

Monaghan et al. [54] used an induction furnace where five kilograms of carbon-saturated iron were melted in a graphite crucible. Phosphorus was added to the metal phase as ferrophosphorus prior to melting and 500 grams of slag was usually used. The change in chemical composition of both slag and metal was monitored by sampling both phases at given time intervals. The temperature difference between both phases was kept under  $\pm 10^\circ\text{C}$ . It was found that dephosphorization reaction followed a first order kinetic rate with respect to phosphorus concentration in the metal. They also looked at the effect of iron oxide content in the slag and found that higher  $\text{FeO}$  contents increase the mass transfer coefficient of the slag due to a decrease in viscosity, even though  $\text{FeO}$  can also impact either positively or negatively

the driving force of the reaction. They concluded that mass transport in the slag phase was the rate limiting step. If that is the case, the phosphorus content in the slag can be described by:

$$\frac{d(\%P)}{dt} = \frac{k_s \rho_s A}{W_s} ((\%P)_i - (\%P)_b) \quad (3.15)$$

Where  $W_s$  is the weight of the slag,  $A$  is the interfacial area,  $\rho_s$  is the density of the slag,  $k_s$  is the mass transfers coefficient in the slag and  $(\%P)_i$  and  $(\%P)_b$  are the phosphorus contents at the interface and the bulk of the slag. Equation 3.15 is related to the change in phosphorus content in the metal by a mass balance:

$$Q \frac{d[\%P]}{dt} = -\frac{k_s \rho_s A}{W_s} ((\%P)_i - (\%P)_b) \quad (3.16)$$

where  $Q$  is the ratio of the weights of metal and slag. If the interface is at thermodynamic equilibrium, Equation 3.16 can be rewritten using the phosphorus partition coefficient,  $L_P$ , in terms of the phosphorus concentration in the metal:

$$Q \frac{d[\%P]}{dt} = -\frac{k_s \rho_s A}{W_s} \left( \frac{[\%P]_0}{[\%P]_e} \right) ([\%P]_b - [\%P]_e) \quad (3.17)$$

$$L_P = \frac{(\%P)_e}{[\%P]_e} \quad (3.18)$$

where  $[\%P]$  denotes phosphorus in the slag,  $W_s$  is the weight of the slag,  $A$  is the interfacial area,  $\rho_s$  is the density of the slag,  $k_s$  is the mass transfers coefficient in the slag,  $t$  is the time and the subscripts  $e$ ,  $b$  and  $0$  denote equilibrium, bulk and initial values respectively. Integration of Equation 3.17 leads to the final equation used by

Monaghan et al. [54]

$$\left(\frac{[\%P]_e}{[\%P]_0}\right)\left(\frac{W_s}{\rho_s A}\right)\ln\left[\frac{[\%P]_b - [\%P]_e}{[\%P]_0 - [\%P]_e}\right] = -k_s t \quad (3.19)$$

More recently, Fruehan and Manning [6] looked at the rate of the phosphorus reaction between liquid iron and slag. They assumed that the chemical reaction was fast and at equilibrium and noted that the oxygen potential at the interface was controlled by the slag phase due to its high FeO content. This is different from what Monaghan et al. [54] assumed, since there is no decarburization occurring to deplete the oxygen potential at the interface. Another important assumption was that the metal/slag interfacial area was constant throughout the reaction. However, as will be discussed later, this assumption appears not to be true.

If phosphorus is conserved in the system and there is no accumulation at the interface, the flux out of the metal phase and into the slag are equal to each other with opposing directions and can be expressed by

$$\frac{\partial(\%P)}{\partial t}W_s = -\frac{\partial[\%P]}{\partial t}W_m \quad (3.20)$$

where  $W_s$  and  $W_m$  are the weights of the slag and metal phases respectively. The flux equations for each of the phases are:

$$\frac{\partial(\%P)}{\partial t} = -\frac{A\rho_s k_s}{W_s}[(\%P) - (\%P)_i] \quad (3.21)$$

$$\frac{\partial[\%P]}{\partial t} = -\frac{A\rho_m k_m}{W_m}[[\%P] - [\%P]_i] \quad (3.22)$$

where the subscripts  $s$ ,  $m$  and  $i$  stand for slag, metal and interface respectively.

At the reaction interface, it is said that concentrations are the ones predicted by

thermodynamic equilibrium and are related by the equilibrium phosphorus distribution ratio

$$L_P = \frac{(\%P)_i}{[\%P]_i} \quad (3.23)$$

Combining equations 3.20 through 3.23 and solving for  $[\%P]_i$ :

$$[\%P]_i = \frac{\rho_m k_m [\%P] + \rho_s k_s (\%P)}{\rho_m k_m + \rho_s k_s L_P} \quad (3.24)$$

substituting equation 3.24 into equation 3.22 and simplifying gives the following result:

$$\frac{\partial [\%P]}{\partial t} = -\frac{A \rho_m k_m}{W_m} \frac{1}{\frac{\rho_m}{k_s \rho_s L_P} + \frac{1}{k_m}} \left[ [\%P] - \frac{(\%P)}{L_P} \right] \quad (3.25)$$

From equation 3.25, one can define an overall mass transfer coefficient given by  $k_0$  which has units of cm/s:

$$k_0 = \frac{1}{\frac{\rho_m}{k_s \rho_s L_P} + \frac{1}{k_m}} \quad (3.26)$$

From a mass balance, one can establish how the phosphorus contents in the slag and metal are related:

$$[(\%P) - (\%P)_0] = -[[\%P] - [\%P]_0] \frac{W_m}{W_s} \quad (3.27)$$

By combining and integrating equations 3.25 through 3.27, one can obtain an expression which computed  $[\%P]$  as a function of time.

$$-A_T k_0 t = \frac{W_m}{\rho_m} \frac{1}{1 + \frac{W_m}{L_P W_s}} \ln \left[ \left( 1 + \frac{W_m}{L_P W_s} \right) \frac{[\%P]}{[\%P]_0} - \frac{W_m}{L_P W_s} \right] \quad (3.28)$$

Where  $A_T$  corresponds to the total surface area including the area of any metal droplets present due to possible emulsification of the metal phase.

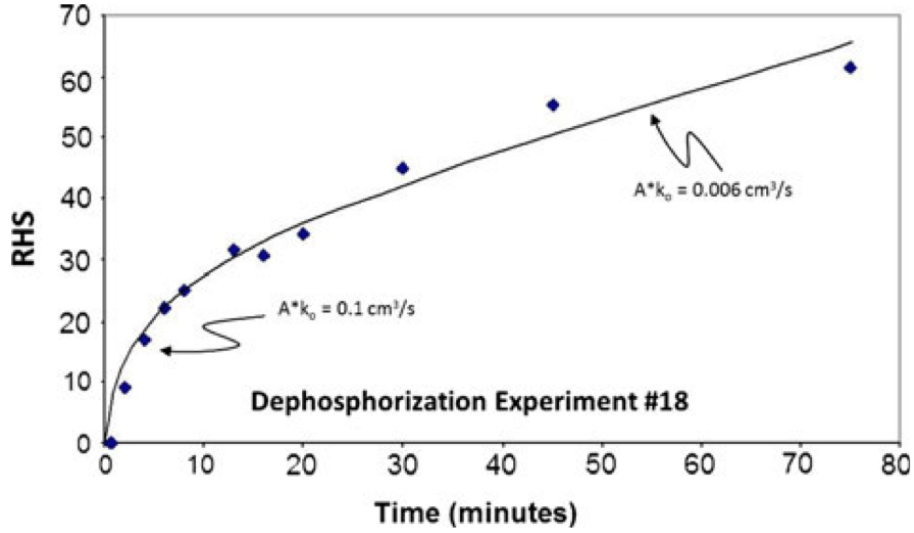


Figure 3.5: Dephosphorization data from experiment 18. Reproduced from [6].

Fruehan and Manning [6] used the aforementioned mathematical approach to quantify the mass transfer of phosphorus between metal and slag. They used a 10kW induction furnace to study the rate of transfer of phosphorus from metal to slag and slag to metal as a function of temperature and slag composition. The temperature range used was from 1550°C to 1650°C. Approximately 200g of iron was used and inductively heated and stirred. The slag mass used was approximately 70g and a molybdenum wire was wrapped around the magnesia crucible to act as a susceptor to heat the slag. Several metal and slag samples were taken at different times with sampling intervals ranging from 30 seconds to 10 minutes.

They used equation 3.28 to plot the right hand side (RHS) of the equation versus time which should yield a straight line with a slope equals to  $A_T k_0$  if their product is constant. They found that the  $A_T k_0$  parameter decreased as the reaction proceeds suggesting that either  $A_T$ ,  $k_0$  or both are decreasing. This behavior is exemplified in Figure 3.5.

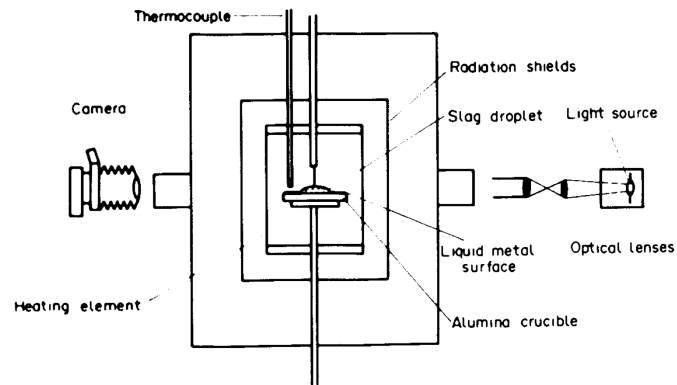
They concluded that the apparent mass transfer coefficient seems to be a function

of interfacial tension, which is affected by the mass flux of a surface active element, such as oxygen, especially under rapid mass transfer conditions. The overall mass transfer parameter ( $A_T k_0$ ) was estimated to be on the order of  $0.07 \text{ cm}^3/\text{s}$  at the beginning of the reaction and it decreases to  $0.007 \text{ cm}^3/\text{s}$  as the reaction approaches an end. The changes in the mass transfer parameter is related to dynamic interfacial phenomenon which enhances the mass transfer during periods of high flux of oxygen across the interface. This high flux of oxygen is suggested to lower the interfacial tension during the reaction which could lead to an increase in the interfacial area or mass transfer coefficient or both. [6]

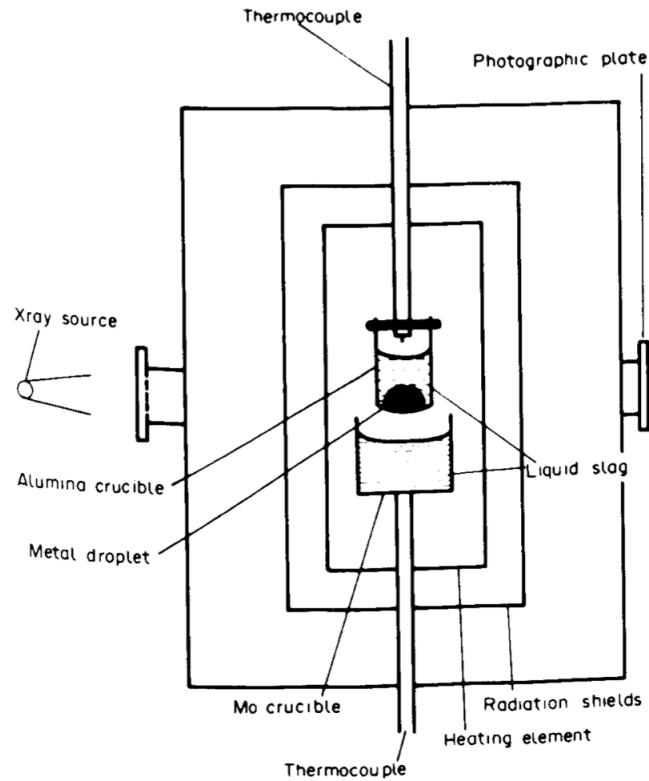
It has been shown by various authors that spontaneous emulsification can occur during periods of intense mass transfer of surface active elements due to a very pronounced reduction in the interfacial tension between two immiscible liquids. [7, 9, 55]

In 1984, Gaye et al. [7] studied both equilibrium and dynamic properties of metal-slag interfaces. He used two experimental methods to study the equilibrium interfacial tension between several iron based alloys and slags. The first method consisted of a slag drop resting on top of a liquid metal substrate. They used a furnace with side openings to enable direct observation and various furnace atmospheres were used depending on the system in question. The main advantage of this method was that the slag drop could stay in place for long periods of time, thus achieving slag/metal equilibrium. The second method consisted of a metal drop immersed in liquid slag. This setup used a X-ray source operating at 120kV and 100mA was used to generate images. Schematics for both of these setups are shown in Figure 3.6.

They concluded that, for the equilibrium interfacial tension, the oxygen and sulphur contents in the metal played a significant role on the observed equilibrium tension. Also, the effect of slag composition was shown to be small. Nonetheless, the addition of  $\text{CaF}_2$  and  $\text{Na}_2\text{O}$  raise the interfacial tension but  $\text{MnO}$  additions tend to



(a) Experimental setup used by Gaye et al. [7] for the observation of a slag drop resting on a liquid metal substrate



(b) Experimental setup used by Gaye et al. [7] for the observation of a metal drop immersed in slag.

Figure 3.6: Diagram of both experimental setups used by Gaye et al. [7]. Reproduced from [7].

lower it. Figure 3.7 summarizes the equilibrium interfacial tension results for the studied systems.

For the the study of dynamic interfacial phenomenon, the same setup from Figure 3.6b was used. They observed a drastic decrease of dynamic interfacial tension for all systems studied if the initial driving force for a given reaction was high enough. Gaye [7] looked at several iron alloys and slags, including an Fe-P alloy in contact with a CaO-Al<sub>2</sub>O<sub>3</sub>-Fe<sub>2</sub>O<sub>3</sub> slag. The mechanism of the phenomenon was divided in three different stages. First, the interfacial tension progressively decreases and the droplet shape flattens. The reaction is said not to be at its maximum rate and interfacial tension reaches an intermediate value. Second, interfacial forces “vanish” and reach an extremely low value when the reaction rate is believed to be at its maximum. Third, as the reaction slows down, interfacial tension recovers at a very fast rate and droplets assume roughly a spherical shape.

Gaye et al. [7] concluded that when the oxygen flux becomes larger than about 0.1 g atom m<sup>-2</sup> s<sup>-1</sup>, the interfacial tension approaches a value close to zero. When oxygen flux becomes lower than 0.01 g atom m<sup>-2</sup> s<sup>-1</sup>, interfacial tension rapidly increases to a value close to the equilibrium tension. This is summarized in Figure 3.8.

In 1998, Jakobsson et al. [9] studied the interfacial characteristics of dephosphorization. They used a setup similar to Gaye et al. [7] to generate X-ray images. An Fe-P alloy containing 0.1wt.% P was reacted with a 40 wt.% CaO, 30 wt.% SiO<sub>2</sub>, 30 wt.% Fe<sub>2</sub>O<sub>3</sub> slag. They observed that after 10 seconds of contact between the metal droplet and the slag, the drop flattened considerably pointing to a significant decrease in interfacial tension between the two phases. As the reaction progressed, the contact angles increased pointing that the interfacial tension was returning to its equilibrium value as mass transfer slowed down as seen in Figure 3.9.

In summary, dephosphorization kinetics has been far less studied than phosphorus



equilibrium between metal-slag. There are disagreements whether mass transfer in the metal, slag or both control the rate of the reaction.

Due to the nature of the reaction, dynamic interface phenomena appears to have a significant role on the overall rate of the reaction. Spontaneous emulsification seems to occur when rapid mass transfer of oxygen takes place at the interface of metal-slag systems. This results in a substantial decrease in interfacial tension, thus increasing the reaction area and its overall rate. However, direct calculation of changes in reaction area due to spontaneous emulsification remains very difficult.

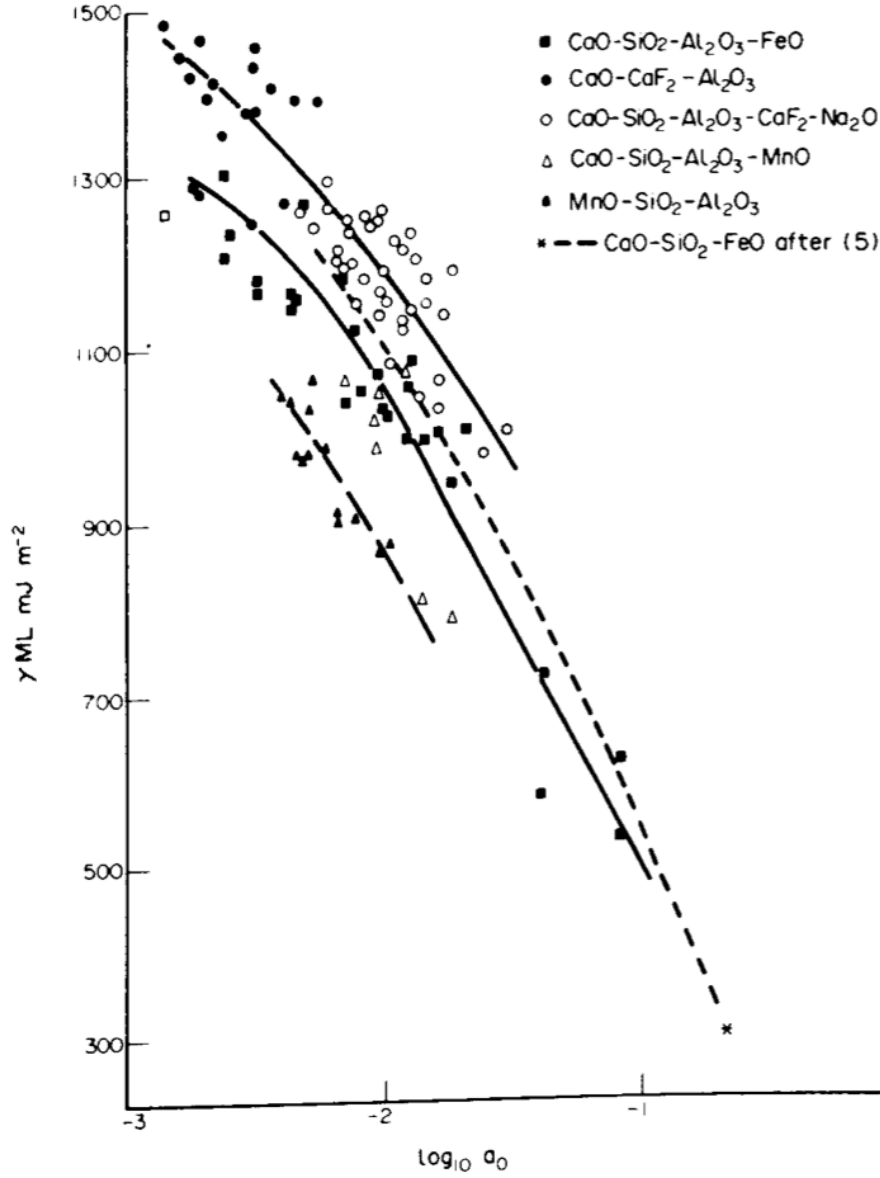


Figure 3.7: Effect of oxygen activity on the equilibrium interfacial tension of different Fe-based alloys and slags at 1600°C. Dashed line for  $\text{CaO-SiO}_2\text{-FeO}$  from [8]. Reproduced from [7].

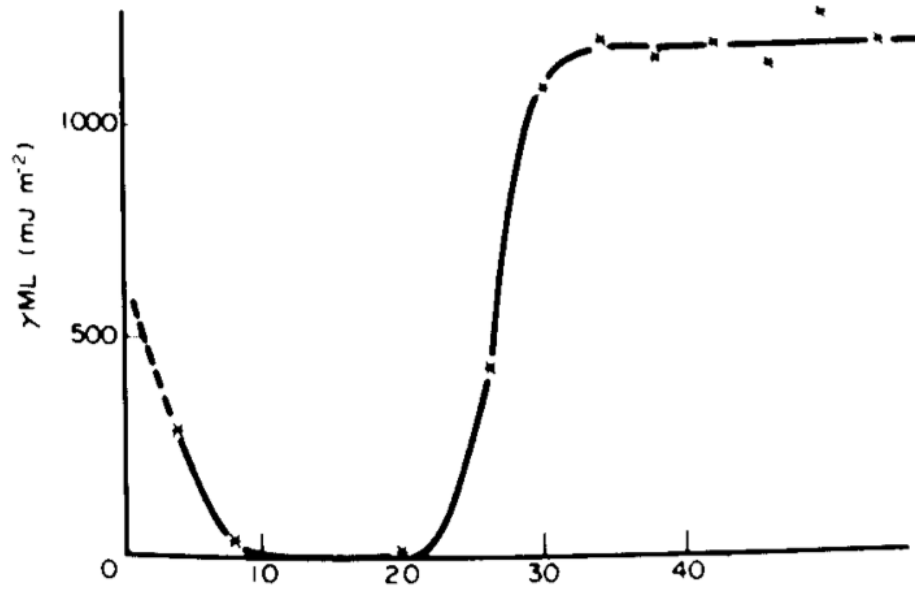


Figure 3.8: Interfacial tension as a function of time for Fe-Al alloy in CaO-Al<sub>2</sub>O<sub>3</sub>-SiO<sub>2</sub> slag. Reproduced from [7].

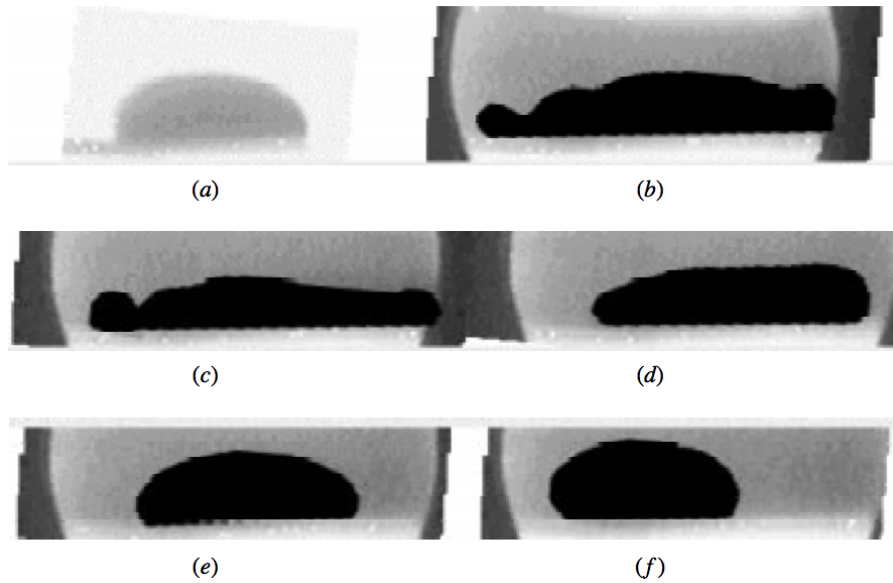


Figure 3.9: Changes in droplet geometry as a reaction time proceeds for a iron drop containing 0.1wt.%P reacting with a slag initially containing 40 wt.% CaO, 30 wt.% SiO<sub>2</sub>, 30 wt.% Fe<sub>2</sub>O<sub>3</sub>. Reproduced from [9].

# Chapter 4

## Objectives and Hypotheses

The overall objectives of this research project are to study the behavior of phosphorus partitioning between liquid iron and liquid slag as a function of slag chemistry; evaluate the degree of non-equilibrium in several industrial vessels by analyzing actual plant data; and study the kinetic behavior of metal droplets suspended in liquid slag as a function of reaction time. For each of these three topics, a corresponding hypothesis has been formulated as follows:

1. The disagreements in the available data for phosphorus equilibrium can be resolved by careful study including approaching equilibrium from both sides of the system and ensuring liquid slags.
2. Phosphorus equilibrium is not achieved in regular plant operation and it is limited by liquid phase mass transfer on both metal and slag phases.
3. The kinetics of dephosphorization is limited by liquid phase mass transfer in both metal and slag phases. Due to spontaneous emulsification, the reaction area greatly increases in the early stages of mass transfer. The previous studies were only able to *qualitatively* analyze this effect.

## Chapter 5

# Phosphorus Equilibrium Between Liquid Iron and CaO-MgO-SiO<sub>2</sub>-FeO-P<sub>2</sub>O<sub>5</sub> Slags

### 5.1 Introduction

As previously discussed in Section 3.1, phosphorus equilibrium between liquid metal and slag has been extensively studied since the 1940's. In order to evaluate the present state of phosphorus equilibrium partitioning prediction, this research utilized the tabulated data provided in two of Suito's papers [10, 11] as well as the more recent data from Basu's work [12, 13]. The form of a Suito's type correlation can be explained from thermodynamic fundamentals. It shows how the slag composition affects the activity coefficients of  $O^{2-}$ ,  $PO_4^{-3}$  and  $Fe^{2+}$  based on the first interaction type coefficients of a Taylor series. For simplicity purposes, only the data at 1600°C was compared. Figure 5.1 shows the plot of the data at 1600°C using Suito's revised correlation proposed by Ide and Fruehan. [27] Although the experimental data seems

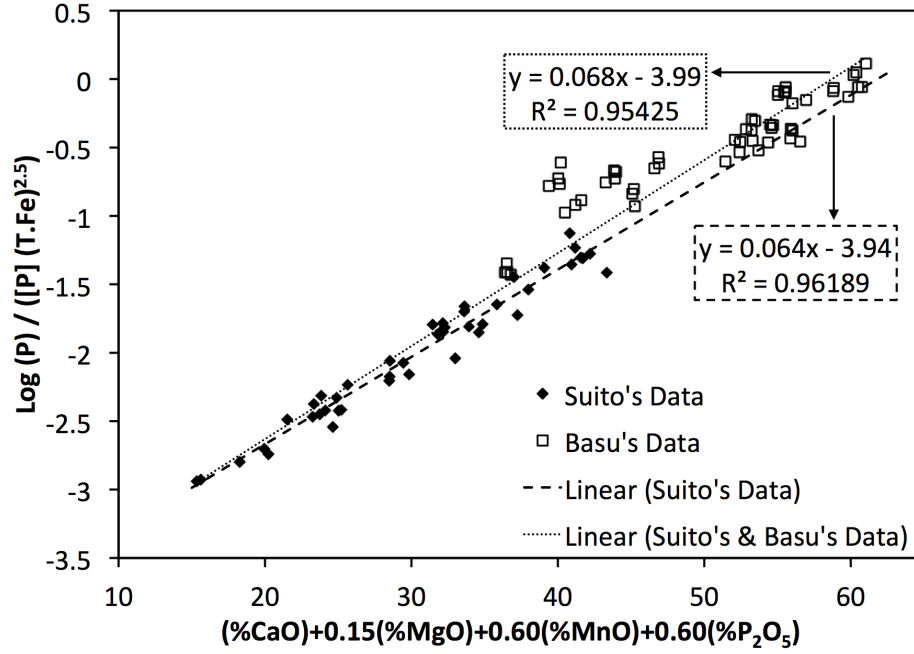


Figure 5.1: Comparison between Suito's [10, 11] and Basu's [12, 13] data at 1600°C

to fit well the line, it is important to remember that the plot is in logarithmic scale, this means that a vertical scatter of 0.3 corresponds to a factor of 2 for the real y-axis variable.

Two linear regression lines are shown in Figure 5.1. The dashed line corresponds to a linear regression using only Suito's data and extrapolated to cover Basu's range of data. The reported slope is 0.064, which is 11% lower than the original coefficient of 0.072. This difference is most likely due to the fact that not all data from Suito was included, but rather only the experimental data relevant to steelmaking. The dotted line corresponds to a linear regression utilizing both sets of data. The slope in this case is 0.068 which is in better agreement to the original coefficient of 0.072. The  $r^2$  coefficients cannot be directly compared since one  $r^2$ , *i.e.* 0.96, takes into account only Suito's data and the other, *i.e.* 0.95, considers both sets of data. Finally, the y-axis intercepts are slightly different. Such a difference corresponds to a factor of

approximately 1.12 if the log term is removed from the correlation.

Some disagreement is still present in Figure 5.1. In an attempt to resolve this issue, a multiple linear regression was made combining both sets of data. This was done using the software package Excel Mac 2011 and the statistical analysis plugin StatPlus. The software utilizes the tabulated data from a Excel spreadsheet and assigns a linear coefficient for each righthand side variable, *i.e.* CaO, MgO, etc., based on the least square method. The result can be seen in Figure 5.2. The new value of the  $r^2$  parameter is 0.97228 and the slope is the same as in Figure 5.1. However, the x-axis coefficients and y-axis intercept have changed considerably. Specifically for the y-axis intercept, has decreased from -4.25 to -4.29. Again, if we remove the log term, this increase would correspond to a factor of 1.09 which is quite reasonable. Nonetheless, the original constant term (10.520) from Suito's correlation was also revised to take into account this new y-axis intercept for a temperature of 1600°C.

The revised correlation combining Suito's and Basu's data is given by:

$$\log \frac{(\%P)}{[\%P](T.Fe)^{\frac{5}{2}}} = 0.068 \left[ (\%CaO) + 0.42(\%MgO) + 1.16(\%P_2O_5) + 0.2(\%MnO) \right] + \frac{11570}{T} - 10.467 \quad (5.1)$$

In the previous equation the temperature dependence is the same as presented earlier in Section 3.1 but the intercept has been adjusted from 10.563 to 10.467 in order to meet the predicted intercept of -4.29 at 1600°C. The MgO coefficient increased by a factor of 2.77, the P<sub>2</sub>O<sub>5</sub> coefficient has also increased by a factor of 1.93 but the MnO coefficient has decreased by a factor of 0.33. It should be noted that the typical concentration of these three oxides are usually low with respect to CaO, FeO and SiO<sub>2</sub> and their overall effect on the partition ratio is relatively small.

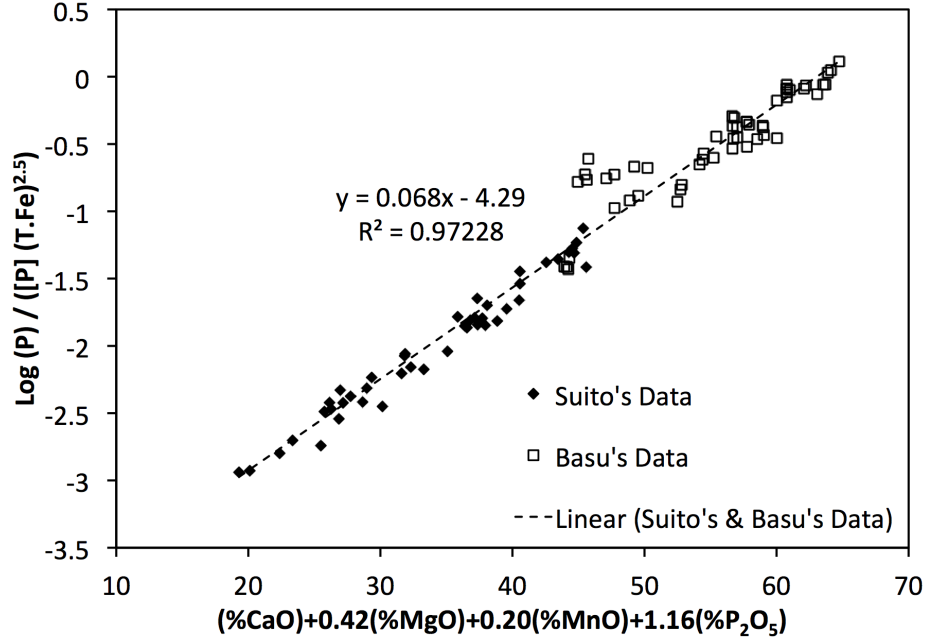


Figure 5.2: Revised Suito's correlation including Basu's data.

Although the new correlation represents some improvement over the previous ones, some disagreement is still present in Figure 5.2. It is interesting to note that this data represents the experiments made by Basu with high  $\text{P}_2\text{O}_5$  content in the slag, ranging from 3 wt.% to 7 wt.%.

Given these disagreements, a set of equilibrium experiments was carefully planned and executed. The experimental approach, results and discussion are presented in the following sections.

## 5.2 Technical Approach

In the present work, phosphorus equilibrium was approached from both metal and slag sides. To do this, experiments were almost always run in pairs, with one sample transferring phosphorus from the metal to the slag, i.e. *dephosphorization*, and



another sample transferring phosphorus from the slag to the metal, i.e. *phosphorus reversion*. Therefore, a two-phase slag-metal equilibrium was established, which it is faster than a three-phase equilibrium with gaseous species. Once equilibrium is set, the phosphorus partition, that is, the ratio between the phosphorus content in the slag and in the metal must be the same for the two samples. The slag system used was  $\text{CaO-SiO}_2\text{-MgO-FeO-P}_2\text{O}_5$  and different slag and alloy compositions were tested. The materials and experimental apparatus are described below.

### 5.2.1 Raw Materials

#### Master Fe-P Alloys

Two Fe-P master alloys were used for the equilibration experiments. For the most part, an Fe-P alloy containing 0.043 wt.% phosphorus (designated MA1) was utilized. The phosphorus content of MA1 is in the range of typical hot metal refining. A second P rich alloy containing 0.2 wt.% P (designated MA2) was used for a secondary set of equilibrium experiments when the phosphate capacity of the slag proved to be too high and dephosphorization would occur to such an extent that the measurement of phosphorus in the metal phase would be below the detection limits of the equipment used for chemical analysis. This will be further explained in Sections 5.3 and 5.4.

MA1 was melted in an induction furnace under high purity argon atmosphere using a magnesia crucible. Phosphorus was added in the form of iron phosphide in conjunction with electrolytic iron. MA2 was kindly provided by United States Steel Corporation in the form for a rectangular slab measuring roughly 14cm x 7cm x 20cm. The complete chemical analysis for MA2 is shown in Table 5.1

Each of the master alloys were cut to smaller sizes, roughly 1-3 cm<sup>3</sup> to facilitate handling and weighing.

Table 5.1: Chemical composition of the master alloy MA2.

%Mn	%P	%Ni	%Cr	%Mo	%V	%Al	%C	%S	%O	%N
0.011	0.201	0.003	0.002	0.001	0.002	0.002	0.0008	0.0012	0.0737	0.0005

### Master Slag

A pre-melted master slag was prepared with a composition in the lower range of basicity ( $\%CaO/\%SiO_2$ ) found in steelmaking slags. Reagent grade  $CaO$ ,  $MgO$  and  $SiO_2$  were dried for 8 hours in air at  $900^\circ C$ . The materials were then weighed, mixed, placed in a carbon crucible and heated up to  $1600^\circ C$  in a resistance box furnace. High purity argon was used to set the atmosphere. A heating rate of  $15^\circ C/min$  was used and the slag was held at  $1600^\circ C$  for 3 hours. The furnace was then opened and the slag poured on a steel boat cooled in a water bath. After cooling, the slag was crushed and pulverized into powder.

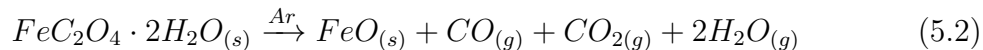
Decarburization of the slag was achieved by heating the pulverized slag to  $1200^\circ C$  and holding it for 10 hours in air. The slag was analyzed by West Penn Testing Group using X-Ray Fluorescence (XRF) and LECO combustion analysis for carbon content. Table 5.2 shows the target and final chemical composition for the master slag.

Table 5.2: Target and Final Master Slag Composition.

	wt.%CaO	wt.%SiO <sub>2</sub>	wt.%MgO	wt.%C
Target	45.00	45.00	10.00	0.000
Final	44.67	44.72	9.98	0.035

## FeO

FeO was synthesized in two ways. A first batch was prepared by mixing reagent grade  $\text{Fe}_2\text{O}_3$  with a slight excess of electrolytic metallic iron and melted in a MgO crucible under argon atmosphere. Upon cooling the crucible was cracked, the FeO-Fe mixture was pulverized and any traces of magnetic material was removed by magnetic separation. This FeO was used for the majority of equilibrium experiments except for the last three experiments. The second batch of FeO was synthesized by heating iron oxalate,  $\text{FeC}_2\text{O}_4 \cdot 2\text{H}_2\text{O}$ , to  $1000^\circ\text{C}$  in an iron crucible exposed to an ultra-high purity argon atmosphere for 1 hour according to the reaction:



this batch was used for the last three equilibrium experiments. The X-ray diffraction pattern for both batches is shown in Figures 5.3 and 5.4.

## $\text{Ca}_2\text{P}_2\text{O}_7$ and Other Materials

Phosphorus was added to the slag in the form of reagent grade calcium pyrophosphate ( $\text{Ca}_2\text{P}_2\text{O}_7$ ). Other oxide additions such as reagent grade CaO, MgO and  $\text{SiO}_2$  were also used to achieve the desired slag composition for each experiment.

### 5.2.2 Furnace

A horizontal resistance tube furnace was used for all equilibrium experiments. The furnace was manufactured by CM Furnaces Inc., model name 1730-12 HTF containing 10 MoSi<sub>2</sub> heating elements and a maximum operating temperature of  $1700^\circ\text{C}$ . The reaction tube was made of high density alumina tube, measuring 79.3mm ID x 88.9mm

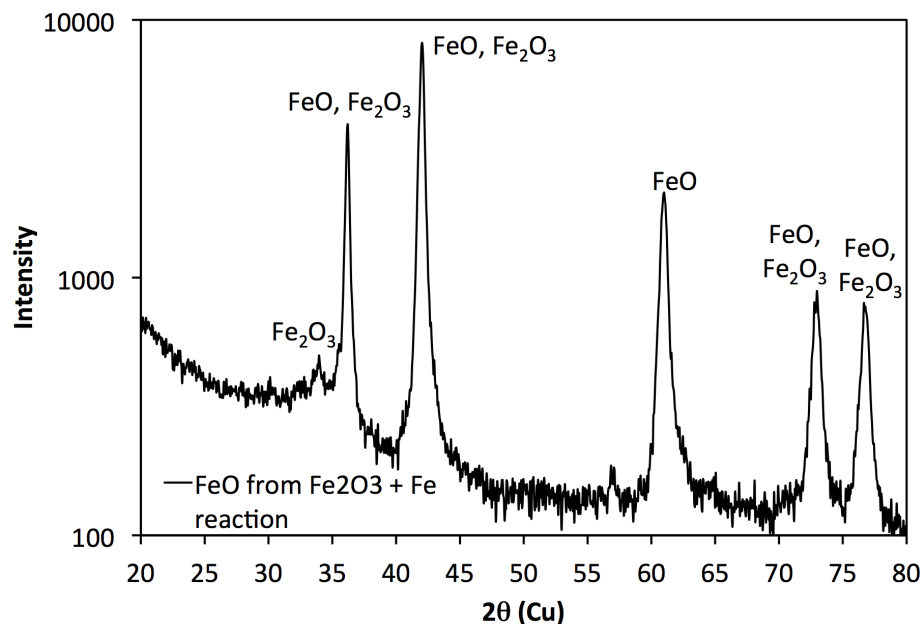


Figure 5.3: XRD of FeO synthesized from  $\text{Fe}_2\text{O}_3 + \text{Fe}$  reaction.

OD x 1066.8mm L, sealed from both sides using water cooled steel lids and Viton fluoroelastometer gaskets. A schematic diagram of the experimental setup is shown in Figure 5.5.

The crucibles containing the samples were placed onto a magnesia tray, which was then placed inside the horizontal alumina tube at the hot zone. Both ends were sealed, allowing only the ultra high purity argon stream to enter and leave the furnace from opposite sides. The flow rate was controlled by a mass flow controller programmed for 0.2 liters per minute of Argon (STP).  $\text{MoSi}_2$  heating elements provide the heat from outside of the alumina tube and a type B thermocouple, placed on the outside wall of the alumina tube, is connected to the temperature controller.

All equilibrium experiments were performed at  $1600^\circ\text{C}$  with a heating rate of  $2^\circ\text{C}$  per minute.

The furnace was calibrated to  $1600^\circ\text{C}$  by inserting a type B thermocouple from

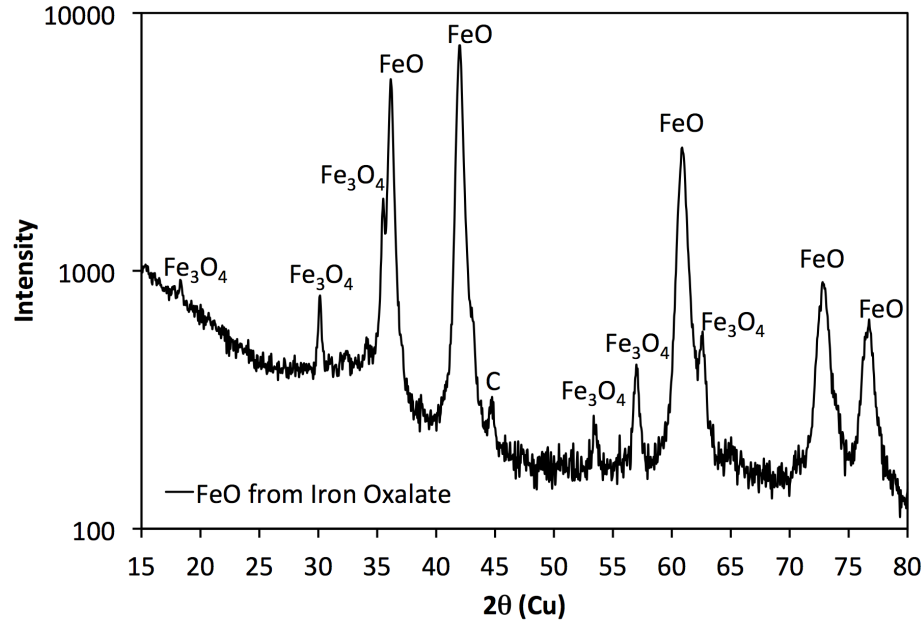


Figure 5.4: XRD of FeO synthesized from Iron Oxalate.

the right side end cap through an opening specially designed to maintain the thermocouple stable and its position roughly at the radial center of the tube. Temperature was measured in intervals of 2cm from the beginning of the alumina tube until the hot zone was reached. At the hot zone, the temperature was manually raised until the thermocouple inside the furnace would read  $1600^{\circ}\text{C} \pm 2^{\circ}\text{C}$ . The temperature calibration was periodically checked every time the alumina tube was replaced. On average, the furnace would have to be set to  $1645^{\circ}\text{C} \pm 5^{\circ}\text{C}$  in order to achieve  $1600^{\circ}\text{C}$  at the hot zone.

### 5.2.3 Crucible Selection

Crucible options were limited due to the nature of the slags used for the experiments. As will be mentioned in Section 5.2.4, the slags were very close to MgO saturation. In this case, the only reasonable crucible choice was high density MgO crucibles for

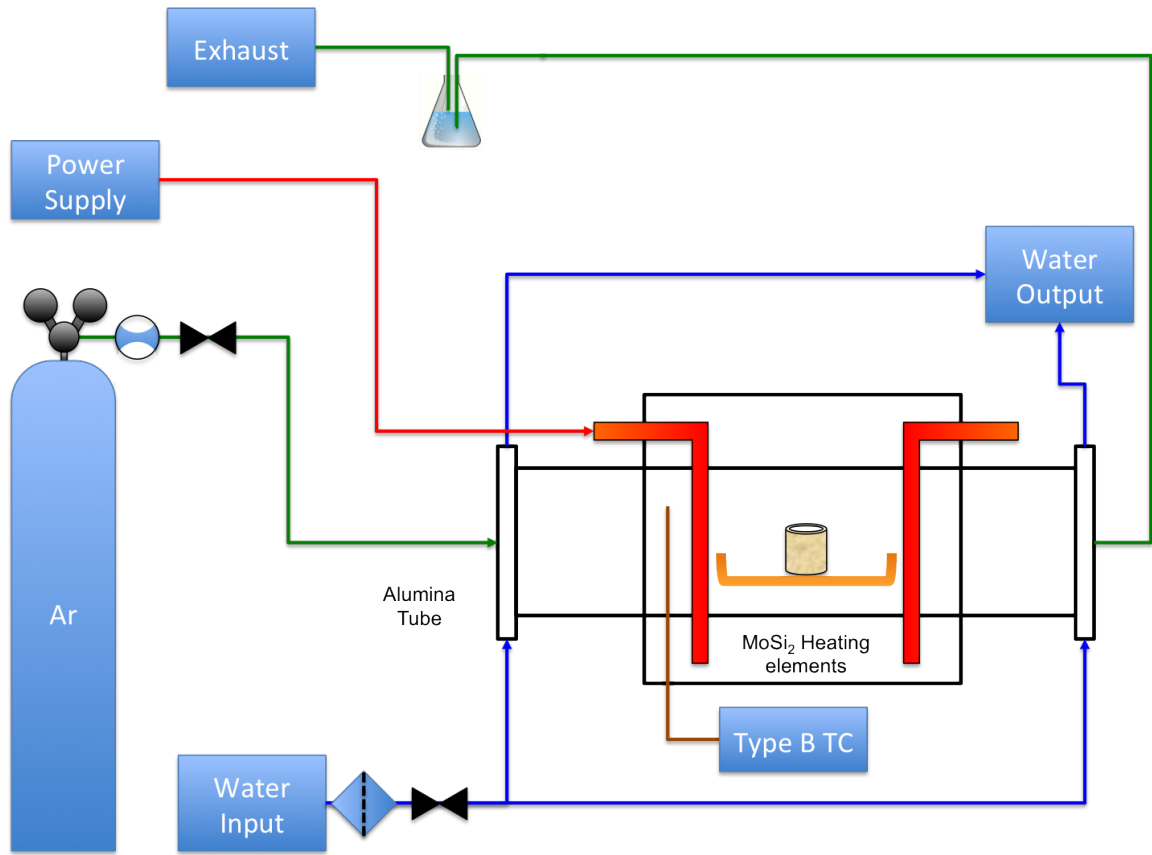


Figure 5.5: Diagram of experimental setup.

all equilibrium experiments. Using MgO crucibles with a MgO saturated slag reduces the risk of crucible dissolution and slag infiltration into the crucible, which would increase the MgO content of the slag with time, both of which are not desirable. The dimensions of the crucibles were 21.5mm ID x 25.5mm OD x 31.7mm H.

## 5.2.4 Experimental Procedure

### Slag Design

The slag compositions were designed using the *Equilib* module of the software package FactSage to ensure that a fully liquid slag would form at 1600°C. The example below

describes the FactSage protocol for designing a slag of ( $\%CaO/\%SiO_2$ ) ratio of about 3.0. A similar protocol was used for designing the vast majority of the slags used in this study.

- FactSage setup:
  - Databases: FactPS, FToxid and FSstel.
  - Units: temperature -  $^{\circ}C$ , pressure - atm, energy - J, mass - g, volume -  $dm^3$ .
- Initial species and quantities:
  - For 100 grams of slag with binary basicity of 3.0:
    - \*  $CaO = 56.25g$
    - \*  $SiO_2 = 18.75g$
    - \*  $MgO = 10g$  (note that the initial MgO content is well above the expected saturation of about 3 to 6wt.%)
    - \*  $FeO = 15g$
    - \*  $Fe = 100g$
- Phases considered:
  - Ideal gas
  - Liquid steel (FSstel-LIQU)
  - Liquid Slag (FToxid-SLAGA)
  - Spinel (FToxid-SPINA)
  - Monoxide (FToxid-MeO\_A)
  - Dicalcium silicate (FToxid-bC2S and FToxid-aC2S)

```

48.296      gram  ASlag-liq#1
(48.296 gram, 0.80766 mol)
(1600 C, 1 atm,      a=1.0000)
( 19.005      wt.% SiO2      FToxid
+ 52.645      wt.% CaO      FToxid
+ 23.942      wt.% FeO      FToxid
+ 1.3700      wt.% Fe2O3    FToxid
+ 3.0383      wt.% MgO      FToxid)

Site fraction of sublattice constituents:
Si              0.18818
Ca              0.55851
Fe2+            0.19826
Fe3+            1.0208E-02
Mg              4.4848E-02
-----
O              1.0000

System component      Mole fraction      Mass fraction
Fe                    9.5047E-02      0.19568
Ca                    0.25464      0.37625
Si                    8.5798E-02      8.8837E-02
Mg                    2.0448E-02      1.8322E-02
O                     0.54406      0.32091

```

Figure 5.6: Liquid slag predicted by FactSage using initial values from the first attempt to design a liquid slag with binary basicity of 3.0.

– Olivine (AOlivine)

- Temperature: 1600°C
- Pressure: 1 atm

For the aforementioned inputs, the predicted liquid slag from FactSage would be 52.645 wt.% CaO, 19.005 wt.% SiO<sub>2</sub>, 23.942 wt.% FeO, 1.370 wt.% Fe<sub>2</sub>O<sub>3</sub> and 3.038 wt.% MgO as shown in Figure 5.6. Note that the liquid slag has a binary basicity of 2.77 instead of the desired value of 3.0. In these cases, iterative calculations were performed incrementally adding FeO until the desired basicity for the liquid slag would reach the target. For the example above, that is achieved by using the following initial quantities.

- For 100 grams of slag with binary basicity of 3.0:

– CaO = 46.5g



```

90.188      gram  ASlag-liq#1
(90.188 gram, 1.4986 mol)
  (1600 C, 1 atm,      a=1.0000)
  ( 17.186      wt.% SiO2
+ 51.265      wt.% CaO
+ 26.902      wt.% FeO
+ 1.5261      wt.% Fe2O3
+ 3.1204      wt.% MgO
                                     FToxid
                                     FToxid
                                     FToxid
                                     FToxid
                                     FToxid)

Site fraction of sublattice constituents:
Si                      0.17116
Ca                      0.54702
Fe2+                   0.22406
Fe3+                   1.1437E-02
Mg                     4.6327E-02
-----
0                      1.0000

System component      Mole fraction  Mass fraction
Fe                   0.10818      0.21978
Ca                   0.25129      0.36639
Si                   7.8625E-02    8.0335E-02
Mg                   2.1281E-02    1.8817E-02
0                   0.54063      0.31468

```

Figure 5.7: Liquid slag predicted by FactSage with binary basicity of 3.0 using iterative approach of adding more FeO as a slag flux.

- $\text{SiO}_2 = 15.5\text{g}$
- $\text{MgO} = 10\text{g}$  (note that the initial MgO content is well above the expected saturation of about 3 to 6wt.%)
- $\text{FeO} = 28\text{g}$
- $\text{Fe} = 100\text{g}$

The resulting liquid slag would now be 51.265 wt.% CaO, 17.186 wt.%  $\text{SiO}_2$ , 26.902 wt.% FeO, 1.5261 wt.%  $\text{Fe}_2\text{O}_3$  and 3.1204 wt.% MgO as shown in Figure 5.7. Note that this slag has a basicity of 2.98. This composition would then be used as the initial target composition when weighing the materials for an experiment containing a slag with basicity of 3.0.

## Laboratory Procedure

The same experimental procedure was used for all equilibrium experiments. The procedure can be summarized in the steps as described below:

1. Weighing of the raw materials: 18 grams of metal and 8 grams of slag were used for most experiments. In some cases, only 6 grams of slag were used. If extra additions to achieve the desired initial slag composition were necessary (like CaO, FeO or  $\text{Ca}_2\text{P}_2\text{O}_7$ ) a mixing step was added in order to homogenize the powders prior to placing the slag into the crucible.
2. Loading of the crucible: The steel phase was added to the bottom of the crucible. In order to ensure proper separation between steel and slag and to avoid initial slag inclusions, a high purity iron disk was placed on the top of the Fe-P master alloy to provide proper separation of phases. The mixed slag was then placed on the top of the iron disk.
3. Loading of the furnace: The loaded crucible was placed into a magnesia tray, which was then placed at the furnaces hot zone and the argon flow was started at a rate of 0.2 liters per minute (STP).
4. Furnace cycle: The furnace was sealed and programmed for a heating rate of  $2^\circ\text{C}/\text{min}$  until it reached  $1600^\circ\text{C}$ . The temperature was then held for 10 hours to ensure that equilibrium had been reached. The temperature then quickly dropped to  $1300^\circ\text{C}$  at a rate of around  $-35^\circ\text{C}/\text{min}$  to ensure rapid solidification of the sample and held there for 10 minutes. The cooling rate was then resumed to the same  $2^\circ\text{C}/\text{min}$  experienced during heat up. Upon cooling, the furnace was opened and the sample was removed.

5. Sample preparation: In order to recover the slag and the metal phases, sand paper #60 was used to grind off the crucible in a polishing machine with the speed set between 200 to 300 rpm. For several samples, the slag and metal would usually detach from each other without major difficulties after the crucible would have been ground. Some samples would require the use of a hammer to physically separate the slag and metal. After the separation, the metal phase was sanded using #120 sand paper to remove any traces of slag on the surface.
6. Slag analysis: All slags were analyzed by Energy Dispersive X-Ray Fluorescence (EDXRF). West Penn Testing was the laboratory that carried the analysis. A phosphorus standard traceable to NIST at a level of 3.50 wt.% phosphorus was used as well as Ausmon standard used to check the equipment daily.
7. Metal analysis: most of the metal samples were analyzed by Inductively Coupled Plasma Mass Spectrometry (ICP-MS). Some metal samples were analyzed by Inductively Coupled Plasma Optical Emission Spectrometry (ICP-OES) later in the course of the project.

## 5.3 Results

Phosphorus transfer was approached from both sides, that is, from metal to slag and slag to metal, whenever possible to ensure thermodynamic equilibrium was achieved. For every furnace cycle, from 2 to 6 samples were placed at the hot zone following the procedure described in Section 5.2.4.

Sample coding was designed to provide all the relevant information about the sample at a glance. It consists of two capital letters followed by four or five numbers, e.g. MS1105. Where *M* and *S* stand for *metal* and *slag* respectively. The first

numerical digit refers to the only master slag used, where 1 corresponds to the master slag shown in Table 5.2. The second digit refers to the master alloy used and can have values of either 1 or 2 corresponding to MA1 or MA2 respectively as described in Section 5.2.1. The next two digits refer to the number of the experiment in the order it was performed. Therefore, MS1105 means that phosphorus was transferred from the *metal* to the *slag*, i.e. dephosphorization; used the master slag from Table 5.2 plus whatever additions were necessary; used master alloy MA1 and it was the fifth experiment performed. The initial calculated slag and metal compositions are shown in Table 5.3.

Table 5.3: Calculated initial slag and metal compositions.

Sample	%CaO	%MgO	%P <sub>2</sub> O <sub>5</sub>	%SiO <sub>2</sub>	%Fe <sub>t</sub> O	%P
MS1101	41.08	4.05	1.43	17.69	27.79	0.04
SM1101	40.97	4.02	1.66	17.56	27.82	0.00
MS1102	48.76	4.18	1.39	18.75	20.93	0.04
SM1102	48.66	4.17	1.60	18.69	20.89	0.00
MS1103	51.42	3.06	1.42	18.39	20.00	0.04
SM1103	51.30	3.06	1.63	18.32	19.97	0.00
MS1104	52.15	2.97	1.43	17.40	20.25	0.04
SM1104	52.05	2.97	1.63	17.29	20.25	0.00
MS1105	49.31	3.18	1.42	15.43	23.84	0.04
SM1105	49.19	3.18	1.64	15.35	23.82	0.00
SM1106	46.88	3.22	1.64	13.85	26.74	0.00
MS1107	46.71	3.10	1.40	12.98	27.84	0.04
SM1107	46.56	3.09	1.63	12.94	27.82	0.00
MS1108	42.39	4.50	1.43	16.95	26.99	0.04
SM1108	42.12	4.46	1.65	16.92	27.09	0.00
MS1109	46.93	3.65	1.46	17.09	24.00	0.04
SM1109	46.83	3.74	1.65	17.38	23.63	0.00
MS1110	50.36	3.17	1.42	17.30	21.58	0.04
SM1110	50.05	3.17	1.61	17.32	21.65	0.00
SM1111	48.22	3.27	1.65	15.79	24.16	0.00
MS1112	48.48	3.22	1.48	14.71	24.97	0.04
SM1112	48.28	3.21	1.63	14.53	25.16	0.00
MS1201	50.85	4.00	1.42	20.34	18.18	0.20
MS1202	51.36	3.70	1.42	19.80	18.44	0.20
MS1203	51.98	3.50	1.41	19.28	18.52	0.20
MS1204	52.48	3.30	1.44	18.76	18.67	0.20
MS1205	52.98	3.20	1.43	18.29	18.74	0.20
MS1206	53.34	3.10	1.43	17.78	18.93	0.20
MS1207	39.20	3.23	1.55	14.96	31.92	0.00
SM1207	34.42	3.59	2.18	17.06	33.24	0.20
SM1208	48.14	3.00	2.44	18.53	21.68	0.00
MS1209	49.46	4.99	1.44	17.86	20.41	0.20
MS1210	46.54	5.65	1.29	19.57	20.95	0.20
MS1211	42.41	4.51	1.42	16.97	26.97	0.20
SM1211	41.59	4.56	2.54	16.62	26.98	0.00
SM1212	45.56	4.51	2.53	16.58	23.95	0.00

### **5.3.1 Visual Observations**

After the experiment, a few samples were mounted in epoxy, cross-sectioned and polished for visual examination of the metal and slag phases. Figure 5.8 shows the cross-sectional area of a typical sample mounted in epoxy. It can be seen that the metal/slag interface is well defined. The slag nicely wets the magnesia crucible while the metal phase does not exhibit wetting behavior. Also, slag penetration and crucible dissolution was usually small, indicating that, in fact, the slag was somewhat close to the predicted MgO saturation.

### **5.3.2 Chemical Analysis Results**

As previously mentioned in Section 5.2.4, the slag phase was analyzed by XRF and the metal phase by ICP-MS. Table 5.4 shows the raw data obtained from the chemical analysis for both metal and slag.

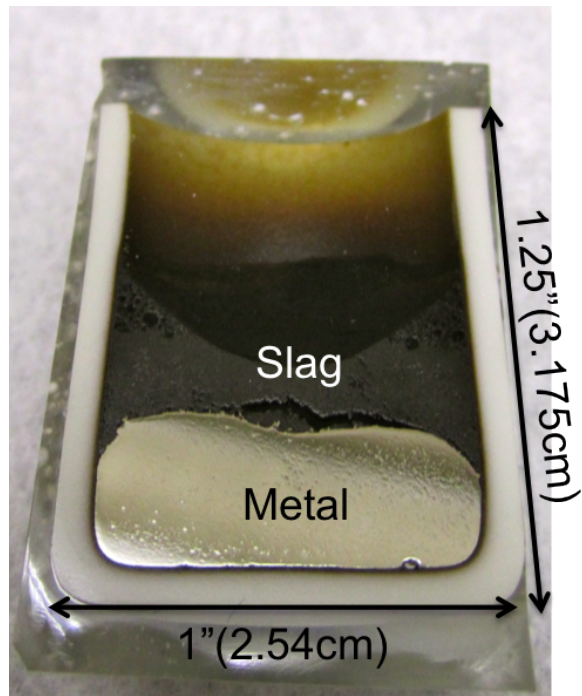


Figure 5.8: Cross sectional area of a typical sample mounted in epoxy and polished.

Table 5.4: Reported values from chemical analysis for slag and metal. Species marked with “–” were not analyzed.

Sample	%CaO	%MgO	%P <sub>2</sub> O <sub>5</sub>	%SiO <sub>2</sub>	%Fe <sub>t</sub> O	%P
MS1101	–	6.05	1.51	–	29.48	0.0040
SM1101	–	5.82	1.52	–	29.68	0.0040
MS1102	–	–	1.67	–	22.01	0.0010
SM1102	–	5.53	1.62	–	20.78	0.0010
MS1103	–	4.77	1.74	–	19.31	0.0016
SM1103	–	4.82	1.85	–	–	0.0017
MS1104	–	6.83	1.34	–	37.90	0.0010
SM1104	–	6.23	1.54	–	32.16	0.0009
MS1105	–	5.99	1.35	–	40.88	0.0010
SM1105	–	4.57	1.81	–	27.06	0.0012
SM1106	43.60	5.66	1.67	12.69	32.23	0.0007
MS1107	43.64	5.02	1.69	12.35	33.17	0.0004
SM1107	44.10	4.98	1.75	12.51	32.58	0.0005
MS1108	43.63	5.59	2.20	18.02	27.23	0.0011
SM1108	–	5.38	1.82	–	29.21	0.0013
MS1109	47.28	4.54	1.91	19.54	23.69	0.0009
SM1109	–	4.50	1.97	–	22.90	0.0009
MS1110	51.26	4.15	2.01	19.08	20.91	0.0013
SM1110	–	4.70	1.82	–	21.84	0.0013
SM1111	–	4.60	1.66	–	25.77	0.0014
MS1112	47.87	5.05	1.68	15.58	26.62	0.0008
SM1112	–	5.51	1.65	–	25.10	0.0009
MS1201	48.62	4.98	2.70	21.08	19.92	0.0016
MS1202	48.55	4.37	2.63	21.33	19.66	0.0021
MS1203	49.87	4.36	2.66	20.32	20.20	0.0011
MS1204	50.24	4.16	2.71	19.99	20.30	0.0012
MS1205	50.09	4.24	2.67	19.04	21.28	0.0010
MS1206	50.63	4.15	2.60	18.61	21.35	0.0011
MS1207	37.17	7.10	2.86	13.98	34.56	0.0013
SM1207	35.86	9.00	2.54	17.30	31.34	0.0016
SM1208	43.66	6.09	2.42	16.60	27.74	0.0010
MS1209	48.04	7.45	2.91	20.26	18.86	0.0008
MS1210	50.10	6.68	3.07	18.40	19.23	0.0011
MS1211	43.79	6.52	3.02	17.34	25.99	0.0010
SM1211	46.68	7.24	2.96	17.27	22.93	0.0011
SM1212	42.46	6.65	2.80	16.70	27.84	0.0008



The majority of the equilibrium slag samples were analyzed for  $\text{CaO}$ ,  $\text{SiO}_2$ ,  $\text{Fe}_t\text{O}$ ,  $\text{MgO}$  and  $\text{P}_2\text{O}_5$ . The species not analyzed of a certain sample are indicated with a “\_”.

## 5.4 Discussion

From Table 5.4, it can be seen that some samples were not completely analyzed. This is especially true for the set of experiments where only the concentration of the critical species were analyzed. It was later decided that full slag analyses was to be carried for the experiments that followed. For these samples, it was assumed constant weight of the species not analyzed.

### 5.4.1 Chemical Analysis Estimate and Correction

#### CaO and $\text{SiO}_2$

Several samples were not analyzed for the final  $\text{CaO}$  and  $\text{SiO}_2$  contents, especially in the first half of experiments as it can be seen in Table 5.4. The assumption was that, ideally, the initial and final  $\text{CaO}$  and  $\text{SiO}_2$  amounts of the slag should not change during the phosphorus reaction. However, the  $\text{CaO}$  powder presented a small amount of unexpected hydration. This was checked by heating the  $\text{CaO}$  powder above the calcination temperature ( $1000^\circ\text{C}$ ) for 10 hours and checking the delta in the measured weight. The measured weight loss was around 2% of the initial  $\text{CaO}$  mass. It was finally decided to correct the  $\text{CaO}$  and  $\text{SiO}_2$  contents in the slag by assuming 2% weight loss of the original  $\text{CaO}$  amount and constant ratio between  $\text{CaO}$  and  $\text{SiO}_2$ .

## MgO

Only one sample was not analyzed for MgO: MS1102. However, since MS1102 and SM1102 have basically the same chemistry, it was assumed that the MgO content for MS1102 was the same as that of SM1102.

## Fe<sub>t</sub>O

The Fe<sub>t</sub>O content in the slags were usually directly taken from the chemical analysis results. However, one can point out that the Fe<sub>t</sub>O contents for samples MS1104, SM1104 and MS1105 are considerably higher than the initial values. If metallic iron was suspended in the slag, it could result in much higher bulk Fe<sub>t</sub>O than expected. On average, the wt.%Fe<sub>t</sub>O changes by -5.41wt.%. This average change was used to correct the Fe<sub>t</sub>O concentrations using its initial weighted value plus the change of -5.41wt.% for the aforementioned samples.

Table 5.5 presents the final corrected results that are used throughout the discussion.

Table 5.5: Corrected equilibrium chemical composition. Values with \* are estimated based on the assumptions discussed in the text.

Sample	%CaO	%MgO	%P <sub>2</sub> O <sub>5</sub>	%SiO <sub>2</sub>	%Fe <sub>t</sub> O	%P	Lp
MS1101	41.57*	6.05	1.51	18.11*	29.48	0.0040	165
SM1101	41.64*	5.82	1.52	18.04*	29.68	0.0040	166
MS1102	49.20*	5.53*	1.67	19.15*	22.01	0.0010	729
SM1102	50.23*	5.53	1.62	19.53*	20.78	0.0010	707
MS1103	52.85*	4.77	1.74	19.18*	19.31	0.0016	475
SM1103	52.75*	4.82	1.85	19.12*	19.31*	0.0017	475
MS1104	51.30*	6.83	1.34	17.37*	20.84*	0.0010	585
SM1104	51.66*	6.23	1.54	17.42*	20.84*	0.0009	747
MS1105	48.87*	5.99	1.35	15.51*	25.47*	0.0010	587
SM1105	48.28*	4.57	1.81	15.28*	27.06	0.0012	656
SM1106	43.85	5.69	1.68	12.76	32.41	0.0007	1047
MS1107	43.84	5.04	1.70	12.41	33.31	0.0004	1852
SM1107	44.30	5.00	1.76	12.57	32.73	0.0005	1535
MS1108	43.76	5.61	2.21	18.07	27.32	0.0011	875
SM1108	42.71*	5.38	1.82	17.64*	29.21	0.0013	611
MS1109	47.47	4.56	1.92	19.62	23.79	0.0009	930
SM1109	48.18*	4.50	1.97	19.91*	22.90	0.0009	955
MS1110	51.40	4.16	2.02	19.13	20.96	0.0013	677
SM1110	50.44*	4.70	1.82	18.77*	21.84	0.0013	611
SM1111	49.05*	4.60	1.66	16.06*	25.77	0.0014	517
MS1112	47.99	5.06	1.68	15.62	26.69	0.0008	919
SM1112	49.00*	5.51	1.65	15.95*	25.10	0.0009	800
MS1201	48.86	5.00	2.71	21.18	20.02	0.0016	740
MS1202	49.18	4.43	2.66	21.61	19.91	0.0021	554
MS1203	50.05	4.38	2.67	20.39	20.27	0.0011	1059
MS1204	50.42	4.17	2.72	20.06	20.37	0.0012	989
MS1205	50.25	4.25	2.68	19.10	21.34	0.0010	1169
MS1206	50.78	4.16	2.61	18.66	21.41	0.0011	1035
MS1207	37.35	7.13	2.87	14.05	34.73	0.0013	965
SM1207	36.03	9.04	2.55	17.38	31.49	0.0016	696
SM1208	43.84	6.12	2.43	16.67	27.85	0.0010	1060
MS1209	48.23	7.48	2.92	20.34	18.93	0.0008	1594
MS1210	50.29	6.71	3.08	18.47	19.31	0.0011	1223
MS1211	43.99	6.55	3.03	17.42	26.11	0.0010	1324
SM1211	46.85	7.27	2.97	17.33	23.02	0.0011	1179
SM1212	42.66	6.68	2.81	16.78	27.97	0.0008	1535

## **The Challenge of Analyzing Low Phosphorus in Iron**

It was a challenge to reliably quantify the equilibrium phosphorus partition when the phosphorus content in the metal was below 20ppm, which was the initial reported reproducible limit for the ICP-MS used at West Penn Testing. Phosphorus contents below 20ppm were not considered reproducible by the aforementioned lab.

In order to evaluate the uncertainty of the measurements, the raw ICP-MS and ICP-OES data was successfully retrieved for all samples from MS1108 to SM1212. The raw data from the older experiments was not available from West Penn Testing. Table 5.6 shows the average and standard deviation for all the aforementioned samples. For some measurements, the uncertainty is quite high, even exceeding the average value in some cases. This is specially true for samples MS1108 to SM1111.

Continuing with the effort to identify suitable techniques to analyze low phosphorus contents in iron, one metal sample was sent to three different labs for chemical analysis using Glow Discharge Mass Spectrometry (GD-MS), ICP-MS and ICP-OES. The results are shown in Table 5.7. This particular sample had a phosphorus content above 20 ppm. The results show that, for phosphorus contents above 20ppm, the measurements are consistent across the three different labs and techniques.

Table 5.6: Average and standard deviation for P analysis in the metal.

Sample	Average P (wt.%)	Standard Deviation
MS1108	0.0011	0.0006
SM1108	0.0013	0.0005
MS1109	0.0009	0.0005
SM1109	0.0009	0.0003
MS1110	0.0013	0.0008
SM1110	0.0013	0.0019
SM1111	0.0014	0.0016
MS1112	0.0008	0.0000
SM1112	0.0009	0.0002
MS1201	0.0016	0.0001
MS1202	0.0021	0.0001
MS1203	0.0011	0.0001
MS1204	0.0012	0.0001
MS1205	0.0010	0.0001
MS1206	0.0011	0.0001
MS1207	0.0014	0.0001
SM1207	0.0016	0.0001
SM1208	0.0010	0.0001
MS1209	0.0008	0.0001
MS1210	0.0011	0.0000
MS1211	0.0010	0.0001
SM1211	0.0011	0.0001
SM1212	0.0008	0.0000

Table 5.7: Analysis results for an alloy containing more than 20ppm using ICP-MS, ICP-OES and GD-MS.

Laboratory	P (ppm)	Technique
Clark Testing	36	ICP-OES
West Penn Testing	38	ICP-MS
Evans Analytical Group	32	GD-MS

A second metal sample containing less than 20ppm P was sent to ICP-MS and ICP-OES. The results for P contents below 20ppm show good agreement as shown in Table 5.8. This part of the project was done in conjunction with Mr. Mohammed Tayeb.

As previously mentioned, the earlier experiments from Table 5.6 had a much greater uncertainty than the ones reported later. It is unclear to the author why this behavior was observed. Finally, the author believes that the vast majority of values reported by ICP-MS or ICP-OES are reasonable even for P contents below 20ppm.

Table 5.8: Analysis results for an alloy containing less than 20ppm using ICP-MS and ICP-OES.

Laboratory	P (ppm)	Technique
Clark Testing	15	ICP-OES
West Penn Testing	12	ICP-MS

Based on the initial target values and the results from chemical analysis, mass balances were conducted with respect to phosphorus to ensure to ensure the initial compositions were consistent with the final compositions. The standard deviation limits were calculated based on the observed mass balance errors for all experiments. From Figure 5.9, most of the data is within one standard deviation and all the data, except for one experiment, is within two standard deviations. Considering that the total amount of phosphorus in the experiments was about 0.5 grams and that very low phosphorus levels in the metal was recurrently achieved, the author believes the uncertainties in the mass balances are reasonable and all experiments are valid.

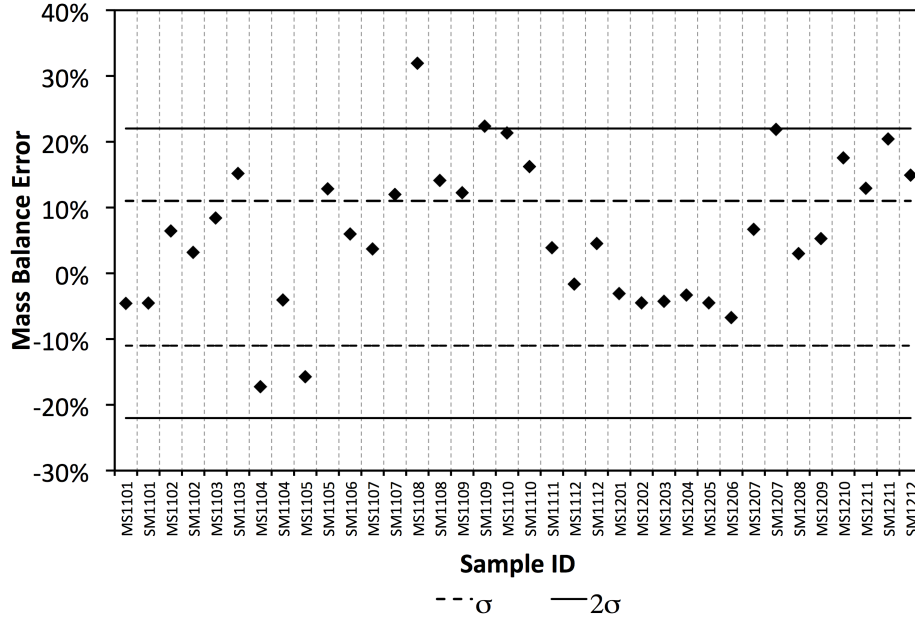


Figure 5.9: Phosphorus mass balance uncertainty between initial target composition and final composition.

### 5.4.2 Equilibrium Phosphorus Partition

Approaching equilibrium from both sides is a good way to ensure thermodynamic equilibrium has been achieved. The phosphorus partition coefficient,  $L_P$ , can be defined as:

$$L_P = \frac{(wt.\%P)}{[wt.\%P]} \quad (5.3)$$

where  $(wt.\%P)$  and  $[wt.\%P]$  correspond to the phosphorus content in the slag and metal respectively. Once equilibrium is set,  $L_P$  should be very similar for the two cases, regardless of which direction phosphorus transfer took place.

Figure 5.10 shows the initial and equilibrium phosphorus partition coefficient for some of the experiments. The dotted lines are only meant to connect the related points for ease of understanding; they do not refer to the rate of the reaction. Most of the experiments showed very good agreement on the final  $L_P$ . This ensures that

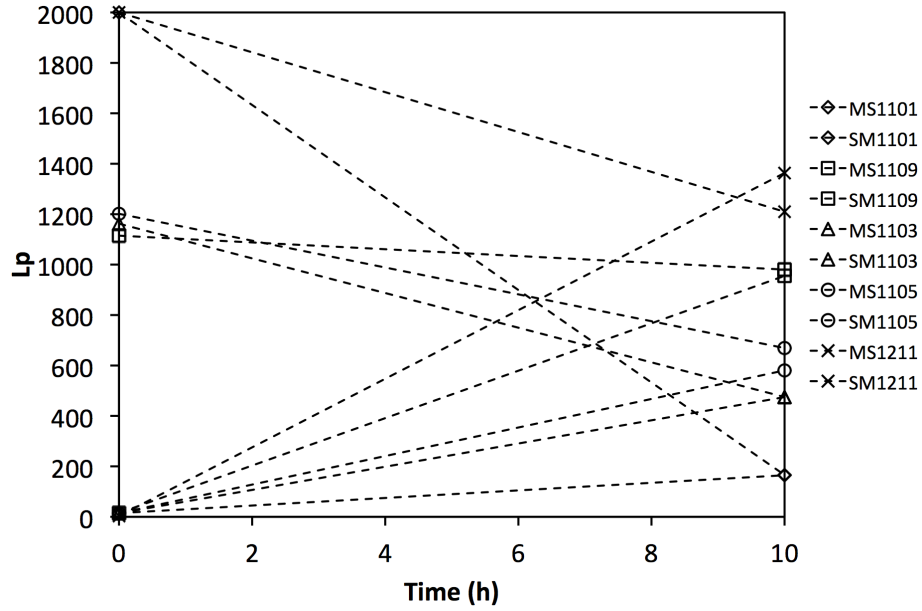


Figure 5.10: Initial and equilibrium phosphorus partition coefficient.

thermodynamic equilibrium is indeed achieved after 10 hours of equilibration time. From Table 5.5 and Figure 5.10 it can be seen that usually the  $L_P$  values are reasonably close, but samples with very low P in the metal can show significant scatter.

The tabulated data from Suito et al. [10, 11], Basu et al. [12, 13], Tayeb et al. [2] and the present work was combined to generate a correlation to illustrate how each set of data fits together. From Figure 5.11, it can be seen that Suito's and Basu's data are consistently below the line while Tayeb's data and the author's data are consistently above the line. This means that the  $L_P$ 's achieved by the author and Tayeb's study are higher than that of the previous authors. When looking only at the range of slag compositions shown in Table 5.5, there are only four data points from Basu's work that fall into such a range and the observed phosphorus partition averages at around 300. The present work, however, observes an average  $L_P$  close to 800, meaning that the amount of phosphorus removed from the metal was much greater than what other authors have observed.



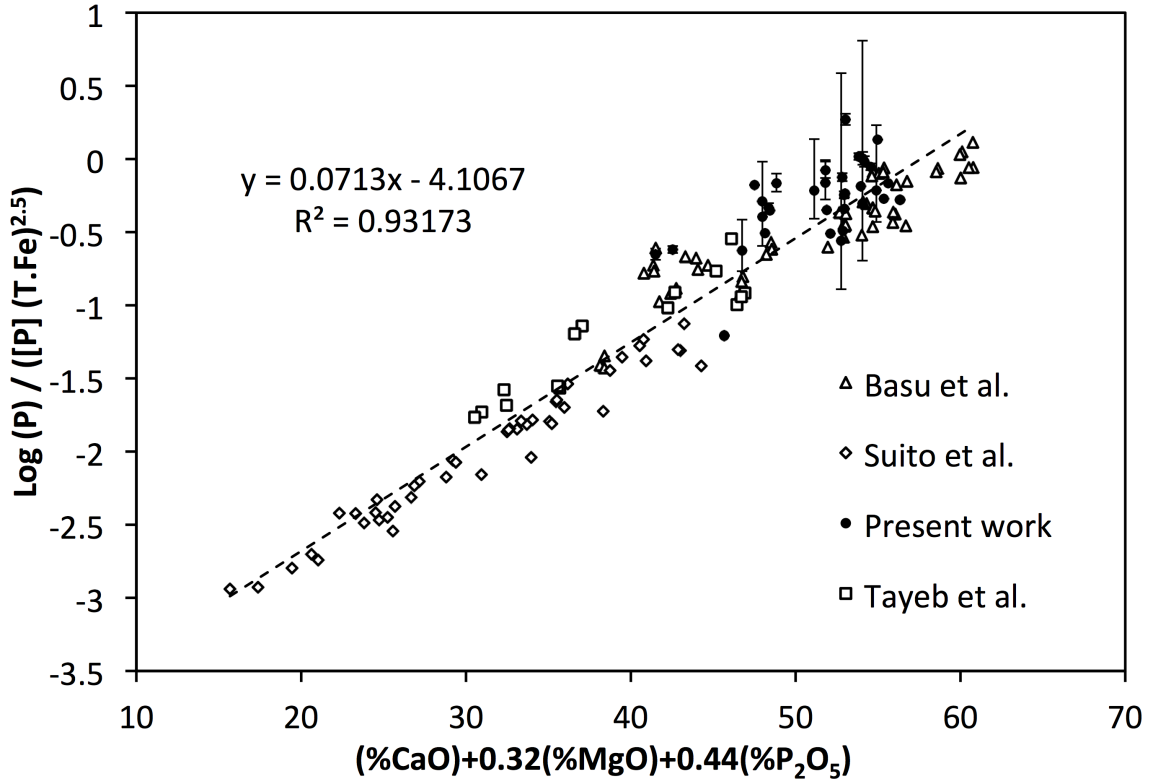


Figure 5.11: Comparison between present work, Tayeb's [2], Suito's [10,11] and Basu's [12,13] data.

In order to understand why the present work and Tayeb's data [2] predict much higher values for  $L_P$ , one must first look at the differences in the experimental procedure adopted by previous studies. The first significant difference is the equilibration time used at a given temperature. In the case of Suito's work, the equilibration time used was between 3 to 6 hours. [10] Basu used a longer equilibration time of 8 hours. On the other hand, the author and Tayeb have used a considerably longer equilibration time of 10 hours. This represents an increase of at least 25% on the reaction time. Therefore, it is a possibility that the previous studies were near to thermodynamic equilibrium but not as close as the more recent data.

Let us now look only at the range of slag compositions studied by the author

and Tayeb. This range is defined in Table 5.9. The data within this range of slag compositions is shown in Figure 5.12. It can be seen that there are a few data points from Basu that are well aligned with the present study in the x-axis but differ considerably in the y-axis as highlighted by the dashed ellipses in Figure 5.12. A scatter in the y-axis is explained by  $L_P$  and/or the total iron in the slag. From Table 5.10, it can be seen that for similar  $(T.Fe)$  contents, the  $L_P$ 's observed by Basu are considerably lower than the observed by the present work. Therefore, the scatter seen on the y-axis is mostly attributed to higher  $L_P$ 's. This reinforces that equilibrium might not have been achieved for all the data from Basu and even possibly from Suito.

Table 5.9: Range of Slag Compositions Studied by the author and Tayeb. [2]

	Max	Min
%CaO	54.01	24.78
%SiO <sub>2</sub>	30.28	12.88
%Fe <sub>t</sub> O	36.12	19.34
%MgO	17.45	4.26
%P <sub>2</sub> O <sub>5</sub>	3.15	0.59

If a Suito's type correlation is derived using only the present work data, the result is no better than the current correlation presented in Equation 5.1. The  $R^2$  parameter drops to 0.84. The author believes that the composition range of the present study is too narrow to be able to generate a better correlation. Another set of data using Electric Arc Furnace (EAF) type slags should broaden the composition range enough to enable a new evaluation of a Suito's type correlation.

Even though a correlation derived only from the present study does not improve the prediction of equilibrium phosphorus partition, it is interesting to note that, if SiO<sub>2</sub> is included in the independent variables (CaO, MgO and P<sub>2</sub>O<sub>5</sub>), the correlation improves from having an  $R^2$  of 0.84 to 0.89 and the interaction coefficient of SiO<sub>2</sub>

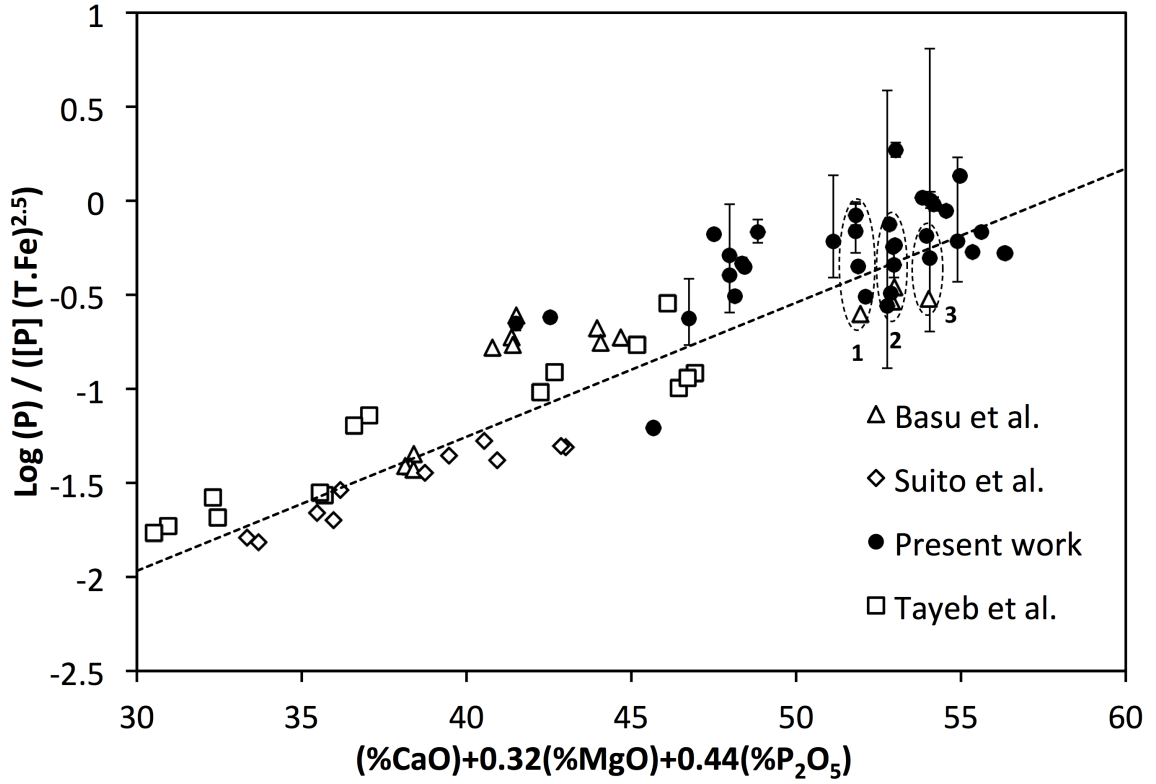


Figure 5.12: Comparison between present work, Tayeb's [2], Suito's [10,11] and Basu's [12,13] data within the slag composition range defined in Table 5.9.

shows as being negative. This means that  $\text{SiO}_2$  has a negative effect in the oxygen ion activity or increases the activity coefficient of phosphorus in the slag.

$$\log \frac{(\%P)}{[\%P](T.Fe)^{\frac{5}{2}}} = 0.072 \left[ (\%CaO) + 0.83(\%MgO) + 5.20(\%P_2O_5) - 0.58(\%SiO_2) \right] + \frac{11570}{T} - 10.520 \quad (5.4)$$

Si is present in the slag in the form of  $\text{SiO}_4^{4-}$  tetrahedra. [14, 43] Each Si atom is surrounded by 4 oxygen atoms forming a tetrahedral structure. These tetrahedral

Table 5.10:  $L_P$  and (T.Fe) data for regions 1, 2 and 3 from Figure 5.12.

Region	Author	Lp	(T.Fe)	Log Lp	-2.5 Log (T.Fe)	Log Lp/(T.Fe) <sup>2.5</sup>
1	Basu	324	17.58	2.51	-3.11	-0.60
	Assis	677	21.69	2.83	-3.34	-0.51
	Assis	980	18.26	2.99	-3.15	-0.16
	Assis	947	21.38	2.98	-3.33	-0.35
	Assis	1210	18.36	3.08	-3.16	-0.08
2	Basu	309	15.13	2.49	-2.95	-0.46
	Basu	311	16.26	2.49	-3.03	-0.53
	Assis	747	17.54	2.87	-3.11	-0.24
	Assis	604	20.37	2.78	-3.27	-0.49
	Assis	533	20.62	2.73	-3.29	-0.56
	Assis	823	20.07	2.92	-3.26	-0.34
	Assis	757	15.91	2.88	-3.00	-0.13
	Assis	566	15.83	2.75	-3.00	-0.25
3	Basu	273	15.24	2.44	-2.96	-0.52
	Assis	724	16.54	2.86	-3.05	-0.19
	Assis	626	17.40	2.80	-3.10	-0.30

form networks or chains by bridging oxygen anions to other tetrahedra, effectively polymerizing the liquid slag. The degree of polymerization has been frequently associated with slag viscosity. For highly basic slags, the cations present, such as  $\text{Ca}^{2+}$  and  $\text{Mg}^{2+}$ , promote breakage of these chains to form non-bridging oxygens and free oxygen anions. This should be related to the oxygen activity in the slag since by breaking the silicate network more oxygen anions are available to react with phosphorus. The degree of depolymerization is usually expressed as the ratio between non-bridging oxygen atoms and tetrahedrally coordinated atoms (NBO/T).

From [14], NBO/T can be computed as follows:

1. Compute the mole fraction of the slag components:  $X_{\text{CaO}}$ ,  $X_{\text{MgO}}$ ,  $X_{\text{P}_2\text{O}_5}$ ,  $X_{\text{SiO}_2}$ ,  $X_{\text{FeO}}$  and ( $X_{\text{Fe}_2\text{O}_3} \sim 0$ )
2. Multiply mole fraction of molecules that contain two metallic cations by 2:

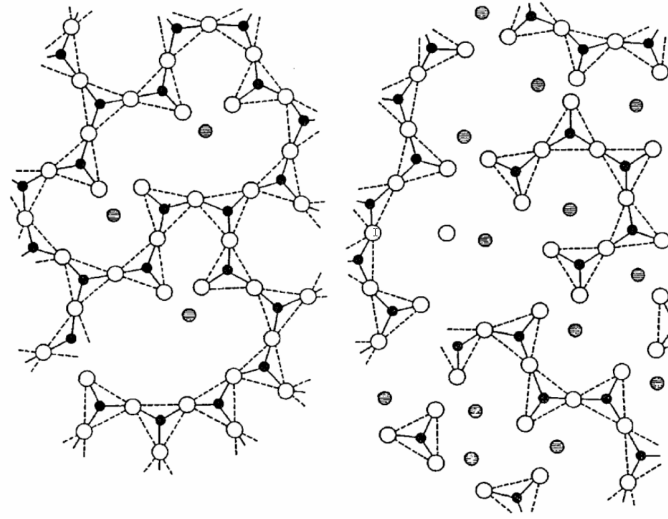


Figure 5.13: Schematic representation of two-dimensional structure of molten silicate slag (a) and depolymerization of the network by dissolution of metal oxides (b). Reproduced from [14]

$$2X_{P_2O_5}, 2X_{Fe_2O_3}$$

3. Sum the mole fractions of the network formers. This corresponds to T:  $X_T = X_{SiO_2} + 2X_{P_2O_5} + F(2X_{Fe_2O_3})$
4.  $F$  is the fraction of  $Fe^{3+}$  in IV coordination and  $(1 - F)$  the fraction in VI coordination. For steelmaking slags,  $F = 0$
5. Compute the total charge of cations that are network breakers:  $y_{NB} = 2(X_{CaO} + X_{MgO} + X_{FeO}) + 6(1 - F)X_{Fe_2O_3}$
6. Compute  $NBO/T = y_{NB}/X_T$

Figure 5.14 shows that as the  $NBO/T$  increases, so does the phosphorus partition ratio,  $L_p$ . Even though the agreement is not particularly good, it can be seen that the higher the fraction of non-bridging oxygen, the higher is the observed  $L_p$ . This work was done in parallel with Tayeb.

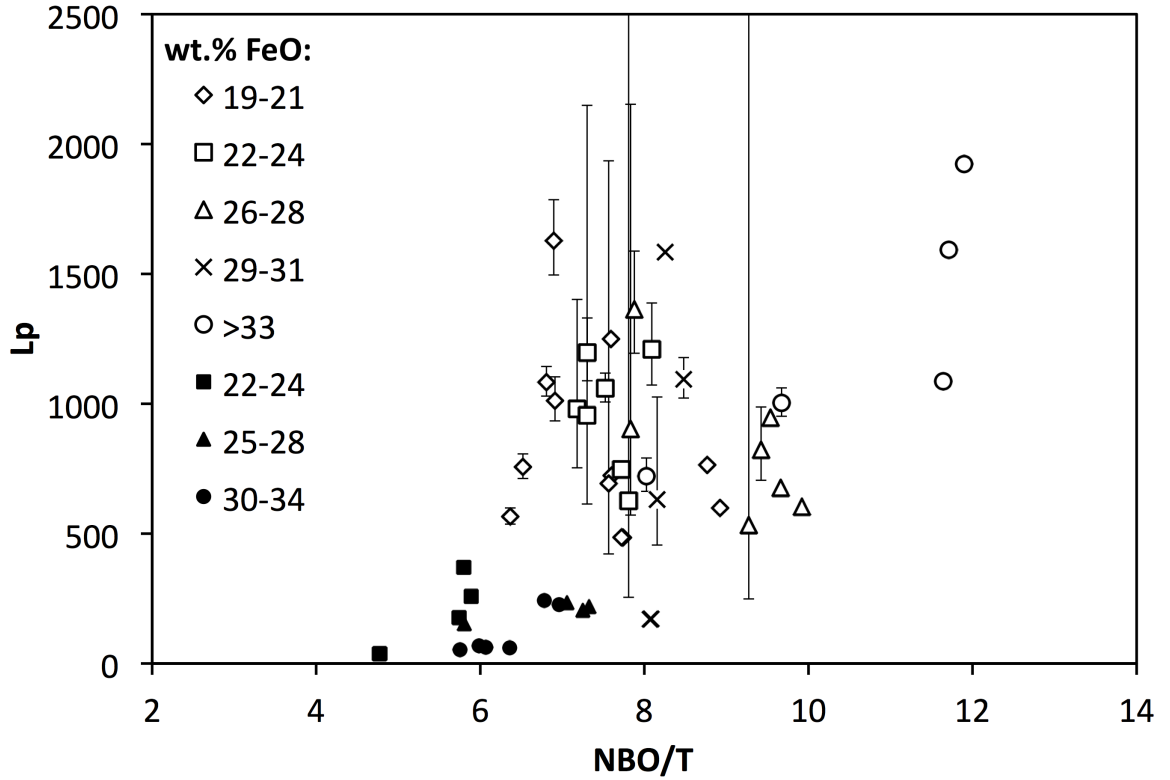


Figure 5.14: NBO/T *vs.*  $L_p$ .  $Fe_tO$  contents in the slag range from 19 to 36 wt.%. Solid data from Tayeb et al. [2].

The notion of slag basicity has also been used to quantify the activity of oxygen anions in the slag. From the acid-base theory of Lux-Flood [56, 57], an acid is a receiver of oxygen anions such as  $SiO_2$  and a base is a donor of oxygen anions such as  $CaO$ . Figure 5.15 shows  $L_p$  *vs.* the  $CaO/SiO_2$  ratio for different FeO contents. The trend is similar to that of NBO/T, with  $L_p$  increasing with basicity. However, for basicities higher than 2.5, it seems that there is no clear function of basicity and FeO content.

Both of these methods are only estimates of how  $L_p$  is related to the oxygen activity in the slag. The author believes they are equivalent and one is not better than the other.

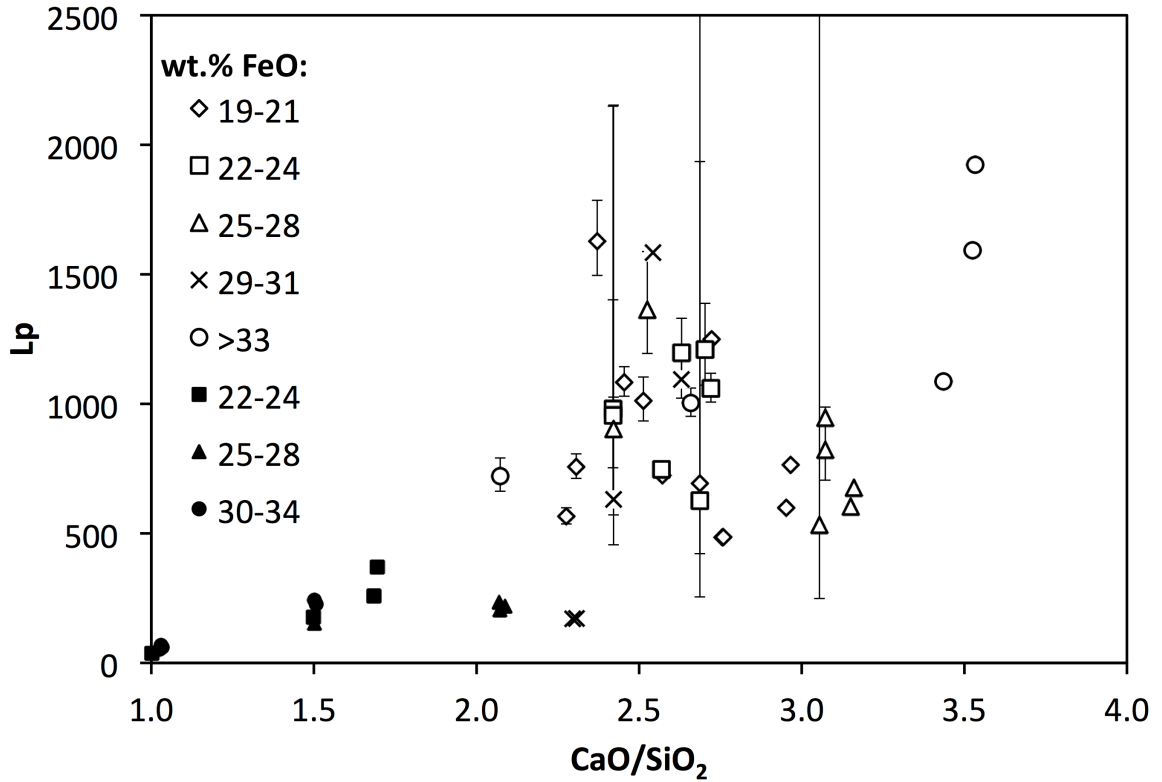


Figure 5.15: Binary Basicity *vs.*  $L_P$ .  $Fe_tO$  contents in the slag range from 19 to 36 wt.%. Solid black symbols from Tayeb et al. [2].

The phosphorus partition ratio should be related to the  $Fe_tO$  content in the slag. Therefore, there should be an optimum  $Fe_tO$  content that provides the highest  $L_P$ . However, as seen on Figure 5.16, there is no clear function of  $FeO$  for the basicity range studied.

As previously mentioned, Basu et al. [12,13], studied phosphorus equilibrium for slags containing from 5 to 25wt.%  $FeO$ . They observed a positive effect of  $FeO$  on  $L_P$  for  $FeO$  contents from 5 to 15wt.%. However, for contents varying from 15 to 25wt.% the effect of  $FeO$  is also unclear. The present work has  $FeO$  contents significantly higher than those used by Basu et al. and it appears that up to 35wt.%  $L_P$  is not greatly influenced by  $FeO$ . It is expected that  $L_P$  would eventually decrease with  $FeO$

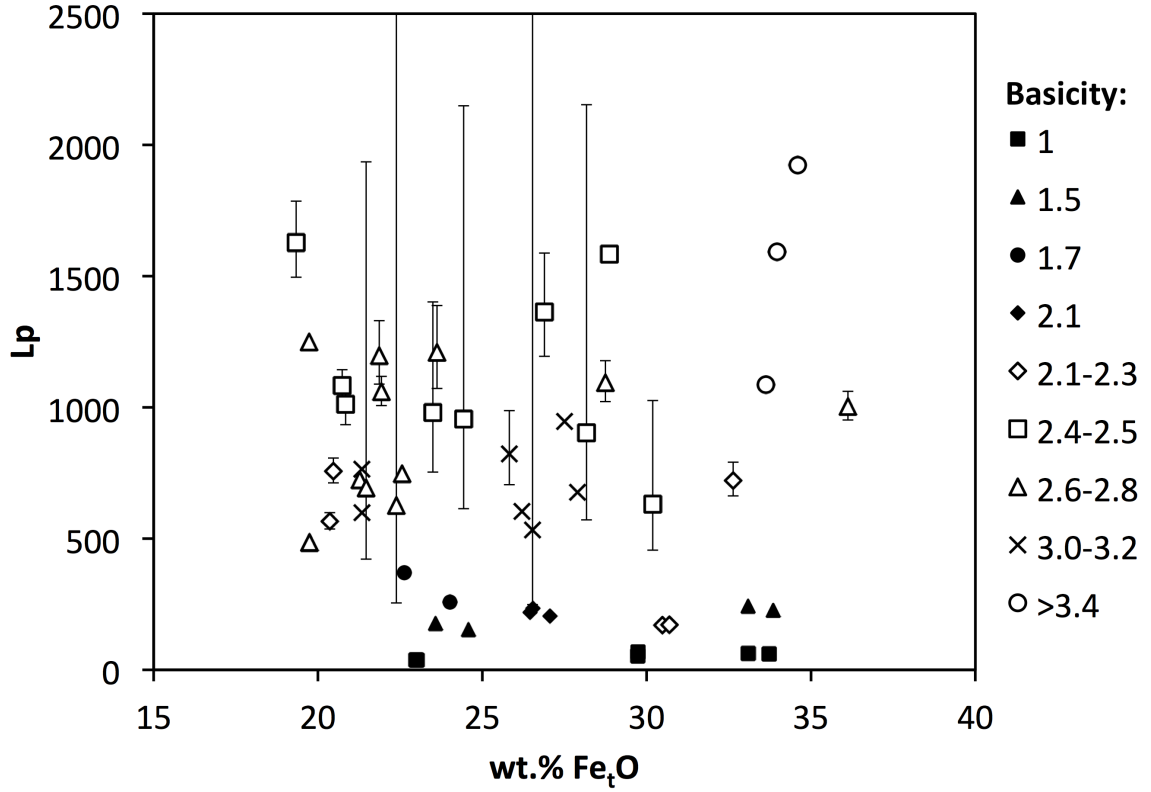


Figure 5.16:  $\text{Fe}_t\text{O}$  vs.  $L_p$ . CaO contents in the slag range from 40 to 52 wt.%. Solid data from Tayeb et al. [2].

due to the dilution of CaO in the slag. Slags containing more than 35wt.% FeO are not relevant for steelmaking and fall outside the scope of the present work.

The experiments presenting very high  $L_P$ 's correspond to slags with the highest binary basicity *and* the highest FeO contents. From Table 5.5, these experiments correspond to SM1106, MS1107 and SM1107. Since FeO and CaO are the most important slag components for dephosphorization, these slags have greater phosphate capacities which result in a very efficient phosphorus removal from the metal.

It should be pointed out that the aforementioned slags are special cases and unusual in common oxygen steelmaking. Normally, high FeO contents in OSM slags are achieved at the expense of CaO and after a certain level of FeO, the  $L_P$  decreases



due to the CaO dilution. However, in the slags being discussed, both FeO and CaO were kept high at the expense of SiO<sub>2</sub> to maintain the desired high basicity.

For all practical purposes, BOF slags with binary basicities above 2.4 and FeO contents of the order of 25 wt.% should promote enough dephosphorization to reach very low P levels in the metal. Therefore, oversaturation of slag with CaO and MgO should be closely monitored in order to maintain optimum bulk slag viscosity.

In summary, phosphorus equilibrium has been evaluated as a function of slag composition. It was shown that for highly basic slags the equilibrium phosphorus partition,  $L_P$ , approaches very high values making chemical analysis in the metal a challenge. Both NBO/T and binary basicities are suitable for semi-quantitative analysis of oxygen ion activity and its impact on  $L_P$ . Slags with Fe<sub>t</sub>O contents of around 22 wt.% are at a local maximum regarding  $L_P$  and, above 31 wt.% Fe<sub>t</sub>O with basicities higher than 3.4, the  $L_P$ 's start reaching even higher values. These slags however, are unusual in oxygen steelmaking.

### **Impact of FeO as a Reactant on $L_P$**

One can argue that because FeO is a reactant, the final slag composition would not be the same for removing or adding phosphorus to the metal phase. To evaluate the approximate impact on  $L_P$  due to FeO being either consumed (dephosphorization) or produced (rephosphorization), let us consider the case of a slag weighing 6 grams and containing 25 wt.% FeO that reacts with 18 grams of Fe containing 0.043 wt.% P (dephosphorization) or 0.0006 wt.% P (rephosphorization). The final P content in the metal is 10ppm for both cases. The impact of FeO on  $L_P$  can be evaluated by rearranging Equation 5.1 as:

$$L_P = 10^a (T.Fe)^{\frac{5}{2}} \quad (5.5)$$

Where  $a$  is a function of slag composition and temperature such as:

$$a = 0.068 \left[ (\%CaO) + 0.42(\%MgO) + 1.16(\%P_2O_5) + 0.2(\%MnO) \right] + \frac{11570}{T} - 10.520 \quad (5.6)$$

and is taken as a constant for a given slag and temperature.

From Table 5.11 the results show that the change on  $L_P$  due to FeO being a reactant would be of 6.85% for a slag initially containing 25 wt.% FeO and assuming constant weight of the metal. The author believes this is a small difference and there are bigger uncertainties on the experiments as will be discussed further in this chapter. The final  $L_P$  on both cases can still be considered very similar.

Table 5.11: Example calculation of how FeO impacts  $L_P$  for dephosphorization and rephosphorization.

	De-P	Re-P
$m_{metal}$ (g)	18.0	18.0
$m_{slag}$ (g)	6.0	6.0
$\%P_{metal}$	0.043	0.0006
$m_{P_{metal}}$ (g)	0.0077	0.00011
$\%FeO_{slag}$	25	25
$m_{FeO_{slag}}$ (g)	1.5	1.5
$\%P_2O_5_{slag}$	1.44	1.66
$m_{P_2O_5_{slag}}$ (g)	0.0864	0.0996
$\%P_{final_{metal}}$	0.001	0.001
$m_{P_{final_{metal}}}$ (g)	0.00018	0.00018
$\Delta m_{P_{metal}}$ (g)	-0.0077	0.00007
$\Delta m_{Fe_{metal}}$ (g)	0.034	-0.00032
$\Delta m_{FeO_{slag}}$ (g)	-0.044	0.00042
$\Delta m_{P_2O_5_{slag}}$ (g)	0.035	-0.00033
$\%FeO_{final_{slag}}$	24.3	25.0066
$\%T.Fe_{final_{slag}}$	18.9	19.4
$(\%T.Fe_{final_{slag}})^{2.5}$	1552	1666
% Change on Lp	6.85	

## Impact of Oxygen from UHP Argon on Fe Oxidation

Another potential issue worth discussion regards to the fact that UHP Argon or Argon 6.0 may carry gaseous oxygen into the furnace. If the oxygen available from the gas reacts with liquid Fe, it can promote the formation of undesirable amounts of FeO. Therefore, it is necessary to estimate the potential impact that the gas might have on the two-phase metal-slag equilibrium.

As previously discussed in Section 5.2.2, an argon flow of 0.2 L/min was used for all experiments. The typical oxygen partial pressure for UHP Argon or Argon 6.0 is about  $10^{-5}$  to  $10^{-6}$  atmospheres respectively. Let us considered the amount of oxygen from the gas during the course of 11 hours, which is approximately the amount of time that a given experiment would be spend above the melting temperature of Fe, assuming a oxygen partial pressure of  $10^{-5}$  atmospheres. It follows that:

$$n_{O_2} = 0.2 \frac{L}{min} \times 660 \text{ min} \times 10^{-5} \text{ atm} \times \frac{1}{22.4} \frac{mol}{L \text{ atm}} \quad (5.7)$$

$$= 5.89 \times 10^{-5} \text{ mols} \quad (5.8)$$

$$n_{FeO} = 2 \times n_{O_2} \quad (5.9)$$

$$= 1.18 \times 10^{-4} \text{ mols} \quad (5.10)$$

$$m_{FeO} = n_{FeO} \times 55.845 \frac{g}{mol} \quad (5.11)$$

$$= 0.0066 \text{ g} \quad (5.12)$$

The maximum amount of FeO produced from oxygen available in the gas is about 0.007 grams. For a initial slag weighting 6 grams, this addition corresponds to 0.1wt.%. Therefore, the amount of oxygen from the gas is negligible and cannot impact the slag chemistry significantly. This reinforces that only a two-phase equilibrium is achieved between metal and slag.

### Impact of Furnace Cooling on $L_P$

As previously mentioned in Section 5.2.4, the furnace was cooled from 1600°C to 1300°C at a approximate rate of -35°C/min. This means that the samples would experience a short period of time at lower temperatures before solidification occurred. Since  $L_P$  increases with lower temperatures, it is important to make sure this period of time at lower temperatures did no influence the observed  $L_P$  for 1600°C.

Pure iron solidifies at 1538°C. At a cooling rate of -35°C/min, this temperature would be achieved in less than two minutes. Let us now investigate how much phosphorus could be transferred during this short period of time.

Using equation 3.28, it is possible to see that higher  $L_P$  would make the term  $\frac{W_m}{L_P W_s}$  closer to zero. Therefore, one can simplify and rearrange equation 3.28 to compute [%P] as a function of time:

$$[\%P] = [\%P]_0 \left( \exp \left( \frac{-A_T k_0 \rho_m}{W_m} t \right) - 1 \right) \quad (5.13)$$

Let us now assume two cooling scenarios, one where the samples experience the same cooling rate as the furnace, *i.e.* -35°C/min, and another where the samples cool at one third of the rate of the furnace. The basic difference between the scenarios is the time that the sample would spend at lower temperatures before solidification. In the first case, the sample would spend less than two minutes at lower temperatures while on the second case the time would be about six minutes. Tables 5.12 and 5.13 show the results assuming time averaged temperatures as shown in Figure 5.17. The calculations assumed  $A_T k_0 = 0.001 \text{ cm}^3/\text{s}$ ,  $W_m = 18 \text{ g}$ ,  $W_s = 6 \text{ g}$  and  $\rho_m = 6.98 \text{ g/cm}^3$ .

From the results above, it is seen that a couple extra ppms of phosphorus could be transferred to the slag. However, the uncertainties of chemical analysis are bigger

Table 5.12: Change in  $L_P$  due to furnace cooling at  $-35^\circ\text{C}/\text{min}$ .

Time (min)	Temp $^\circ\text{C}$	Avg Temp $^\circ\text{C}$	$L_P$ Equilib	[%P]	% Change	$L_P$ Calculated
0	1600		1083	0.0011		1083
1	1565	1583	1162	0.0011	2%	1109
2	1530	1548	1538	0.0010	5%	1135
3	1495	1513	2058	0.0010	7%	1162

Table 5.13: Change in  $L_P$  due to furnace cooling at  $-12^\circ\text{C}/\text{min}$ .

Time (min)	Temp $^\circ\text{C}$	Avg Temp $^\circ\text{C}$	$L_P$ Equilib	[%P]	% Change	$L_P$ Calculated
0	1600		1083	0.0011		1083
1	1588	1594	1061	0.0011	2%	1109
2	1577	1583	1162	0.0010	5%	1135
3	1565	1571	1274	0.0010	7%	1162
4	1553	1559	1399	0.0010	9%	1189
5	1542	1548	1538	0.0010	11%	1217
6	1530	1536	1693	0.0010	13%	1246

than the transfer that could occur in both scenarios. Thus, this is not thought to be a significant effect.

### 5.4.3 MgO Saturation

As previously mentioned in Section 5.3, the software package FactSage was used to determine the initial slag composition and the MgO content was that of the saturation line for the given CaO-SiO<sub>2</sub>-FeO slag system. However, all of the analyzed slags showed a higher final MgO content in the slag. The average MgO pickup is +1.96 wt.%. The average initial and final MgO contents are 3.6 wt.% and 5.6 wt.% respectively. Such variation corresponds to an increase of 55% in the final MgO content in the slag.

One could raise the question whether the higher MgO contents correspond to

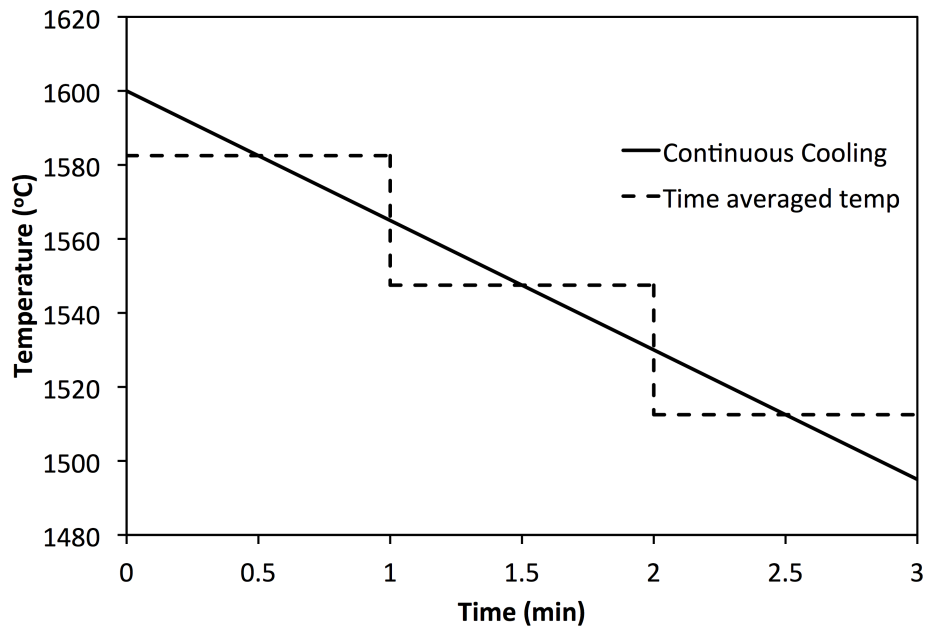


Figure 5.17: Example of time averaged temperature used for calculation of changes in  $L_P$  due to furnace cooling.

traces of the magnesia crucible used. While this is a valid point, all slag samples were carefully and manually ground using 120 grade sand paper until any traces of visually detectable crucible were removed. This was easily achieved due to the color difference between the crucible and the bulk slag. From Figure 5.8 one can observe that the transition from the crucible to the slag is well defined and there is a transition from white (crucible) to brownish (crucible infiltrated by slag) to black (bulk slag).

It is possible that FactSage underestimates the MgO saturation by a few wt.%. This seems to be the case as MgO pickup has occurred for all the experiments. Figure 5.18 shows the MgO solubility predicted by FactSage and the measured solubility based on the chemical analysis results as a function of the binary basicity.

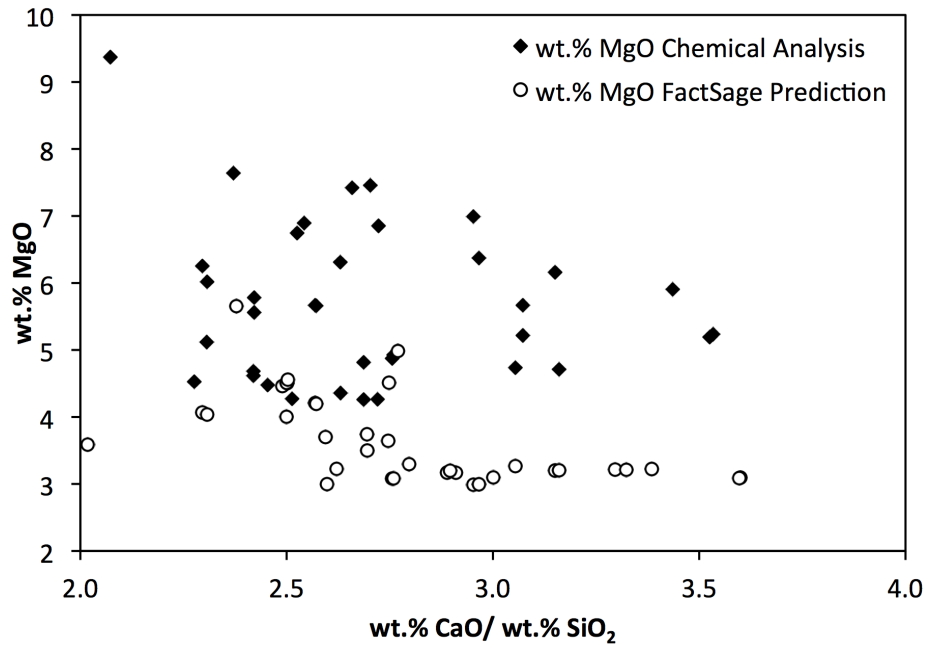


Figure 5.18: MgO solubility as a function of binary basicity.

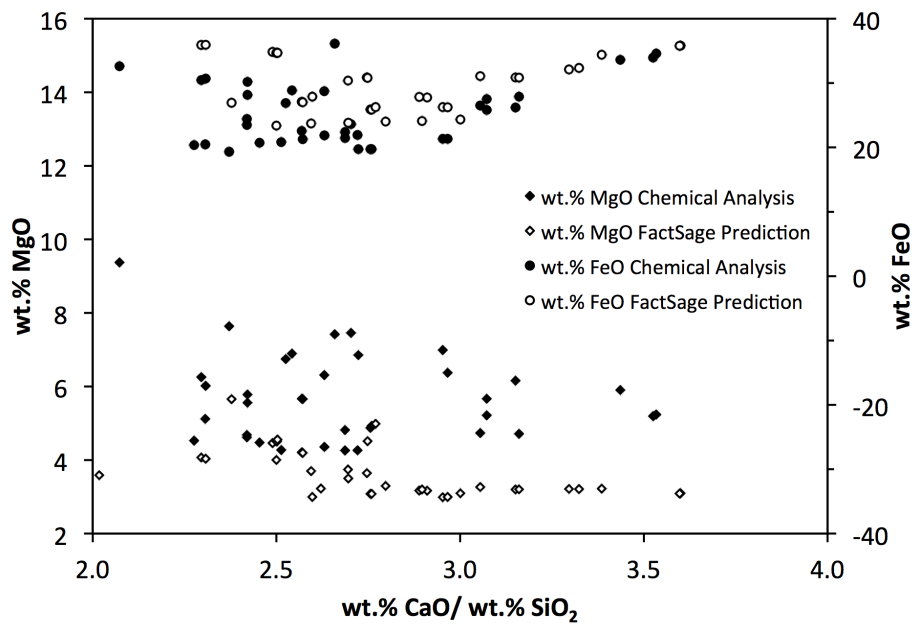


Figure 5.19: MgO solubility as a function of binary basicity and FeO content.



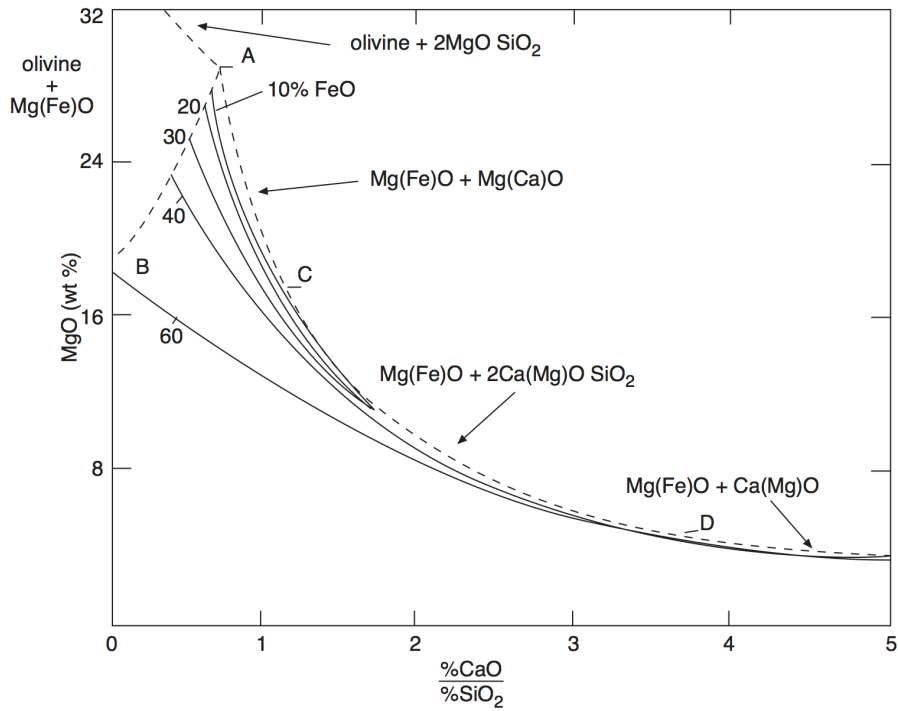


Figure 5.20: MgO saturation as as magnesiowustite as a function of binary basicity and FeO content at 1600°C. Reproduced from [1].

The solubility of MgO in liquid slag is not only a function of basicity, but also of FeO. As seen in Figure 5.19, the FeO content for the present work is in the range of 20 to 40 wt.% FeO. The classical work done by Tromel et al. [58] in 1969 agrees better with the MgO solubility observed in the present work than the ones predicted by FactSage. Figure 5.20 (reproduced from [1]) shows the results from Tromel et al. for MgO saturation, as magnesio-wustite, for FeO contents from 10 to 60 wt.% as a function of basicity. The effect of FeO on the MgO saturation is larger at lower basicities, but the solid curves converge quickly for basicities higher than 2.0. The MgO saturations for basicities of 2, 3 and 4, according to Tromel et al. [58], are approximately 9, 6 and 4 wt.%MgO respectively. This is in reasonable agreement with the observations of the present work but differ considerably from the FactSage

predictions.

In summary, the observed MgO solubility and saturation differ considerably from the predictions by FactSage but are in reasonable agreement with the work done by Tromel et al. [58]. It is not in the scope of this project to propose modifications to the FactSage model.

#### 5.4.4 Development of a New Correlation

The discussion so far has involved four main data sets: Suito’s data [10, 11], Basu’s data [12, 13], Tayeb’s data [2] and the present work. The differences in the experimental approach adopted by Suito and Basu have already been discussed in the beginning of Section 5.4.2, particularly in regards to the equilibration time used in each study and the possibility that thermodynamic equilibrium may not have been achieved. Another possible issue would be the presence of solid phases in the slag which would cause issues by “masking” the liquid slag composition, which will be further discussed in Chapter 6. Therefore, it is necessary to estimate the amount of solid phases present in the experiments conducted by previous authors. A FactSage macro was used to automate the slag equilibrium calculations to retrieve the equilibrium liquid slag and the solid oxide phases formed. The possible solid phases considered were MgO solid solutions, CaO solid solutions and  $2\text{CaO}\cdot\text{SiO}_2$ .

From Figure 5.21, it can be seen that Suito’s slags were mostly liquid, with a liquid fraction varying between 0.8 to 1.0. On the other hand, Basu’s data is predicted to have a large amount solid phases, with liquid fractions ranging from 0.3 to 0.92 as shown in Figure 5.22. The presence of a large quantity of solid phases makes it very difficult to evaluate the composition of the remaining liquid slag, as will be discussed in the next chapter when looking at plant data.

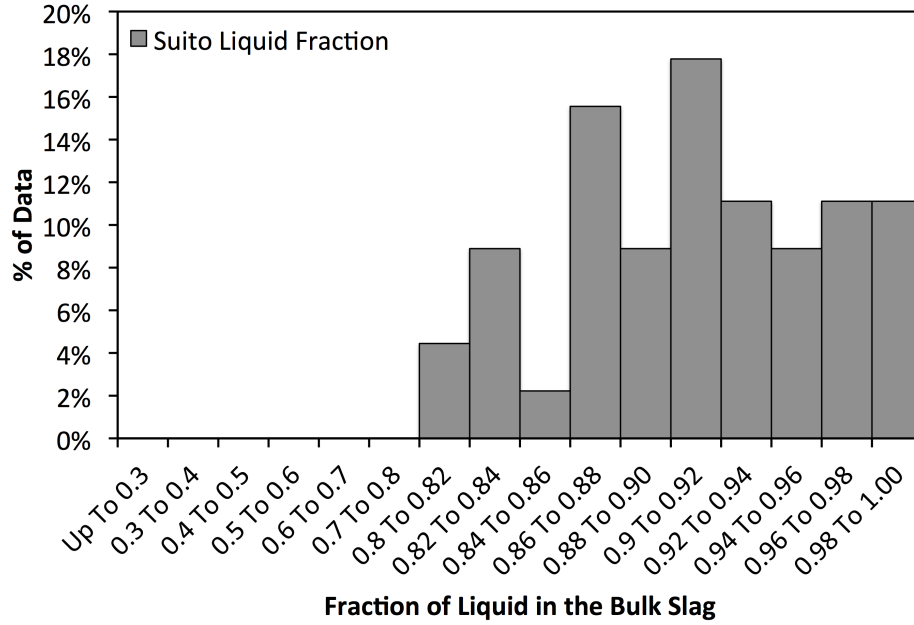


Figure 5.21: Liquid fraction of slag predicted by FactSage for Suito's data.

Based on the aforementioned points, the author and co-workers have decided to develop a new correlation combining only the present work data, Tayeb's and Suito's data.

The steps for developing a new correlation are described below:

1. Use Ide's MgO coefficient and fix its value as  $0.072 \times 0.15 = 0.0108$  as originally reported by Ide et al. [27].
2. Evaluate  $\log K_P - 0.0108(\%MgO)$  as a function of  $wt.\%CaO$ ,  $wt.\%SiO_2$  and  $wt.\%P_2O_5$  utilizing Tayeb's, Assis' and Suito's data at 1600°C.

$$\log K_P - 0.0108(\%MgO) = 0.073(\%CaO) + 0.058(\%P_2O_5) + 0.008(\%SiO_2) - 4.226 \quad (5.14)$$

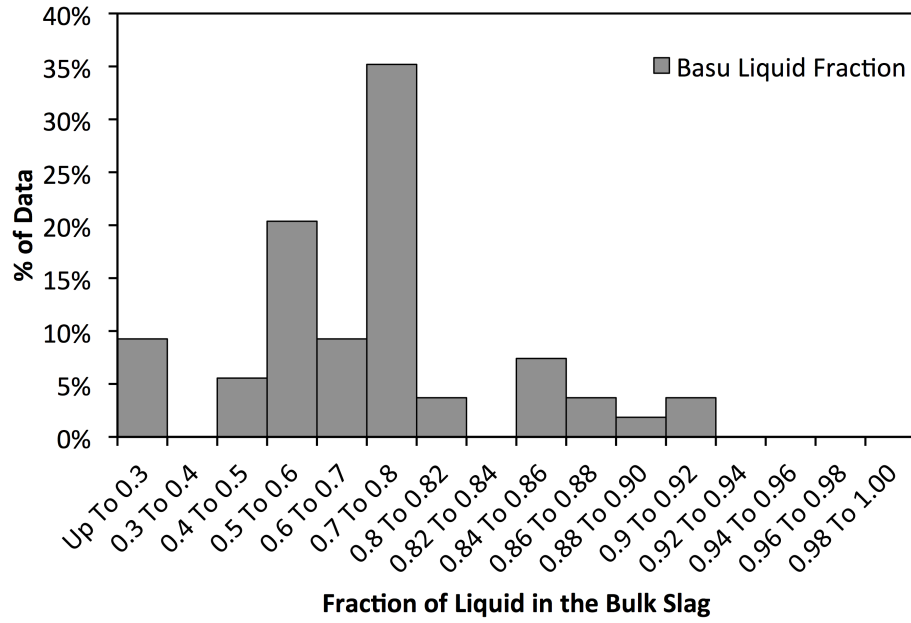


Figure 5.22: Liquid fraction of slag predicted by FactSage for Basu's data.

3. Adjust the original intercept of Suito's equation to give -4.226 at 1600°C.

$$\frac{11570}{1600 + 273.15} + b = -4.226 \quad (5.15)$$

$$b = -4.226 - 6.177 \quad (5.16)$$

$$b = -10.403 \quad (5.17)$$

Statistical correlations are only valid within the range in which they were originally evaluated. This range was previously shown in Table 5.9. The final correlation is then:

$$\log \frac{(\%P)}{[\%P](T.Fe)^{\frac{5}{2}}} = 0.073 \left[ (\%CaO) + 0.148(\%MgO) + 0.8(\%P_2O_5) + 0.113(\%SiO_2) \right] + \frac{11570}{T} - 10.403 \quad (5.18)$$

Equation 5.18 has a few interesting features that are worth discussing. First, the CaO coefficient is in very good agreement with the original coefficient reported by Suito. Second, the P<sub>2</sub>O<sub>5</sub> coefficient is higher than the original coefficient of 0.6 proposed by Suito et al. [11]. It is important to remember that this coefficient was evaluated over a range of P<sub>2</sub>O<sub>5</sub> contents, *i.e.* from 0.5 to 5.5 wt.%. For steelmaking applications however, it is uncommon to have P<sub>2</sub>O<sub>5</sub> contents above 3 wt.%, so this higher coefficient should not be a problem as long as the phosphorus contents in the slag are within the aforementioned range. Second, SiO<sub>2</sub> has a small but positive coefficient. A positive SiO<sub>2</sub> coefficient, does not mean it aids dephosphorization, in fact, the coefficient is significantly smaller than the one for CaO by an order of magnitude. Thus, lower  $L_P$ 's are predicted for acid slags. This is exemplified in Table 5.14 where  $L_P$  is predicted to decrease by a factor of 1.9 for a slag containing 19 and 24 wt% SiO<sub>2</sub> respectively. Lastly, the constant changed from -10.520 to -10.403 which represents a difference of 25% on the phosphorus partition coefficient once the log term is accounted for in Equation 5.18.

Table 5.14: Change in  $L_P$  with 5 wt.% increase in SiO<sub>2</sub> content.

wt.% CaO	wt.% SiO <sub>2</sub>	wt.% P <sub>2</sub> O <sub>5</sub>	wt.% MgO	wt.% FeO	Total	Equilib $L_P$
51	19	3	7	20	100	801
48	24	3	6	19	100	425

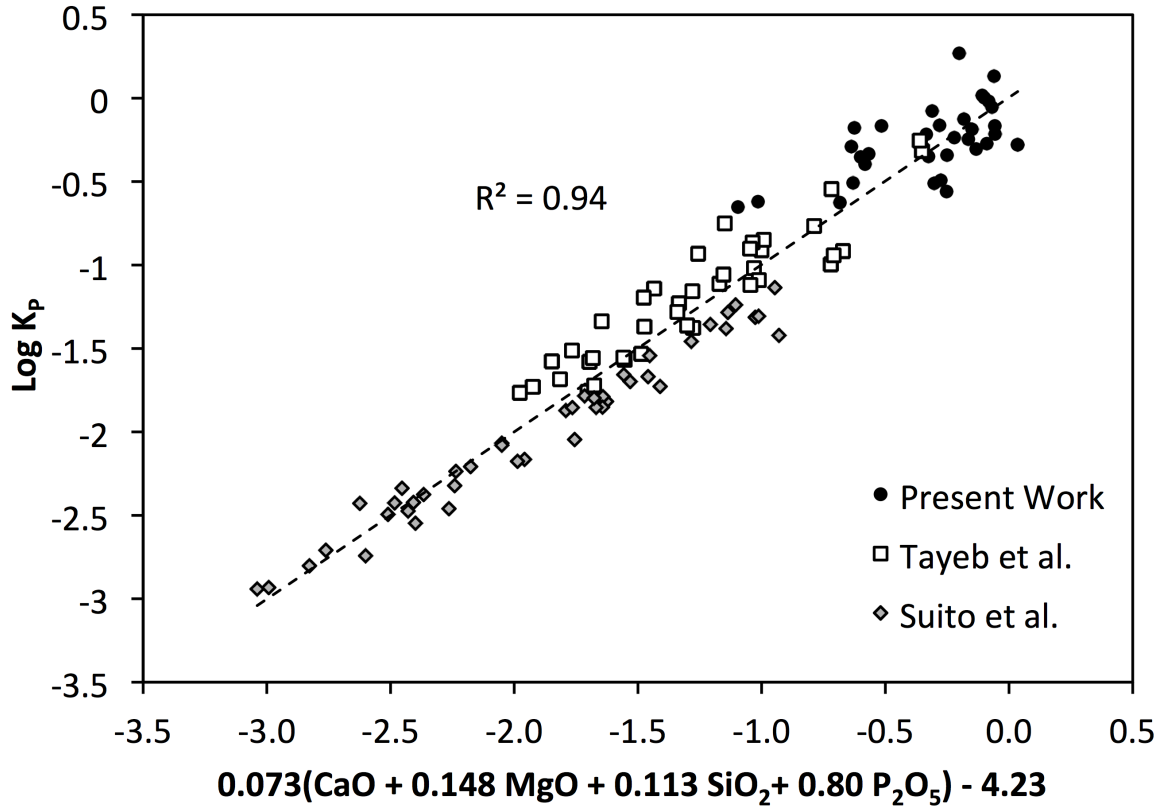


Figure 5.23: Comparison between present work, Tayeb's [2] and Suito's [10,11] using the new correlation from Equation 5.18.

Figure 5.23 shows the plot of the new correlation. The agreement with Assis' and Tayeb's data is very good throughout the whole range of EAF and BOF type slags. Suito's data also fits the equation quite well. The calculated  $R^2$  is 0.94. The diagonal plot of measured  $L_P$  vs. predicted  $L_P$  (Figure 5.24) shows again very good agreement and the new correlation predicts most of the data quite well. The prediction of the present work data is within a factor of about 2. While this may seem like a big discrepancy, it must be remembered that the equilibrium phosphorus content in the metal for the present work is very low and the uncertainty can be significantly large as discussed previously.

Equation 5.18 represents the final result within the scope of this chapter. The

author firmly believes that it represents an improvement over previous correlations. Its applicability is restricted to the range of compositions studied and it was developed with focus on EAF- and BOF-type slags. This final correlation is used on the next chapters whenever it is necessary to predict the equilibrium phosphorus partition.

In summary, this chapter provided a thorough discussion on phosphorus equilibrium between liquid iron and BOF type slags. It was concluded that 10 hours of holding time is adequate to ensure thermodynamic equilibrium. The experimental data from the present work showed phosphorus partitions considerably higher than those from previous studies. The impact of FeO being a reactant as well as the possible oxidation of Fe from the argon gas were studied and found to have little impact on  $L_P$ . The author showed that the MgO saturation predicted by FactSage appears to be lower than what was found experimentally. Finally, a new correlation was developed using the present data, Tayeb et al. [2] and Ide's data. This correlation was presented in Equation 5.18. The author believes this is a suitable correlation for steelmaking slags as long as the studied data falls within the range of composition of which the correlation was evaluated.

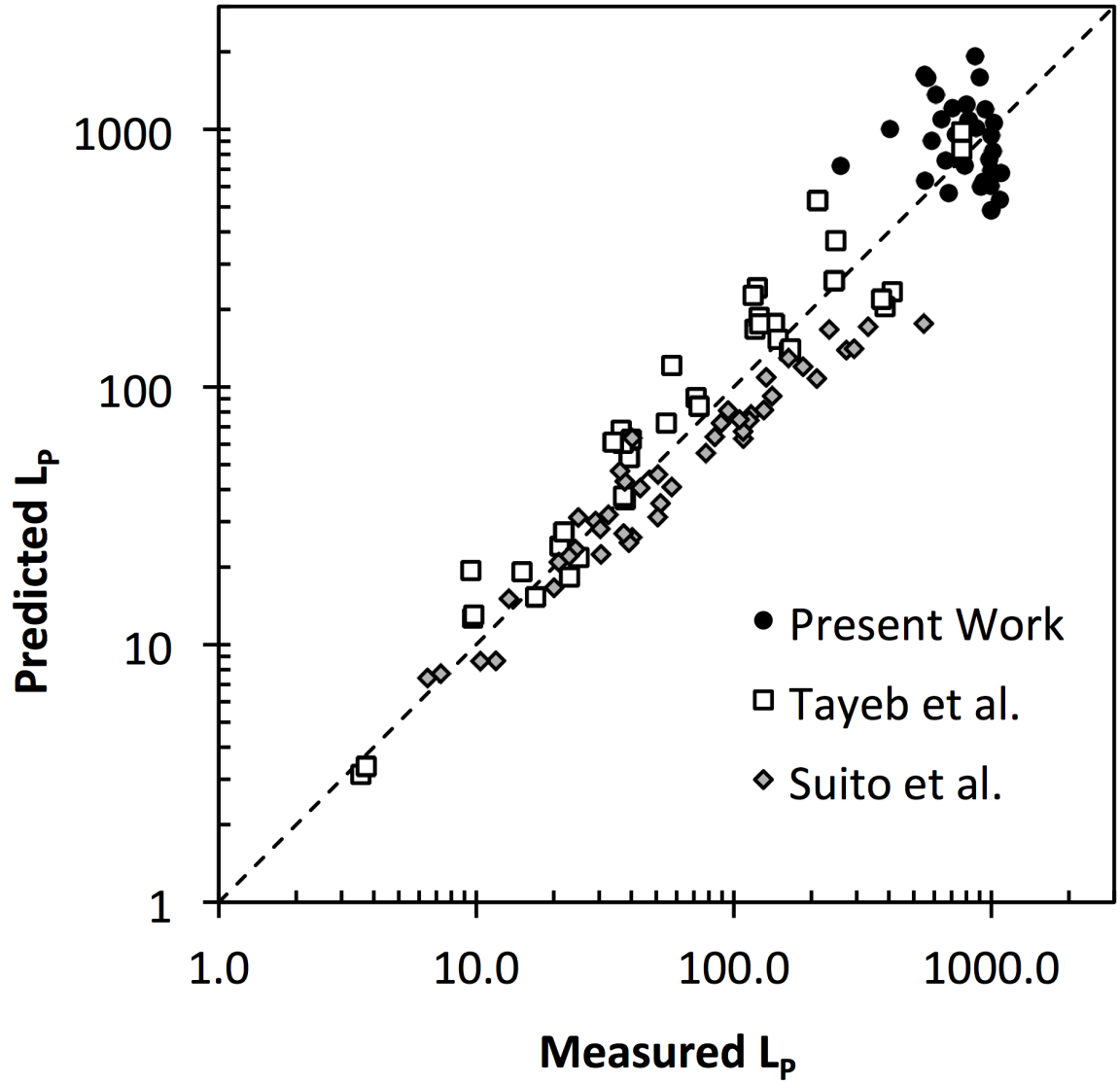


Figure 5.24: Measured  $L_P$  *vs.* Predicted  $L_P$  for present work, Tayeb's [2] and Suito's [10,11] data using the new correlation from Equation 5.18.



# Chapter 6

## Plant Data Analysis

### 6.1 Introduction

As previously discussed in Section 3.1, an extensive amount of work has been done on the topic of phosphorus equilibrium partitioning between liquid metal and slag. However, comparison between large amounts of plant data and laboratory equilibrium data still remains relatively small. One of the goals of the present work is to evaluate how different designs of industrial furnaces perform from the point of view of phosphorus removal by comparing how close these furnaces can get to the predicted equilibrium.

### 6.2 Technical Approach

Data from three different furnaces were compared. The AOD (Argon Oxygen Decarburization), which is a highly stirred reactor, usually used in the production of stainless steels, a regular top-blown BOF and a Q-BOP or OBM.

The data sets from each reactor consisted of the steel and slag composition just

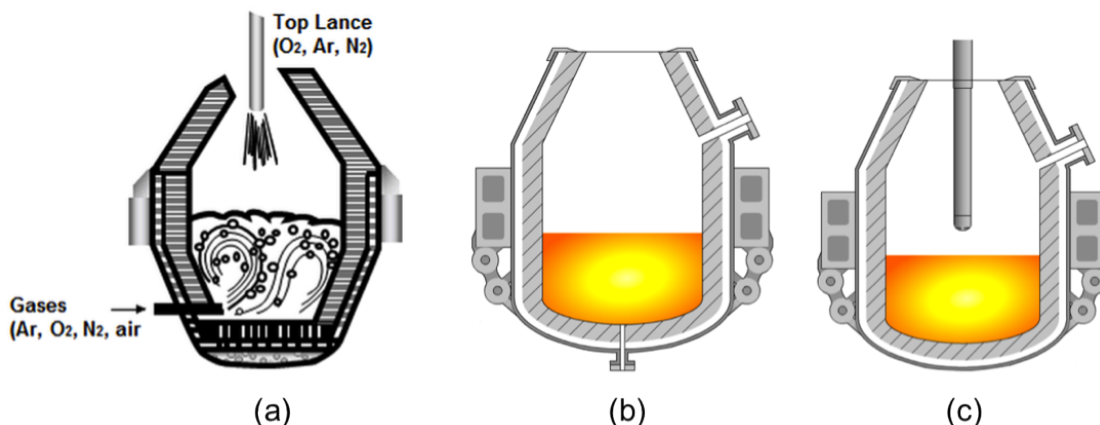


Figure 6.1: Schematics diagram of AOD [15](a), Q-BOP or OBM [16](b) and top-blown BOF [17](c)

before tapping, as well as the tapping temperature of each heat.

The slag compositions were normalized to the  $\text{CaO-MnO-SiO}_2\text{-MgO-FeO}_t\text{-P}_2\text{O}_5$  system and the sets of data were plotted using the correlation given by Equation 5.1. The other components, such as  $\text{Al}_2\text{O}_3$ ,  $\text{MnO}$  and  $\text{TiO}_2$  were normally less than 5% in total.

For the AOD, the author had access to over 230 heats. For the three BOFs, the amount of data was in the order of thousands. Table 6.1 shows the exact number of heats for each of the furnaces as well as the average, maximum and minimum turndown temperature.

Since the amount of data for the Q-BOP, BOF 1 and BOF 2 is much larger than that of the AOD, approximately 10% of the BOF heats were randomly selected and used for the present work.

Because the chemical analysis data was that of the bulk slag, it is probable that undissolved oxides such as solid solutions of  $\text{CaO}$  and  $\text{MgO}$  were present during the operation of each vessel. This would “mask” the actual liquid slag composition making it either more or less demanding with respect to dephosphorization. Because

Table 6.1: Average, Minimum and Maximum Turndown Temperatures for AOD, Q-BOP or OBM, BOF 1 and BOF 2.

	Number of Heats	Average Turn-down Temperature (°C)	Minimum Turn-down Temperature (°C)	Maximum Turn-down Temperature (°C)
AOD	233	1600	-	-
Q-BOP	6328	1647	1569	1715
BOF 1	6574	1626	1559	1691
BOF 2	2428	1655	1584	1709

the author had no access to the physical samples, FactSage was used to predict the amount of solid phases in equilibrium with the liquid slag which provided a better estimate of the actual liquid slag composition. Assis et al. [59] recently emphasized the importance of correcting the bulk slag analysis excluding undissolved oxides.

A FactSage macro was used to automate the slag equilibrium calculations to retrieve the equilibrium liquid slag and the solid oxide phases formed. The possible solid phases considered were MgO solid solutions, CaO solid solutions and  $2\text{CaO}\cdot\text{SiO}_2$ . As a first approximation, it was assumed that all phosphorus from the bulk slag would be dissolved only in the liquid portion of the slag and that there was no solubility of phosphorus in the considered solid phases. This assumption is further discussed in the next sections.

## 6.3 Results

A total of 1788 heats were run on FactSage to extract the equilibrium liquid slag composition. The most common solid phase predicted was  $\text{MeO}_A$ , which corresponds to a monoxide phase for CaO and MgO solid solutions. A total of 97.6% of the industrial data had monoxides predicted by FactSage as shown in Table 6.2. Dicalcium

silicate was predicted for 23.4% of the heats as shown in Table 6.3. All the data where  $2\text{CaO}.\text{SiO}_2$  was predicted also had monoxides according to FactSage. Also, all the data containing CaO solid solution also contained MgO solid solution. The distribution of the fraction of monoxides (MgO and CaO) and  $2\text{CaO}.\text{SiO}_2$  with respect to the bulk slags is shown in the histograms in Figures 6.2, 6.3 and 6.4 respectively. The aforementioned figures correspond to the distribution of the subsets of heats containing MeO, *i.e.* 1745 heats, and  $2\text{CaO}.\text{SiO}_2$ , *i.e.* 418 heats, respectively.

Table 6.2: Number of heats for each reactor where CaO and MgO solid solutions (S.S.) were predicted as solid phases by FactSage.

	MgO S.S.	CaO S.S	Total MeO-A
Reactor	Number of Heats	Number of Heats	Number of Heats
AOD	205	0	205
Q-BOP	634	628	634
BOF1	663	112	663
BOF2	243	234	243
Total			1745
% of Total Data			97.6%

Table 6.3: Number of heats for each reactor where  $2\text{CaO}.\text{SiO}_2$  was predicted as solid phase by FactSage.

Reactor	Number of Heats
AOD	1
Q-BOP	316
BOF1	101
Total	418
% of Total Data	23.4%

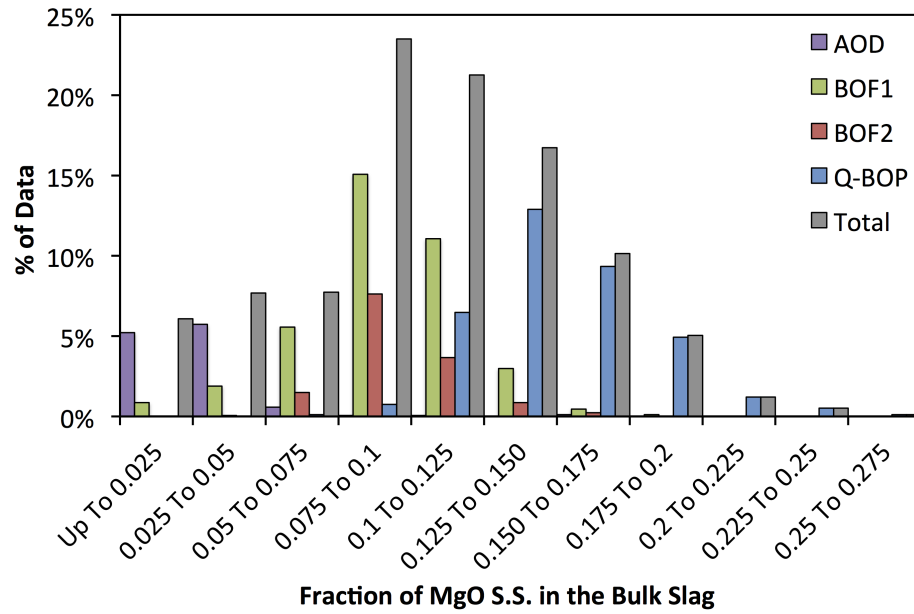


Figure 6.2: Histogram of the fraction of total monoxide present in the bulk slag in the form of MgO solid solution.

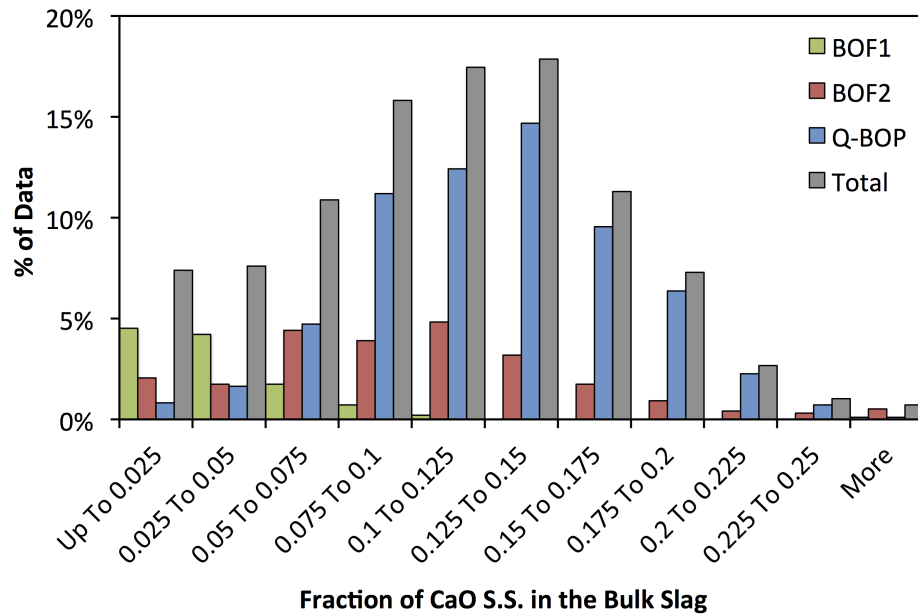


Figure 6.3: Histogram of the fraction of total monoxides present in the bulk slag in the form of CaO solid solution.

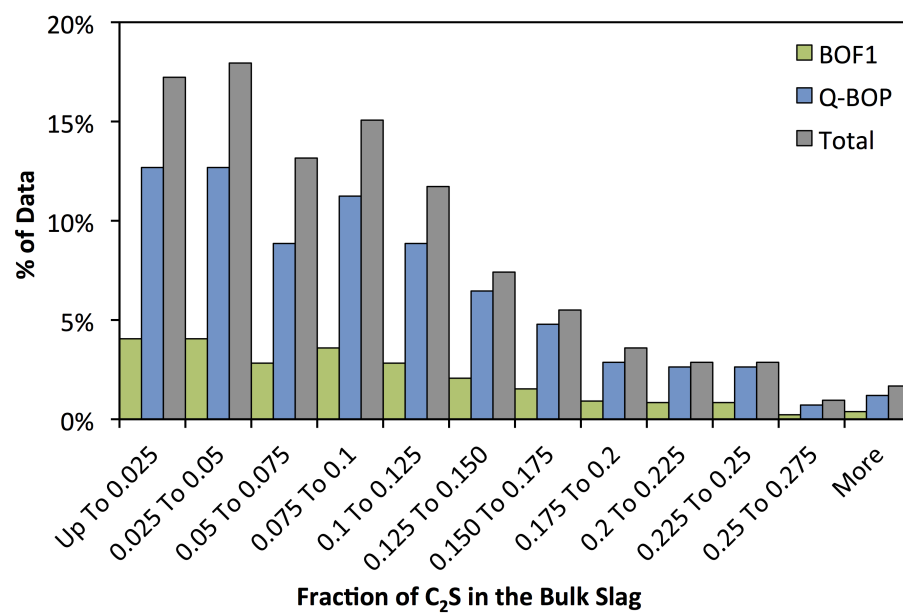


Figure 6.4: Histogram of the fraction of dicalcium silicate present in the bulk slag.

Table 6.4 shows the average chemical composition for the slag and steel for the each of the furnaces. The AOD has the lowest average binary basicity at around 1.5 and the highest  $\text{FeO}_t$  content at 37.5 wt.%, it also has the lowest phosphorus content in the steel and in the slag. The Q-BOP or OBM presents the highest phosphorus partition,  $L_p$ , at 182 but it also has the highest  $\text{P}_2\text{O}_5$  content in the bulk slag. The BOF 1 has the second lowest basicity but the second best final phosphorus content in the steel. BOF 2 has the highest average basicity at 3.9 and also the highest phosphorus content in the steel.

Table 6.4: Average chemical composition data for the steel and the slag for AOD, Q-BOP, BOF 1 and BOF 2.

Reactor	$\text{CaO}/\text{SiO}_2$	%MgO	%FeOt	%MnO	%P <sub>2</sub> O <sub>5</sub>	[%P]	$L_p$
AOD	1.54	9.3	37.53	2.02	0.19	0.0019	103.89
Q-BOP	3.26	13.71	17.87	4.23	1.34	0.0073	182.19
BOF 1	2.43	9.21	26.78	5.35	0.7	0.0071	97.98
BOF 2	3.9	9.75	26.26	4.83	1.19	0.0084	141.15

Figures 6.5 and 6.6 used the bulk slag composition to present the predicted equilibrium phosphorus partition,  $L_p$ , calculated using Equation 5.18, against the actual phosphorus partition for each of the furnaces. This plot is useful because it removes the log effect on the data so we can study the true scatter for each reactor. Additionally, contour plots are an easy way to visualize the density of the data and possible multiple operating regimes a single reactor might have. In these plots, the thickness of the lines is proportional to the density of the data. The dashed black line represents the diagonal of the plot, meaning that  $L_p$  predicted is equal to  $L_p$  actual. The combination of all plots from Figures 6.5 and 6.6 is shown in Figure 6.7.

All the contour plots were generated using the Microsoft Excel add-in “Contour Plot” by Office Expander. In order to generate such plots, the data for each reactor

was divided in a 26 by 26 grid or matrix, resulting in a total of 676 “pixels”. The size of the “pixels” was adjusted in order to fit the individual sets of data in the matrix. Typical “pixel” sizes varied between 8x8 to 40x40. The amount of data in each “pixel” was counted to produce a “height” on the z-axis which correspond to the amount of heats that fall into each “pixel”. The pixel with the highest peak height was then used to normalize the data so that the relative frequencies for each reactor would be between 0 to 1. Finally, contours corresponding to relative frequencies of 0.2, 0.4, 0.6 and 0.8 were used for all sets of data. These values were chosen to eliminate outliers in the data which would typically appear with relative densities of 0.1 and below.

As previously mentioned in Section 6.2, each individual heat was corrected for possible solid phases in equilibrium with the liquid slag. Figures 6.8 and 6.9 show the results taking into account only the liquid portion of the bulk slag as predicted by FactSage. The combination of all contour and scatter plots for the corrected slags is shown in Figure 6.10.



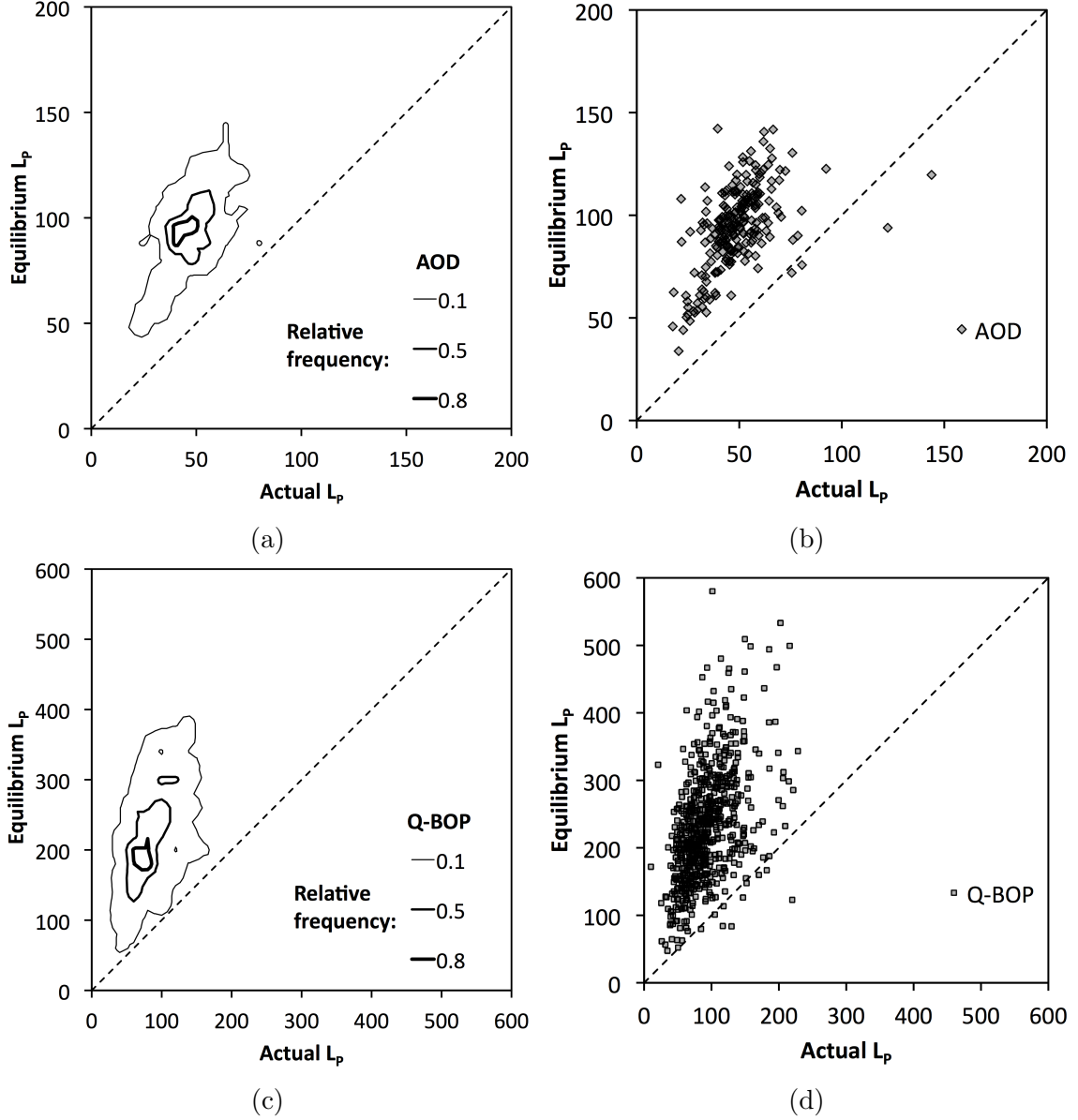


Figure 6.5: Contour and scatter plots for Actual  $L_p$  vs. Equilibrium  $L_p$  for AOD (6.5a and 6.5b) and Q-BOP (6.5c and 6.5d) for bulk slag compositions. Thickness of the contour lines are proportional to relative density of data.

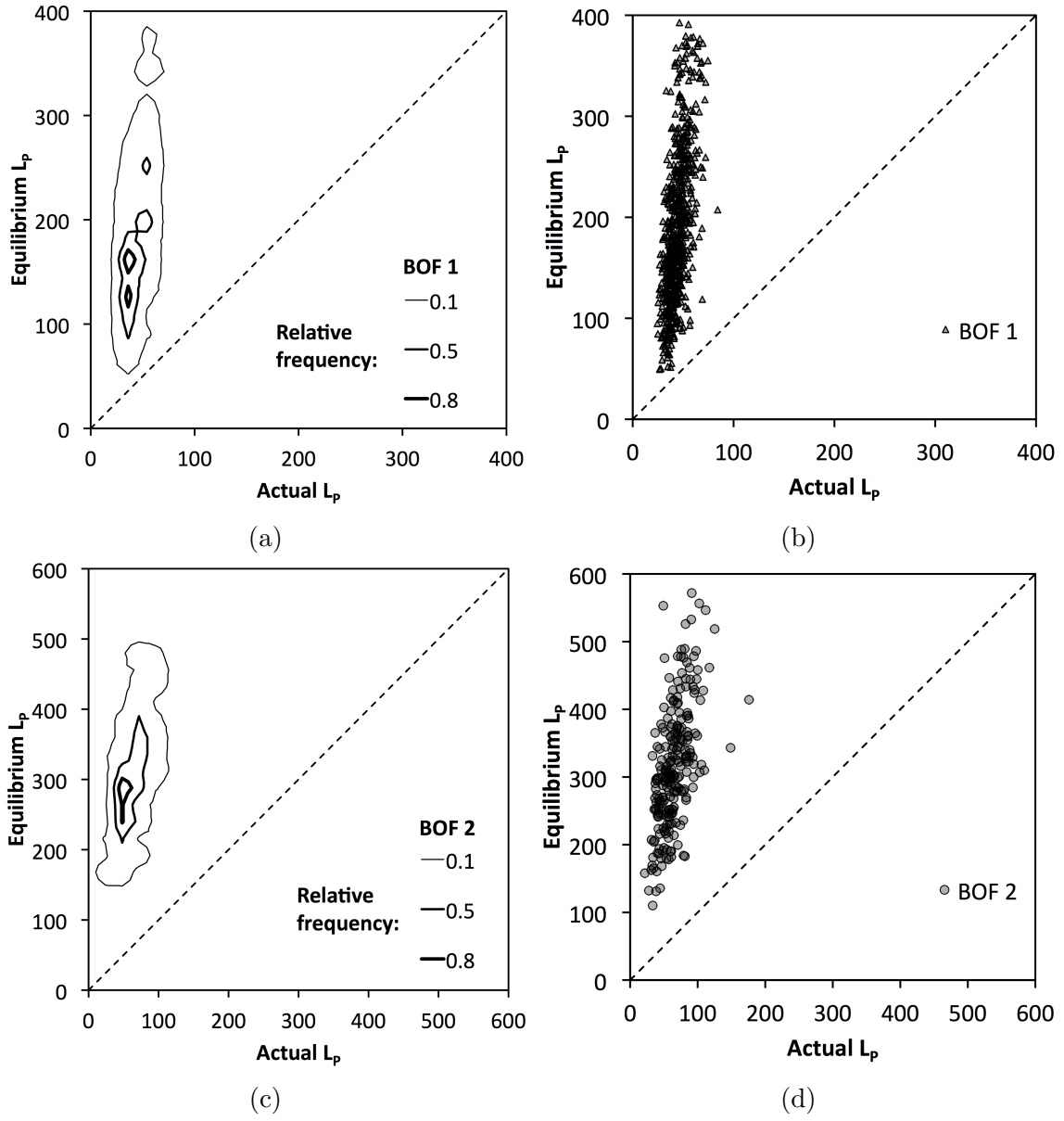
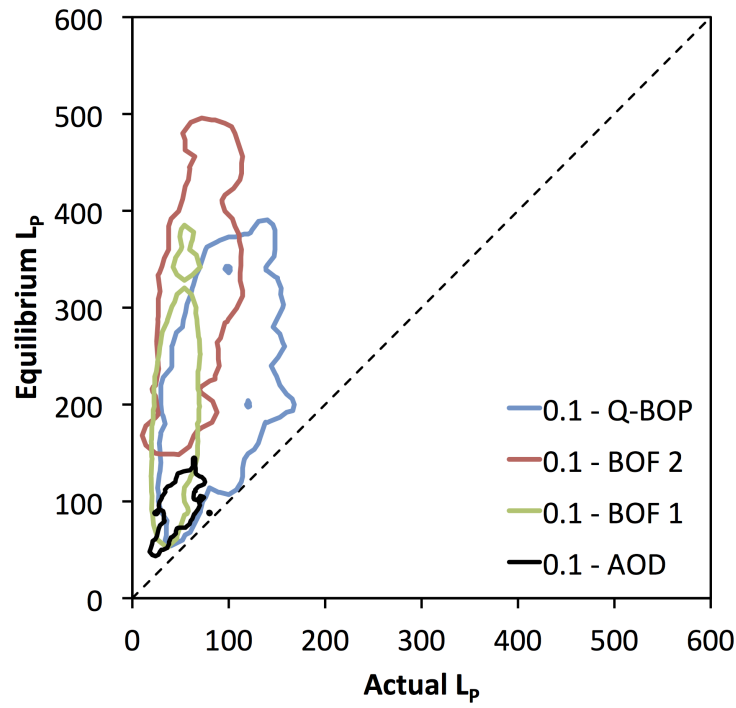
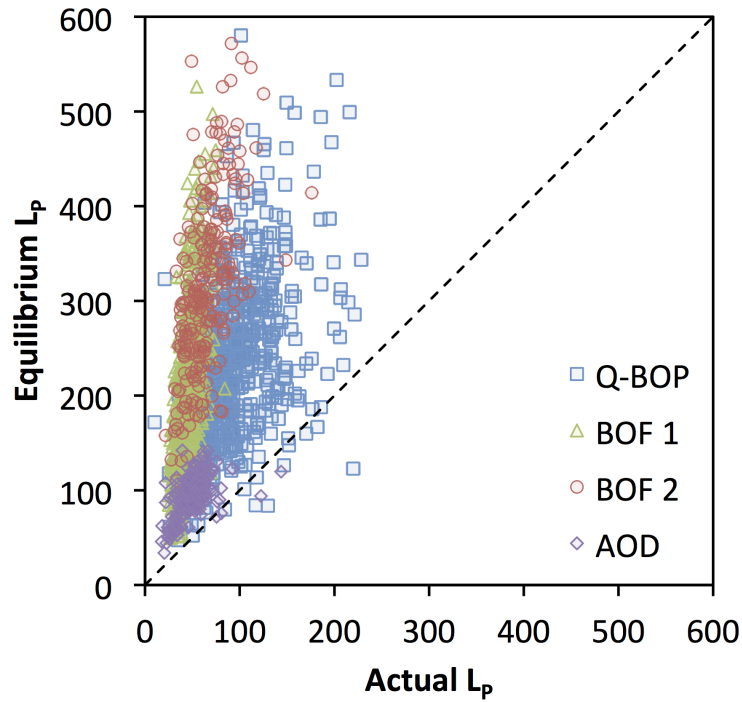


Figure 6.6: Contour and scatter plots for Actual  $L_p$  vs. Equilibrium  $L_p$  for BOF 1 (6.6a and 6.6b) and BOF 2 (6.6c and 6.6d) for bulk slag compositions. Thickness of the contour lines are proportional to relative density of data.



(a)



(b)

Figure 6.7: Contour and scatter plots for Actual  $L_p$  vs. Equilibrium  $L_p$  for all furnaces studied using bulk slag compositions.

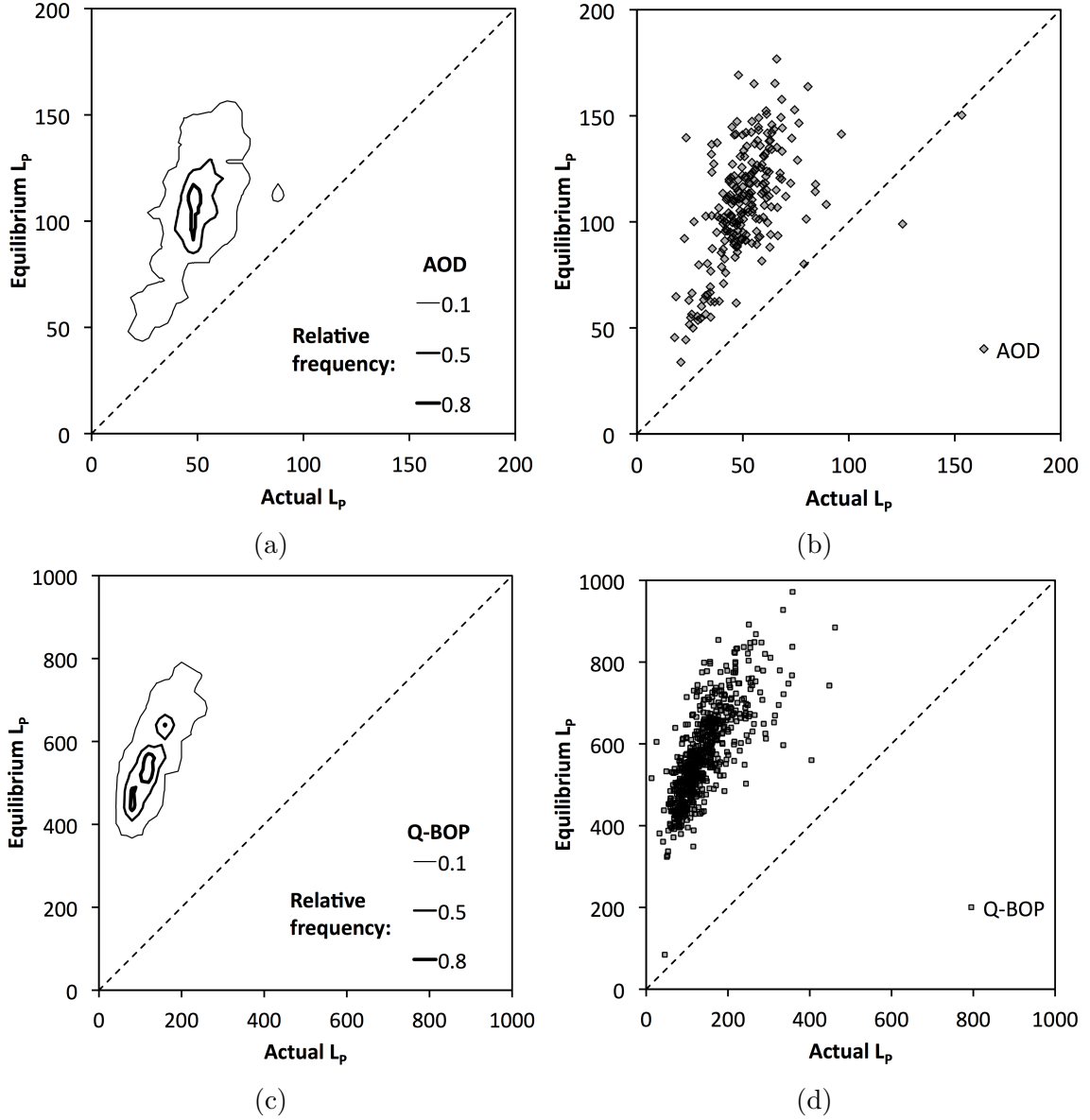


Figure 6.8: Contour plots for Actual  $L_p$  vs. Equilibrium  $L_p$  for AOD (6.8a and 6.8b) and Q-BOP (6.8c and 6.8d) for liquid slag compositions after FactSage correction. Thickness of the contour lines are proportional to relative density of data.

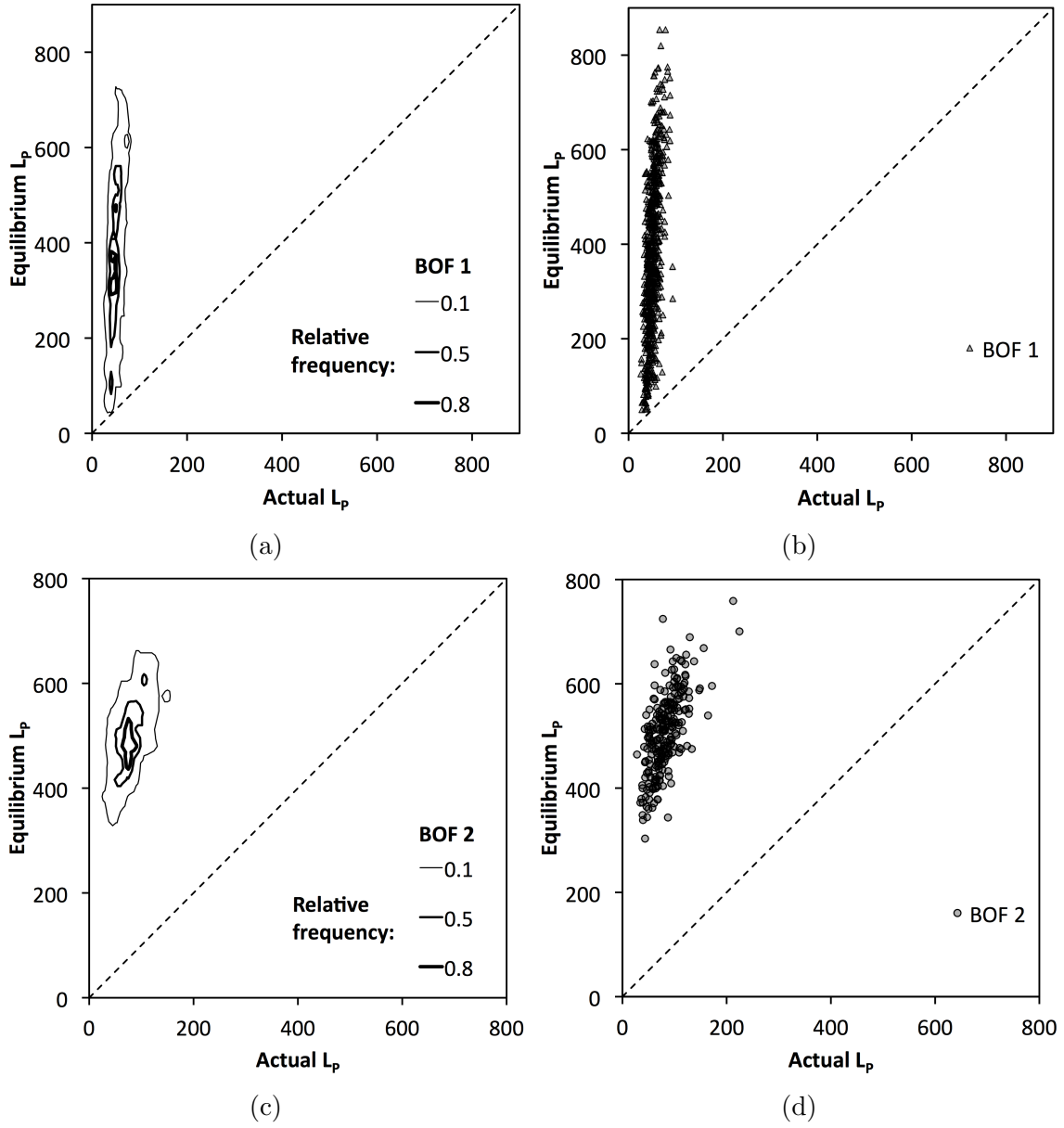
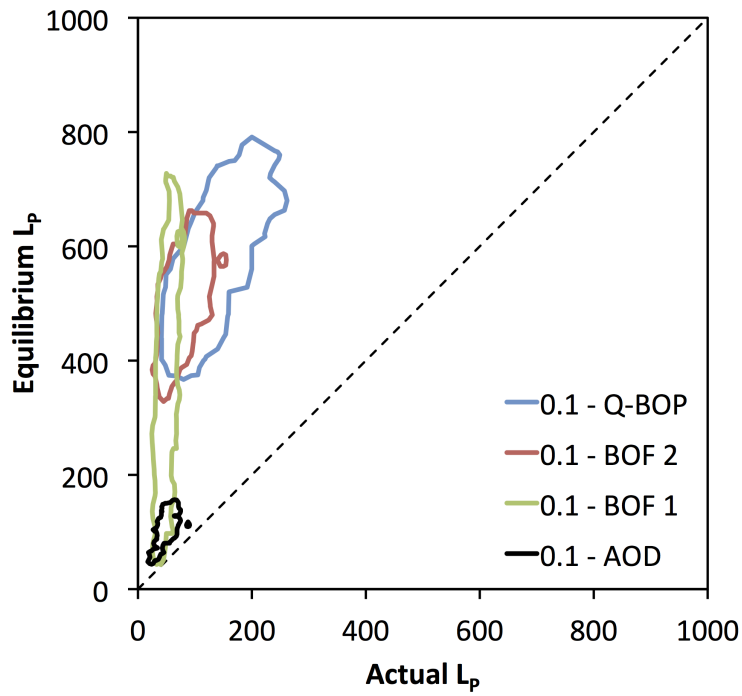
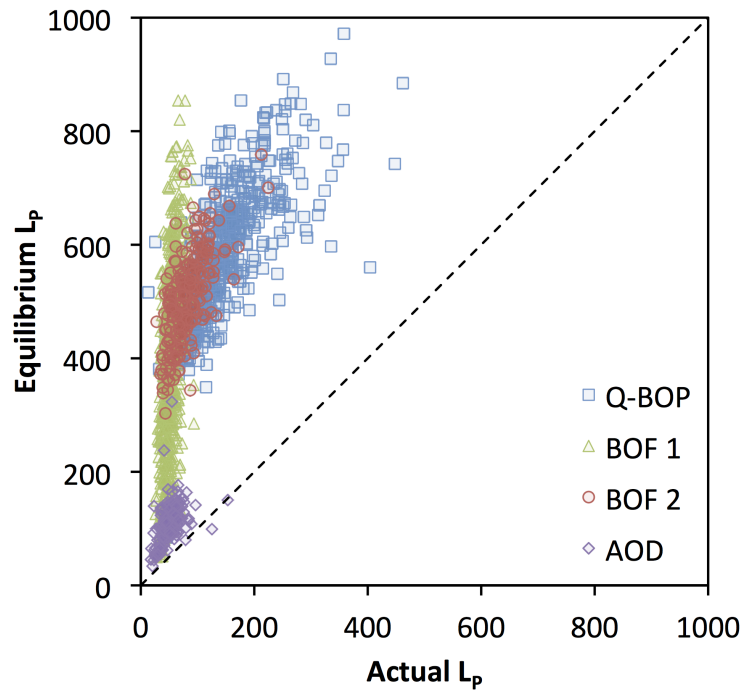


Figure 6.9: Contour plots for Actual  $L_p$  vs. Equilibrium  $L_p$  for BOF 1 (6.9a and 6.9b) and BOF 2 (6.9c and 6.9d) for liquid slag compositions after FactSage correction. Thickness of the contour lines are proportional to relative density of data.



(a)



(b)

Figure 6.10: Contour and scatter plots for Actual  $L_p$  vs. Equilibrium  $L_p$  for all furnaces studied after FactSage correction.

It is also interesting to look at the fraction of liquid slag predicted by FactSage in order to understand its effects on the kinetics of dephosphorization in real industrial operations. Figure 6.11 shows the normalized superimposed histograms for all four furnaces and the percentage of slags that fall into each liquid fraction band of the histograms.

## 6.4 Discussion

The vast majority of the data studied was predicted to have MgO S.S as a coexisting phase with the liquid slag. From Figure 6.2 it can be seen that the AOD operates with minimum amount of MgO S.S.. BOF 1 and BOF 2 operate in the same “mode” with the fraction of MgO S.S. varying roughly between 0.05 to 0.015. The Q-BOP or OBM operates in a higher “mode” with solid fractions in the range of 0.1 to 0.25.

Regarding the saturation with CaO S.S., all slags where CaO saturation was predicted were also saturated with MgO. Therefore, these slags were actually double saturated. The AOD was the only reactor that had no excess CaO. BOF 1 operates within the lower “mode” followed by BOF 2 and the Q-BOP as seen in Figure 6.3.

In the case of the formation of dicalcium silicate, the AOD and BOF 2 were not predicted to have dicalcium silicate present, except for one heat of the AOD. Only BOF 1 and the Q-BOP had a quantifiable distribution of  $C_2S$  present in the bulk slag, with the Q-BOP having significantly more  $C_2S$  than BOF 1.

Overall, the Q-BOP is by far the most saturated reactor, presenting significant amounts of all three solid phases considered. On the other hand, the AOD is the least saturated reactor with slags containing only minor amounts of MgO.

The amount of solids present in the bulk slag has a directed implication on the rate of mass transfer for a given amount of stirring. The more solids present in the

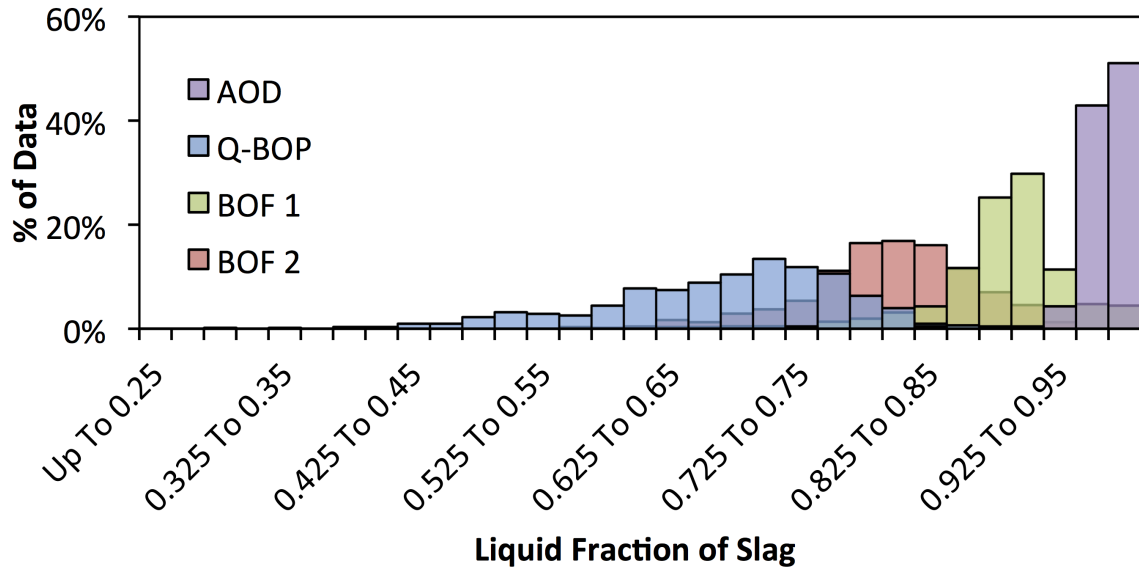


Figure 6.11: Superimposed Histograms of liquid slag fraction for each of the furnaces.

slag, the higher the bulk viscosity thus, the lower the mass transfer rate.

Looking at the bulk slags before the FactSage correction (Figure 6.7) the AOD and the Q-BOP were the furnaces operating closest to equilibrium with the highest density peak located, in terms of (x, y) coordinates, at around (40, 90) and (60, 180) respectively. Next, BOF 1 operated in a vertical regime with most of its data farther from equilibrium than the AOD and the Q-BOP with its highest peaks located at around (30, 120) and (40, 170). Lastly, BOF 2 operated also quite far from equilibrium with its strongest peak at around (40, 280).

From Figures 6.7 and 6.10, it can be seen that the behavior of the furnaces change drastically after the correction for solid phases in the slag, except for the AOD which continued to show a similar distribution since its slags were the closest to being fully liquid and it has intense stirring.

It is interesting to see that BOF 1 has  $L_{PS}$  of about 50 or so no matter what slag was being used. This points to the fact that steel refining is being highly limited by



liquid phase mass transfer, most probably due to insufficient stirring since BOF 1 has slags that are mostly liquid as will be discussed. BOF 2 is in a slightly different regime than BOF 1 but its slags are predicted to have a somewhat lower equilibrium  $L_P$ . The change is the most drastic for the Q-BOP as a results of having the highest amount of solid phases predicted by FactSage, thus it also has the biggest change in the liquid slag composition since so many solids were present. The Q-BOP now has most of its heats away from equilibrium by a factor of 3 to 5. One must remember that, in the aforementioned results, it was assumed that all phosphorus from the bulk slag was present in the liquid slag, *i.e.* phosphorus has no solubility in CaO, MgO and C<sub>2</sub>S. While this assumption is true for CaO and MgO, it is known that phosphorus is significantly soluble in dicalcium silicate. The impact of this solubility is discussed in detail in the next section and will be shown that it has big effects on the Q-BOP.

The AOD had slags closest to a fully liquid state with most of its slag compositions falling in to the 90% range of liquid fraction. BOF 1 had most of its liquid fraction in the 85% to 93% range. BOF 2 shows a flatter distribution falling in the 75% to 87% range. The Q-BOP is the reactor with the most solids with significant amounts of data in the 50-70% liquid range. Most of its liquid fractions are in the 70% range meaning that there is always a high amount of undissolved phases present during its operation. It should be stressed that these are calculated results using FactSage, which may underestimate the MgO solubility in the liquid slag.

It is important to roughly quantify the impact of the underestimation of MgO solubility in the liquid slag. As previously discussed in Section 5.4.3, FactSage can underestimate the MgO saturation by a factor of up to 2. Based on this value, it is possible to qualitatively reevaluate the impact that a higher MgO saturation would have on the equilibrium  $L_P$ . Clearly, by having more MgO in the liquid slag would result in a dilution effect on the other components. This means that the concentration

of all other components would decrease as a result of having more MgO present in the liquid slag. By rearranging Equation 5.18 we get:

$$L_P = 10^{0.073 \left[ (\%CaO) + 0.148(\%MgO) + 0.8(\%P_2O_5) + 0.113(\%SiO_2) \right] + \frac{11570}{T} - 10.403} \times (T.Fe)^{\frac{5}{2}} \quad (6.1)$$

From the equation above, it is possible to see the what would be the effect of MgO on  $L_P$ . The concentration of CaO,  $P_2O_5$  and  $SiO_2$  would decrease. Taking into account that the MgO coefficient is much smaller than CaO and  $P_2O_5$ , the compositional term  $(\%CaO) + 0.178(\%MgO) + 0.8(\%P_2O_5) + 0.113(\%SiO_2)$ , would decrease. Additionally, the FeO concentration would also decrease, resulting in a decrease of the term  $(T.Fe)^{\frac{5}{2}}$ . Therefore, the equilibrium  $L_P$  would experience some decrease if a higher MgO saturation is used. Figure 6.12 shows the calculated equilibrium  $L_P$  using the FactSage MgO saturation as well as if this saturation was multiplied by a factor of 2 for the Q-BOP. The data used in these plots only contained monoxides as possible solid phases (CaO and MgO), data containing dicalcium silicate was not considered. Both scatter and contour plots are presented.

As expected, the equilibrium  $L_P$  is lower for a higher MgO saturation. In this particular scenario, it appears that the equilibrium  $L_P$  has decreased by 100 to 150 units. Although this difference is somewhat significant, these numbers should not be taken as quantitative.

From all the aforementioned results one can conclude that the AOD has slags very close to fully liquid, it is also the highest stirred reactor and is the closest to equilibrium. Next, the Q-BOP has most of its data away from equilibrium but several heats closer. It also has the highest amount of solids in the slag. BOF 1 operates in a way that appears to be independent of slag composition since it is in a vertical

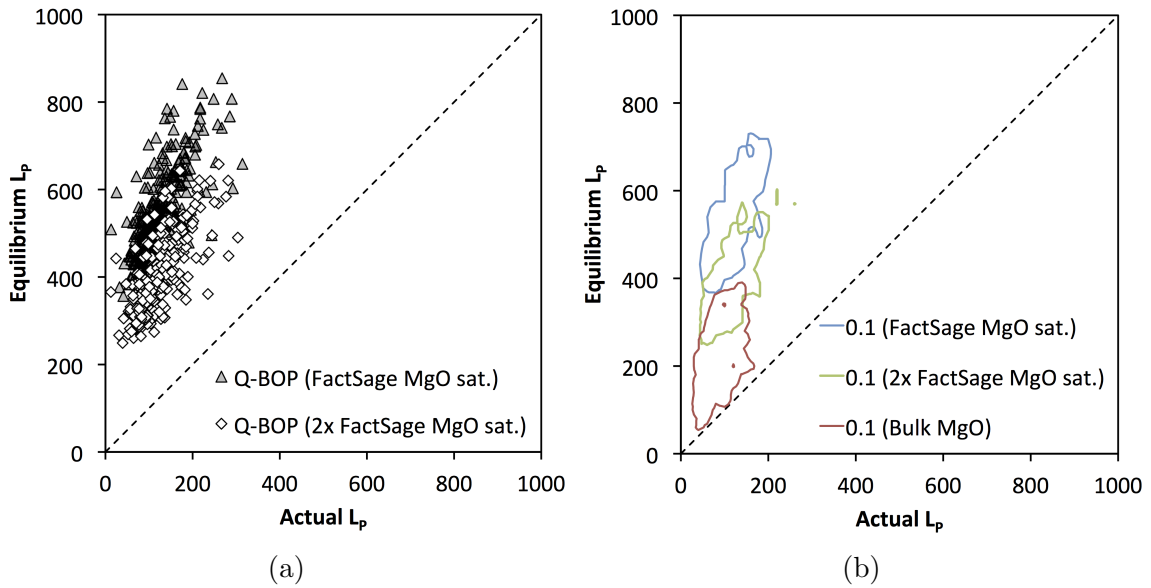


Figure 6.12: Scatter plot (6.12a) and contour plot (6.12b) of Actual  $L_p$  vs. Equilibrium  $L_p$  for the Q-BOP data containing monoxide phases predicted by FactSage for two MgO saturation levels: original FactSage prediction and twice the FactSage prediction; and bulk slag (6.12b).

regime as shown in Figure 6.10. BOF 2 has a slightly better performance than BOF 1, operating in a regime that is situated between BOF 1 and the Q-BOP.

The author believes that it is very important to keep the slag as liquid as possible during throughout a heat. This may be achieved by, instead of making just one big addition of CaO and MgO in the beginning of the heat, adding the fluxes in 2 to 4 batches in order to control the dissolution of CaO and MgO and keep the FeO in the liquid slag at a level around 20-25 wt.% to help dilute the additions during the heat.

In summary, this review of plant data points out that there is an optimum balance between slag composition and reactor stirring to ensure results close to equilibrium. Having just the right slag or just enough stirring is not optimum. These two variables have to be monitored closely to improve the performance of a given reactor regarding phosphorus removal. Also, the author believes that correcting the bulk slag composition for solid phases provides a better picture of the reactor's performance and

this should be used to design optimum slags based on the individual needs of a given plant.

#### 6.4.1 Impact of Dicalcium Silicate on Lp

As previously mentioned on Section 3.2.2, phosphates are soluble in  $2\text{CaO}.\text{SiO}_2$ . This means that, if dicalcium silicate is present as a co-existing phase in the bulk slag, phosphorus can be removed from the liquid slag and precipitate in the  $2\text{CaO}.\text{SiO}_2$  particles as  $3\text{CaO}.\text{P}_2\text{O}_5$ . By removing phosphorus from the liquid slag, the phosphate capacity of the liquid slag is kept high and metal dephosphorization can occur to a greater extent. Therefore, it is useful to understand how the presence of  $2\text{CaO}.\text{SiO}_2$  could impact Lp.

Inoue and Suito [18] studied the phosphorus partition between  $2\text{CaO}.\text{SiO}_2$  particles and  $\text{CaO-SiO}_2\text{-Fe}_t\text{O}$  slags. From the data provided in their paper, it seems that the phosphorus partition  $2\text{CaO}.\text{SiO}_2$  and slags,  $L'_P$ , can be reasonably predicted by a logarithmic function of the binary basicity, as given by Equation 6.2 and shown in Figure 6.13

$$L'_P = 38.484 \ln \frac{(\% \text{CaO})}{(\% \text{SiO}_2)} - 3.11 \quad (6.2)$$

Where  $L'_P$  is given by:

$$L'_P = \frac{(wt.\% P_{(2\text{CaO}.\text{SiO}_2)})}{(wt.\% P_{slag})} \quad (6.3)$$

By a simple mass balance, the amount of phosphorus present in the liquid slag and in the dicalcium silicate particles can be expressed as:

$$m_{P_2O_5}^{C_2S} = \frac{m_{P_2O_5}^{total} \times L'_P \times m_{C_2S}}{m_{slag} + (L'_P \times m_{C_2S})} \quad (6.4)$$

$$m_{P_2O_5}^{slag} = m_{P_2O_5}^{total} - m_{P_2O_5}^{C_2S} \quad (6.5)$$

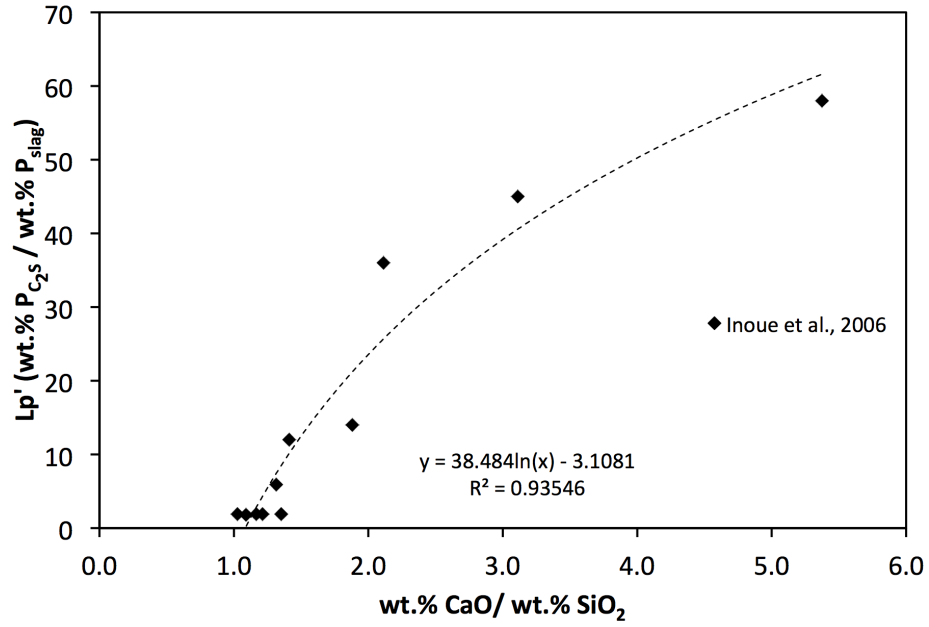
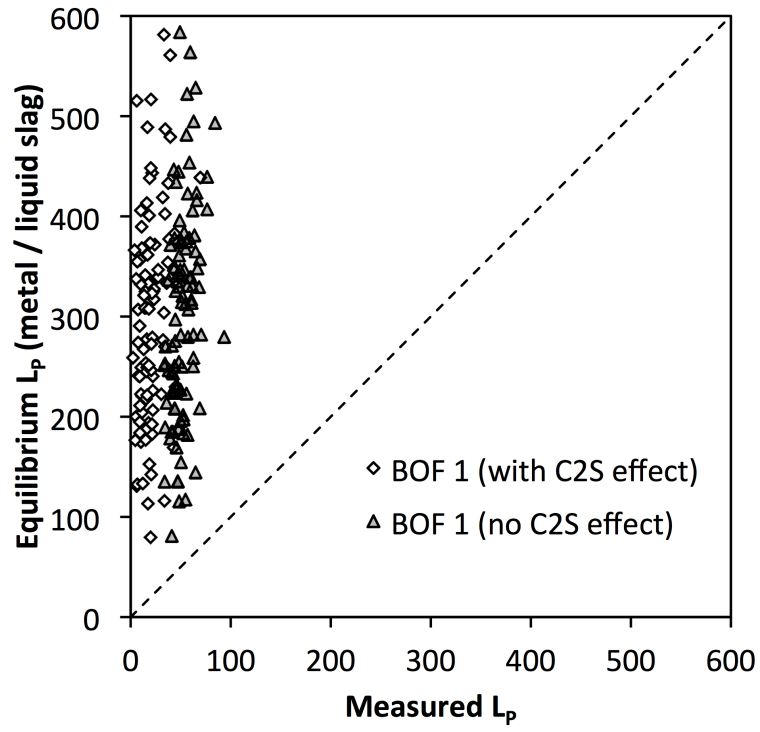


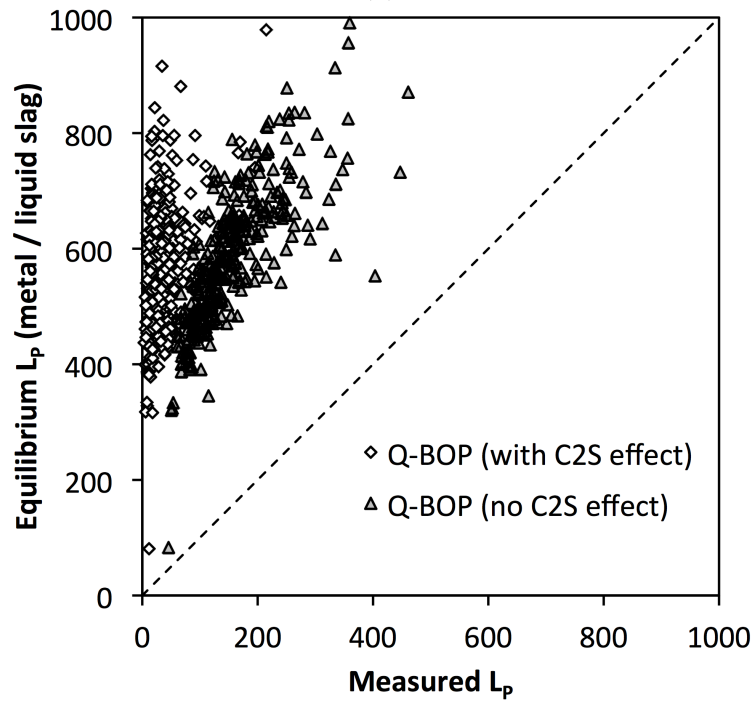
Figure 6.13:  $L'_P$  as a function of binary basicity. Data from [18].

Where  $m_{P_2O_5}^{slag}$ ,  $m_{P_2O_5}^{C_2S}$  and  $m_{P_2O_5}^{total}$  correspond to the mass of  $P_2O_5$  present in the slag, in dicalcium silicate and the total respectively. Additionally,  $m_{C_2S}$  and  $m_{slag}$  correspond to the mass of dicalcium silicate and liquid slag respectively.

Based on the previous equations, it is possible to evaluate how  $L'_P$  would influence  $L_P$ . Figure 6.14 shows the impact on  $L_P$  if we consider the effect of  $2CaO.SiO_2$  on the phosphorus distribution.



(a)



(b)

Figure 6.14: Impact of  $L'_P$  on  $L_P$  for BOF1 (6.14a) and Q-BOP (6.14b).

From Figure 6.14, it can be seen that, as expected, the presence of dicalcium silicate in the bulk slag shifts the data away from the diagonal of the plots. This behavior is congruent with the fact that, by removing phosphorus from the liquid slag, the phosphorus capacity in the slag continues to be high and a more phosphorus could be removed from the metal. Also, it is seen that shifts mostly leftwards. The leftward shift is due to the fact that the measured or actual  $L_P$  has changed since a considerable amount of phosphorus has been removed from the liquid slag, which decreased the measured  $L_P$  values. The amount by which the data shifts is proportional to the amount of  $C_2S$  predicted by FactSage as well as the  $L'_P$  value given by Equation 6.3. In the case of the Q-BOP, the average value of  $L'_P$  was around 33 and the bulk slag contained an average of 9% dicalcium silicate. This means that the  $C_2S$  particles are capable of absorbing 33 times more phosphorus than the liquid slag. On the other hand, the average value of  $L'_P$  for BOF 1 was around 26 and the bulk slag contained an average of 7% dicalcium silicate. Since the Q-BOP has higher values for both  $L'_P$  and fraction of  $C_2S$  in the slag, its change on the equilibrium  $L_P$  is a lot more pronounced than what was observed for BOF 1.

Finally, we must now revisit the contour plots of Figure 6.9c now that we know the maximum effect of dicalcium silicate on  $L_P$ . The comparison of the before and after for both Q-BOP and BOF 1 is shown in Figures 6.15 and 6.16.

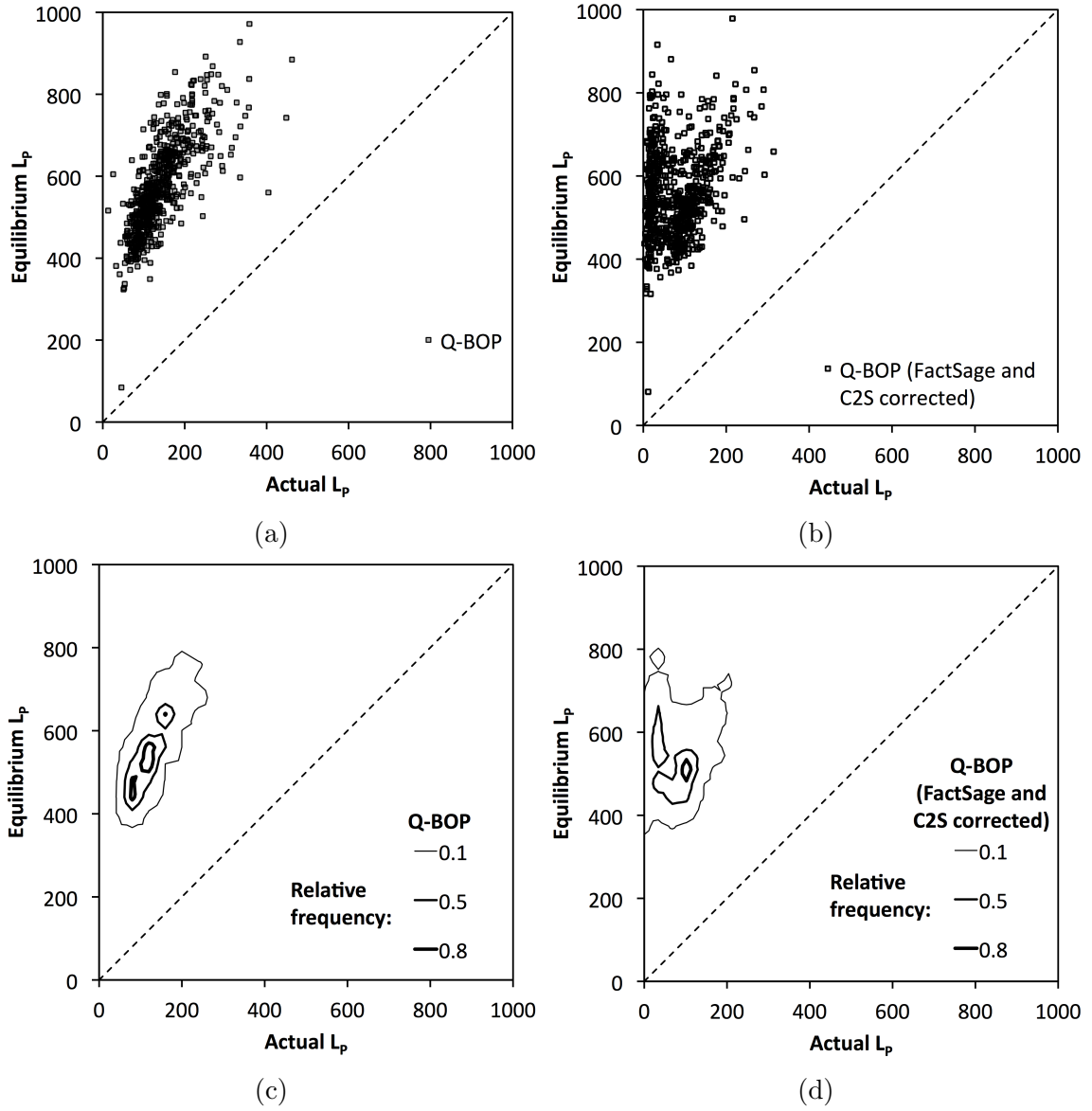


Figure 6.15: Scatter and contour plots for Actual  $L_p$  vs. Equilibrium  $L_p$  for Q-BOP corrected by FactSage (6.15a and 6.15c) and Q-BOP corrected by FactSage and with  $C_2S$  partition taken into account (6.15b and 6.15d)



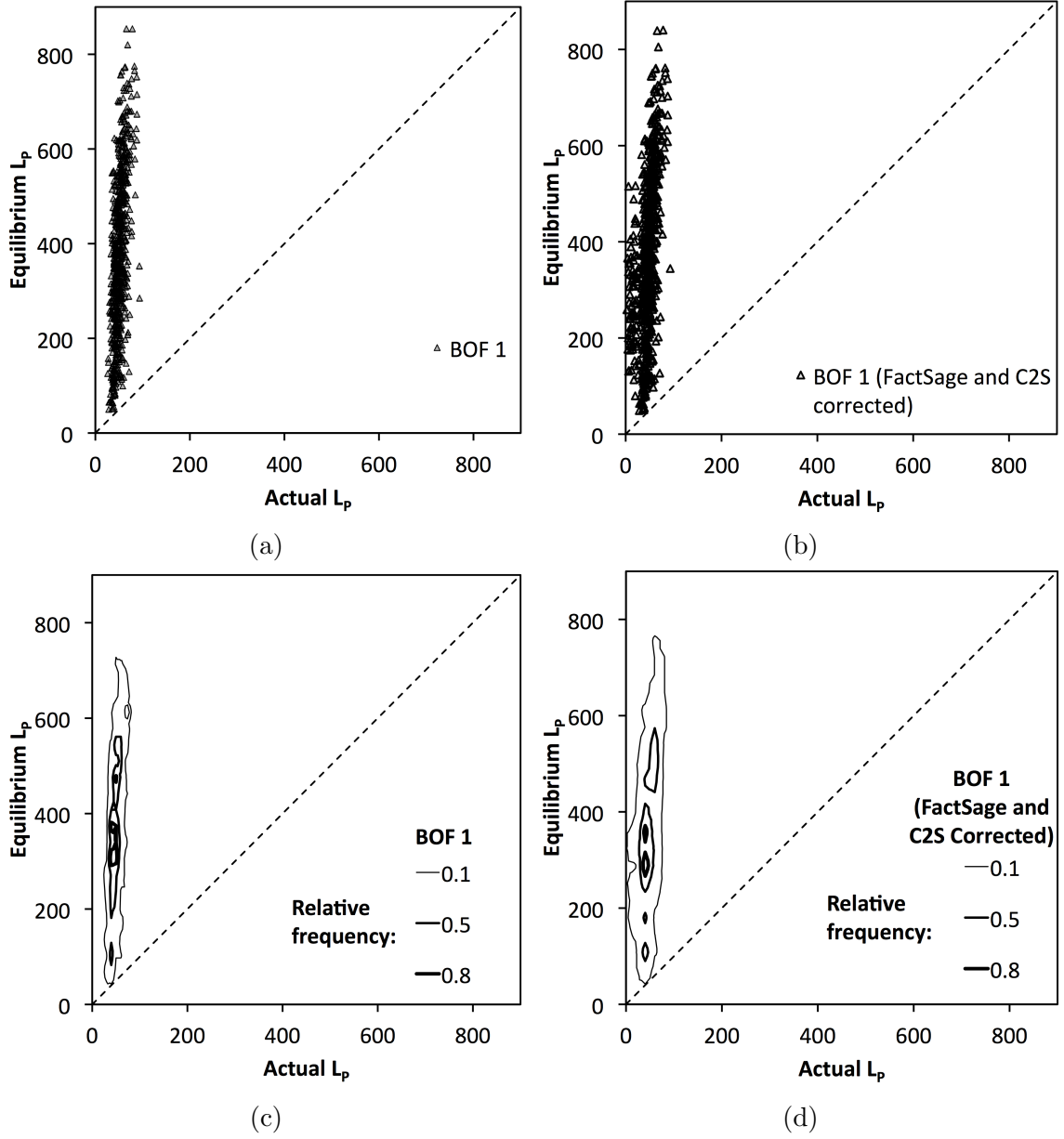


Figure 6.16: Scatter and contour plots for Actual  $L_p$  vs. Equilibrium  $L_p$  for BOF 1 corrected by FactSage (6.16a and 6.16c) and BOF 1 corrected by FactSage *and* with  $C_2S$  partition taken into account (6.16b and 6.16d)

From Figures 6.15 and 6.16 it can be seen that the impact of  $L'_P$  on  $L_P$  is more pronounced for the Q-BOP than BOF 1. This is actually no surprise considering that roughly 50% of all Q-BOP data had significant amounts of dicalcium silicate. On the other hand, less than one third of the data from BOF 1 had  $C_2S$  as a predicted phase. Moreover, the BOF 1 has lesser amounts of  $C_2S$  and its phosphorus solubility is also less than the ones for the Q-BOP. Therefore, the impact of dicalcium silicate on BOF 1 is much less pronounced. Nonetheless, after the consideration of  $C_2S$ , both furnaces became farther from equilibrium, specially for the Q-BOP, which was off by a factor of 10.

Finally, it is important to understand the the previous discussion represents the *maximum* possible effect of dicalcium silicate since it assumes thermodynamic equilibrium between the slag, the  $C_2S$  particles and liquid steel. As we have seen, industrial furnaces do not operate in two-phase equilibrium, let alone a three phase equilibrium such as steel-slag- $C_2S$ , so the actual effect is somewhere in between the two cases presented in this chapter.

## 6.4.2 Summary of this chapter

This chapter reviewed the slag and metal data from four furnaces, one AOD, two BOFs and one Q-BOP or OBM. It was shown that the use of bulk slag composition to study phosphorus partition can introduce uncertainties as a result of solid phases coexisting in the slag. It should be noted that the presented results are for the end of the steelmaking process. The slag chemistry is continuously changing and does not reach its final value until late in the process. The present study took into account three possible solid phases: CaO solid solutions, MgO solid solutions and  $2CaO.SiO_2$ . The bulk slags were then corrected by FactSage in order to examine

something closer to the actual liquid slag composition. Two assumptions were studied regarding how phosphorus could be distributed in the slag: no solubility of phosphorus in the solid phases and phosphorus solubility in  $2\text{CaO}.\text{SiO}_2$ . A detailed evaluation on how dicalcium silicate could impact phosphorus partition between liquid metal and liquid slag was carried.

The major findings are as follows:

- None of the furnaces studied achieved equilibrium with respect to phosphorus. The equilibrium value of  $L_P$  was off by a factor of  $2\pm 1$  for the AOD,  $4\pm 2$  for the Q-BOP,  $8\pm 3$  for BOF 1 and  $7\pm 2$  for BOF 2.
- The AOD is the furnace closest to equilibrium due to its intensive stirring and it has a large fraction of liquid slag. Additionally, it has to transfer less phosphorus to reach equilibrium than the other furnaces.
- The Q-BOP or OBM is farther from equilibrium than the AOD but it is the second closest to equilibrium possibly due to intensive stirring and possibly due to continuous injection of CaO. However, it would possibly achieve better results if it had significantly a higher fraction of liquid slag.
- BOF 1 and BOF 2 operate the farthest from equilibrium and the phosphorus partition is nearly independent from slag composition. Thus, it seems that these furnaces do not have adequate stirring although their slags are relatively liquid.
- The possible underestimation of MgO saturation by FactSage was found not to be very significant and did not alter the operational regime of the furnaces significantly. The degree of non-equilibrium remained similar for both cases.
- The phosphorus content in solid dicalcium silicate *could* greatly impact the

predictions for the Q-BOP or OBM. However, it is unlikely that thermodynamic equilibrium between the slag, metal and  $\text{C}_2\text{S}$  would be achieved.

Lastly, the author realizes the obvious limitations of the discussion presented in this chapter. First, only the turndown slag composition was discussed and assumed to be the slag responsible for dephosphorization. Ideally, the actual “*slag path*” should be studied in order to identify at which point in time the slag becomes optimal for dephosphorization and for how long this given composition is maintained during a heat. Second, the author did not have access to the physical samples and was only provided with the data, it would be interesting to study if different slag sampling tools preferentially sample the liquid fraction or solid fraction. Third, it was assumed thermodynamic equilibrium between the solid phases and the slag. However, steelmaking furnaces rarely operate at equilibrium. Lastly, as previously discussed in Section 5.4.3, FactSage appears to underestimate the  $\text{MgO}$  saturation by a considerable amount, this would have an effect on the amount of undissolved  $\text{MgO}$  coexisting in the slag as well as some influence on the liquid slag composition and the predicted equilibrium phosphorus partition. Further investigation of the above points is beyond the scope of the present work and is suggested for future work.

# Chapter 7

## Studies on Spontaneous Emulsification

### 7.1 Introduction

An emulsion is a mixture of two fluids (liquid or gas) that are immiscible. If two immiscible liquids are at thermodynamic equilibrium, the interfacial area and the system free energy are at a minimum. In this case, in order to promote emulsification, energy has to be supplied to the system and the emulsified state is not thermodynamically stable. However, if two immiscible liquids that are not initially at equilibrium are brought into contact, dynamic interfacial phenomena caused by temporary interfacial instabilities can promote the spontaneous emulsification of the system without external stirring. This phenomenon is often observed in organic and biological ternary systems, with the first observation being recorded in 1879. [60] However, dynamic interfacial phenomena also have important kinetic effects in steelmaking, where the refining of steel relies on good mixing between gas-metal-slag phases.

In oxygen steelmaking (OSM), hot metal and scrap are rapidly refined by the use

of oxygen. [1] The blow of oxygen creates a three phase gas-slag-metal emulsion, which drastically increases the total interfacial area available for several chemical reactions to occur between the phases. Metal droplets are continuously ejected from the bulk metal bath into the slag-gas mixture where they can react for a given amount of time. The generation and behavior of these metal droplets is important for refining processes that are kinetically limited and several authors have studied different aspects of this topic. [6, 43, 47–53]

Various researchers have shown that, during periods of intense mass transfer of surface-active elements, such as oxygen, spontaneous emulsification can occur due to a very pronounced reduction in the interfacial tension between metal-slag systems. [7, 9, 55, 61–63] This behavior is kinetically important as it temporarily increases the interfacial area between metal-slag, thus increasing the rate of a chemical reaction. However, actual quantification of dynamic surface area changes remains scarce.

The work done by Rhamdhani et al. [61–63] is an example of the few studies that have successfully documented how the interfacial area of a metal-slag system changes as a given chemical reaction is allowed to occur between the two phases. They studied the behavior of Fe-Al drops immersed in  $\text{CaO-SiO}_2\text{-Al}_2\text{O}_3$  slags. The interfacial area of the recovered metal droplets was measured using different sizes of papers to cover the droplets and then calculate the area of the papers. They observed that the total interfacial area was a function of the initial reaction rate and could increase by over a factor of 4.

Understanding the behavior of metal droplets immersed in slag is critical for better understanding the kinetic conditions during steelmaking. Spontaneous emulsification seems to occur when rapid mass transfer of oxygen takes place at the interface of metal-slag systems. This results in a substantial decrease in interfacial tension, thus increasing the reaction area and its overall rate. However, direct calculation of changes

in reaction area due to spontaneous emulsification remains difficult.

The studies done so far used metal drops in the range of a few grams which results in drop sizes of several millimetres. However, as reviewed by Koria et al. [52] and from recent results by Millman et al. [5, 52], metal drops recovered from OSM processes can be as small as a few tens or several hundreds of micrometers. As metal drops get smaller, they can behave differently and changes in interfacial area can be dramatically higher than what has been studied so far.

The experimental approach described in the following section was designed in part to observe the interfacial phenomenon and to provide at least semi-quantitative analysis of how the interfacial area of a metal droplet immersed in slag changes as a function of time during dephosphorization. This would enable a better quantification of the overall mass transfer coefficient  $k_0$  since it can be decoupled from the usual mass transfer parameter ( $A_T k_0$ ).

## 7.2 Technical Approach

As previously mentioned, Rhamdhani et al. [61–63] used a simple but effective method to calculate interfacial area of metal drops by using papers to cover the surface of the drops and then calculate the total area of the papers. However, as metal drops get smaller in size and weight, it becomes unfeasible to try to physically recover and measure the area all of the droplets. Additionally, the overall size of the experiments has to be reduced to avoid the needle in a haystack problem. Furthermore, break up of small droplets and re-combination may occur during shorter time periods than in larger drops and therefore the temporal resolution needs to be finer.

To address these complications, the author used a Confocal Laser Scanning Microscope (CSLM) with an integrated hot stage to run the high temperature experiments

and X-Ray Computed Tomography (XCT) to quantify interfacial area in a consistent manner.

Two separate sets of experiments were performed. First, phosphorus was transferred only from the metal to the slag. The slag system used was  $\text{CaO-SiO}_2\text{-MgO-FeO-P}_2\text{O}_5$ . Second, oxygen was transfer from the slag to the metal. In this case, the slag system used was  $\text{CaO-SiO}_2\text{-MgO-FeO}$ . The materials and experimental apparatus are described below.

### **7.2.1 Raw Materials**

#### **Fe-P Master Alloy**

The master alloy, MA2, was used for the kinetics experiments. As described in Section 5.2.1, it consists of a Fe-0.2wt.% P alloy kindly provided by United States Steel Corporation. The alloy was professionally machined to small iron cylinders measuring 1.19mm in height and 1.49mm in diameter. Each iron button weighted about 17mg.

#### **De-P Master Slag**

The De-P master slag was pre-melted using magnesia crucibles in a horizontal tube furnace in an argon atmosphere to ensure a fully liquid slag would readily form once its melting point was reached when running the actual CSLM experiments. After the slag pre-melting, the crucible was ground using SiC grinding paper #60. The recovered solid slag was pulverized on a puck mill to achieve a fine, homogeneous powder. The designed master slag was analyzed by X-Ray Fluorescence (XRF) and had the composition shown in Table 7.1.



Table 7.1: Chemical Composition of the Master Slag Used for Kinetics Experiments.

%CaO	%MgO	%SiO <sub>2</sub>	%FeO <sub>t</sub>	%P <sub>2</sub> O <sub>5</sub>	CaO/SiO <sub>2</sub>
38.2	7.38	17.7	34.98	2.73	2.16

### Low Oxygen Master Alloy

Another master alloy containing 34ppm of oxygen and only traces of phosphorus was used for the oxidation experiments. It was supplied by Alfa Aesar in the form a 2.0mm diameter wire. The wire was cut into discs using a low speed saw and a diamond blade. The weight of the resulting discs was between 14 to 16mg. Table 7.2 shows the detailed chemical composition of this alloy reported by Alfa Aesar.

Table 7.2: Chemical composition of low oxygen master alloy.

%Mn	%P	%Ni	%Cr	%Al	%C	%S	%O	%N
0.0003	0.0004	0.0001	0.0003	0.0005	0.004	<0.001	0.0034	<0.001

### Phosphorus-free Master Slag

The phosphorus-free master slag was prepared using the same procedure described for the De-P master slag. The only difference being that no Ca<sub>2</sub>P<sub>2</sub>O<sub>7</sub> was added. The XRF analysis is shown in Table 7.3.

Table 7.3: Chemical Composition of the Phosphorus-free slag used in the oxidation experiments.

%CaO	%MgO	%SiO <sub>2</sub>	%FeO <sub>t</sub>	%P <sub>2</sub> O <sub>5</sub>	CaO/SiO <sub>2</sub>
38.15	10.26	16.89	34.70	0.01	2.26

## **Crucible**

For the same reasons already described in Section 5.2.3, MgO crucibles were used for all kinetic experiments to prevent slag infiltration and crucible dissolution. Their nominal dimensions are: 9mm OD, 8mm ID and 4mm high.

### **7.2.2 The Confocal Scanning Laser Microscope**

For the present study, the Confocal Scanning Laser Microscope (CSLM) was used solely as a furnace due to the fast heating and quenching capabilities of its integrated hot stage. It consists of an ellipsoidal chamber plated with a highly reflective gold coating. In one of the focal points of the ellipsoid sits a halogen lamp, which emits infrared (IR) light. The sample sits on a small platinum holder at the second focal point of the ellipsoid and is heated by the energy provided by the IR radiation from the halogen lamp. A type B thermocouple is integrated into the platinum sample holder and reads the temperature. Because this system uses a lamp, it can heat up quickly, achieving temperatures up to 1700°C in less than 3 minutes. This allows for a short transient period upon heating and cooling of the samples. The atmosphere of the chamber is controlled and argon (99.9999%) was used. A laser beam scans the surface of the sample and its video signal is recorded on a computer using the HiTOS software package. Figure 7.1 shows a schematic diagram of the CSLM and hot stage.

### **Platinum Pan and Alumina Spacer**

Due to the high area/volume ratio of the magnesia crucibles used, there was the possibility that the slag could climb the walls of the crucible and get in contact with the platinum sample holder and thermocouple. In order to avoid costly repairs, the MgO crucible was placed in a Pt pan acting as a secondary container in case any

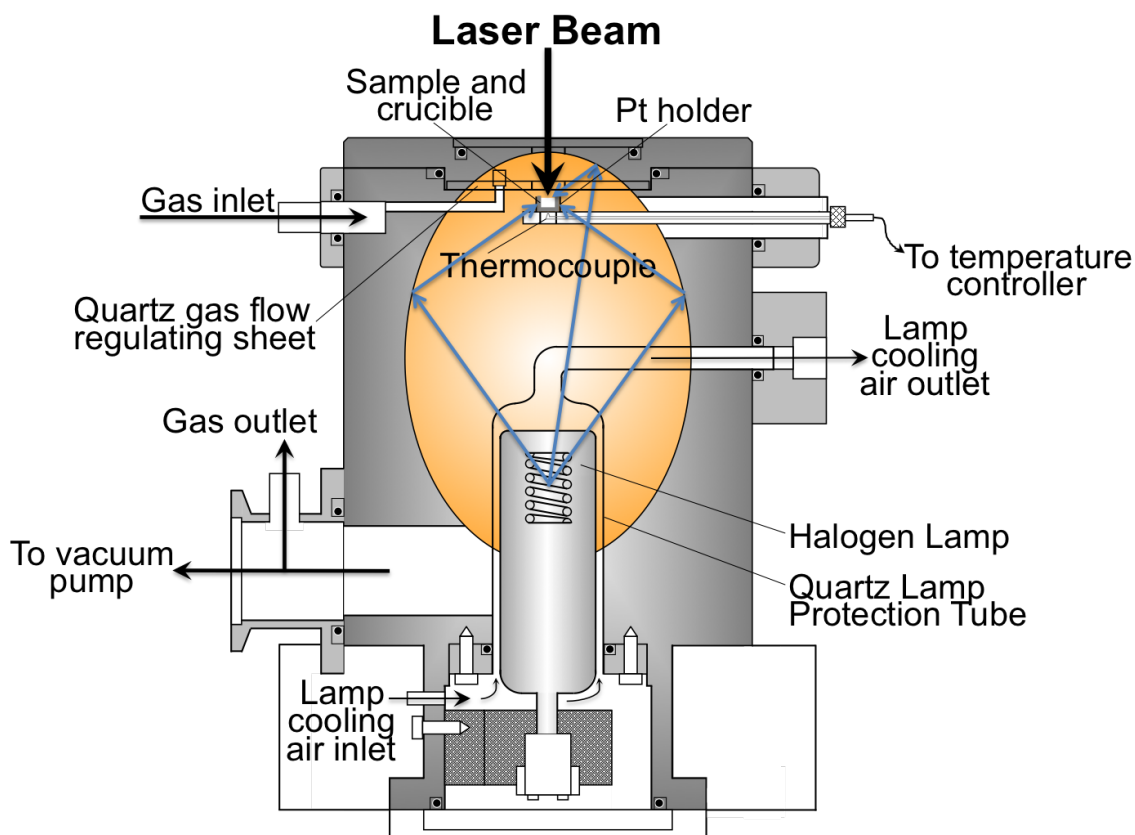


Figure 7.1: Diagram of CSLM experimental setup. (by Prof. Jingxi Wu)

spillage could occur. The platinum pan was made from platinum foil measuring 0.05mm thick.

In order to avoid direct contact between the previously mentioned platinum pan and the platinum sample holder, a very thin  $\text{Al}_2\text{O}_3$  disc spacer was placed between the sample holder and the platinum pan.

### CSLM Temperature Calibration

Temperature calibration of the system was performed using several pure metals and observing the temperature displayed on the hot stage temperature controller when they melted. Table 7.4 shows the pure metals used with their melting point from the

literature and the observed melting point in the CSLM.

Table 7.4: Temperature calibration data for CSLM.

Material	Melting Temp (°C)	Observed Melting Temp (°C)
Copper	1084	1085
Cobalt	1495	1507
Iron	1538	1548

Using the data from Table 7.4, the following equation can be used to determine the correct temperature to be used when programming the CSLM:

$$\text{Controller Temperature} = 1.023 \times (\text{Desired Real Temperature}) - 23.52 \quad (7.1)$$

$$R^2 = 0.9999$$

therefore, if 1600°C is the desired temperature:

$$\text{Controller Temperature} = 1.023 \times (1600) - 23.52 = 1613^\circ\text{C} \quad (7.2)$$

### 7.2.3 Experimental Procedure

The slag was loaded into the crucible and pre-melted at 1625°C for 30 seconds in an argon atmosphere and rapidly cooled at a nominal rate of -1000°C/min.

The crucible was removed from the CSLM and the metal droplet was placed on top of the pre-melted slag with a new addition of pulverized master slag to ensure the droplet would be fully submerged in slag when in liquid state.

The sample was once again loaded into the CSLM and the hot stage is sealed. Purging of the chamber was done as follows:

1. Five minutes of vacuuming achieving a relative pressure of -98kPa;
2. Five minutes of argon gas flowing at 0.25 L/min;
3. Steps 1 and 2 were repeated three times to ensure absence of oxygen in the chamber.

It was important to know the order of magnitude for the equilibration time of the droplet used so one can determine the different holding times for the kinetic experiments. A simple evaluation of  $\frac{Dt}{l^2}$  for diffusion in the metal, provides a estimate of the equilibration time. It must be noted that considering the diffusivity of P only in the metal and not the slag provides a rough initial estimate for the equilibration time.

The Fe-P drops used weighed approximately 0.017g. Considering the density of liquid iron as 6.98 g/cm<sup>3</sup> and that the droplet assumes a spherical shape when in liquid state, the calculated droplet radius is 0.08cm. For diffusion in a sphere,  $\frac{Dt}{l^2}$  to achieve 98% equilibrium equals to 0.5. [64] The phosphorus diffusivity in the metal was taken from [43] as  $4.7 \times 10^{-5}$  cm<sup>2</sup>/sec. It follows that:

$$\frac{Dt}{l^2} = 0.5 \quad (7.3)$$

$$t = \frac{0.5 \times 0.08^2}{4.7 \times 10^{-5}} = 74 \text{ seconds} \quad (7.4)$$

From Equation 7.4, it appears that the equilibration time would be in the order of one or two minutes for mass transfer in the metal phase. With that information, holding times of 0, 5, 10, 20, 30, 60, 90 and 120 seconds were used.

For the oxidation experiments, holding times of 10, 30, 60 and 90 seconds were used.

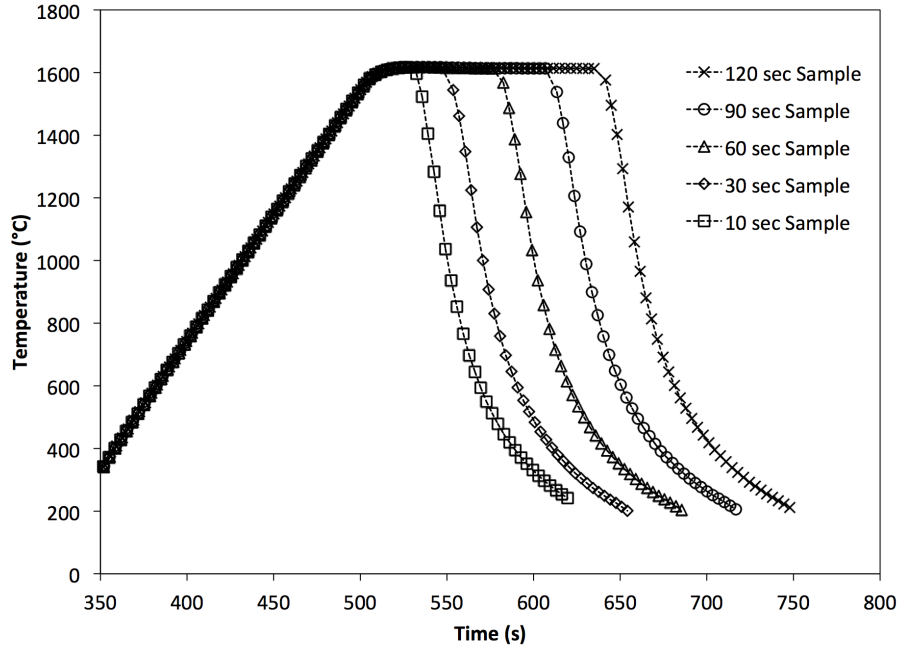


Figure 7.2: Heating profile used for each sample in the CSLM.

The heating profile consists of a preheating stage to ensure longevity of the halogen lamp where temperature was brought up to 300°C at a rate of 50°C/min and held for 45 seconds. The sample was then heated at a rate of 500°C/min until 1613°C and was held for a given amount of time between 0 and 120 seconds. The sample was then quenched using helium gas, flowing at 1.5 liters per minute, at an initial rate of -1200°C/min. The heating and cooling profiles for several samples are shown in Figure 7.2

#### 7.2.4 X-Ray Computed Tomography

XCT has long been used for medical purposes but in the last 25 years has found application in industrial metrology for non-destructive testing and measurement. The method allows full 3D evaluation of objects with no physical modification or destruc-

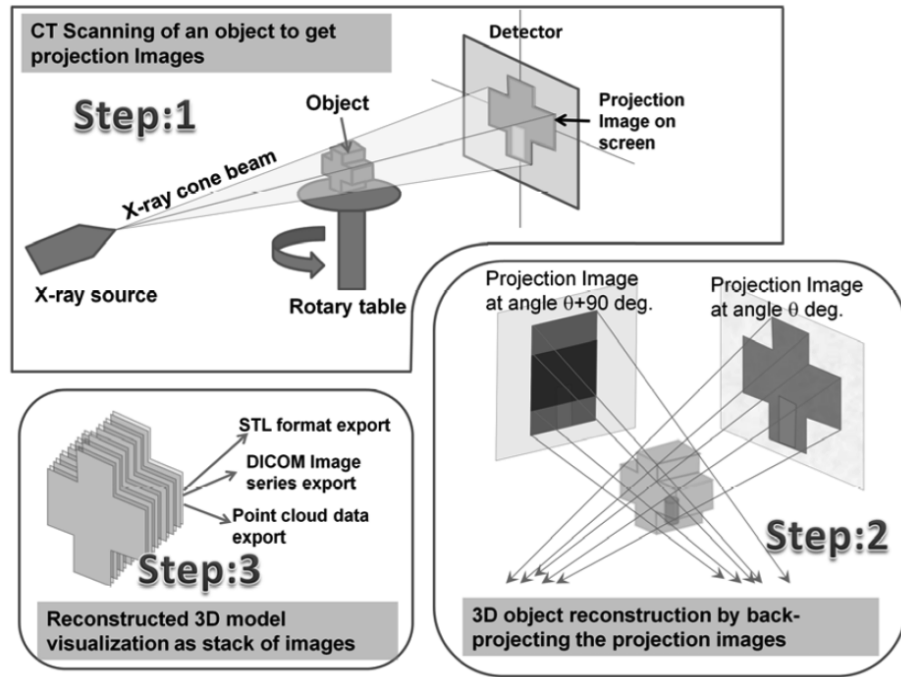


Figure 7.3: Schematic representation of image formation in the XCT process.

tion of the original part.

The setup consists of an x-ray cone beam source and detector with a rotating turntable between for positioning of the object as shown in Figure 7.3. X-rays are produced at the source and pass through the object resulting in an image produced on the detector screen. Where more x-rays have been attenuated by the object a darker patch results on the screen. Images are taken at a variety of angles by rotation of the turntable, and using a method of Feldkamp back projection [65] the object is reconstructed as a series of volume elements known as voxels. Each voxel has an associated grey scale value dependent on the number of attenuated X-rays at the relative position in each projection image, with the calculated voxel size dependent on the magnification of the object. The reconstruction can then be exported for analysis.

The optimal x-ray parameters are determined by the operator. First the magnification is set while containing the entire object within the field of view. Particular x-ray settings are selected to ensure the maximal use of the grey-scale range, while preventing saturation of the signal. If the object contains metal components some filtering at the source must be applied to “harden” the beam, removing lower energy x-rays that would easily scatter and result in artifacts in the scan.

XCT scans for all CSLM samples were kindly performed at the The University of Warwick WMG by Professor Mark Williams, Mr. Jason Warnett and Mr. Stephen Spooner.

### **XCT Settings and Calibration**

Samples were analyzed after quenching at discrete time steps by observing the entire prepared crucible. A Nikon Metrology XT H 320 LC CT scanner was used to investigate the internal characteristics of the prepared crucibles at discrete time-steps. The x-ray source was a 225kV micro focus with a tungsten target. The detector panel constant of 2000 pixels square each 200 microns in size. The parameters for each scan were kept consist as detailed in Table III. Scans were then reconstructed and dimensional evaluation was performed by using the software packages CT-Pro 3D and VGStudio MAX respectively.

The result was a voxel size of 5.06 microns, but CT scanning has its own inherent errors dependent on the given detector-source/source-object distance. This error can be as much as 1% but can be reduced to  $< 0.1\%$  by use of a reference workpiece [66,67]. In this case, a precision ball bar with a center to center distance of 5mm between the two ruby spheres (shown in Figure 7.4) was used as the reference workpiece. The center-to-center distance of the reconstructed model was found to be 5.08mm so all voxels were scaled by a factor of 4.65% accordingly.



Table 7.5: XCT scanning parameters.

Voltage (kV)	220
Power (W)	11
Gain (dB)	12
Exposure (s)	4
Projections	3142
Filter (mm, Cu)	0.5
Magnification	x39.5
Voxel Size (microns)	5.06



Figure 7.4: - Ball bar used as reference work piece in CT scans for voxel scaling to reduce measurement error.

To evaluate the volume and surface area of the iron pellet the volume was individually segmented by process of surface determination based on grey values by selection of an appropriate isosurface. Depending on reasonable isosurface selection, evaluation of volume could vary by up to 10% prior to voxel scaling [68]. To ensure consistency, the selected isosurface was automatically determined by the program by selection of sample voxels considered to be background (air) and then material (iron). Strong contrast in grey values between the slag and the metal aided in a precise determination. All measurements were subject only to a consistent error from the above mechanisms.

### 7.2.5 Chemical Analysis

Previously, as discussed on Chapter 5, ICP-MS or ICP-OES were the techniques used to analyze the metal phase for phosphorus. However, these techniques have spot sizes

on the order of several millimeters and are *not* suitable to analyze a metal drop that measures roughly 1.5mm in diameter. In order to evaluate the phosphorus content in the metal before *and* during emulsification, other techniques had to be used. These include Wavelength Dispersive Spectroscopy (WDS-SEM), Laser Ablation ICP-MS (LA-ICPMS) and Secondary Ion Mass Spectroscopy (SIMS). Each of these techniques have the advantage of having small spot sizes make possible to chemically analyze the metal drop and emulsion. At the time of writing, the author has had limited exposure to these techniques as they are not traditionally usually used for bulk analysis. The use of these methods were more exploratory. The results of each of these methods is discussed below.

## **7.3 De-P Results**

### **7.3.1 3D Images**

Figure 7.5 shows the evolution of the geometry of the metal droplet as a function of time for all time steps. In each image the crucible and the slag phase are shown as independent cross-sections and the metal droplet is shown in front of them.

The results show a dynamic sequence wherein drops break apart completely and recombine within a time period of 120 seconds.

### **7.3.2 Surface Area and Volume Measurements**

The surface area and volume were determined as previously described in Section 7.2.4 after the samples were quenched to room temperature. Table 7.6 and Table 7.7 show the raw data for surface area and volume respectively. The minimum, maximum and selected surface areas and volumes are based on the manually selected grey values.

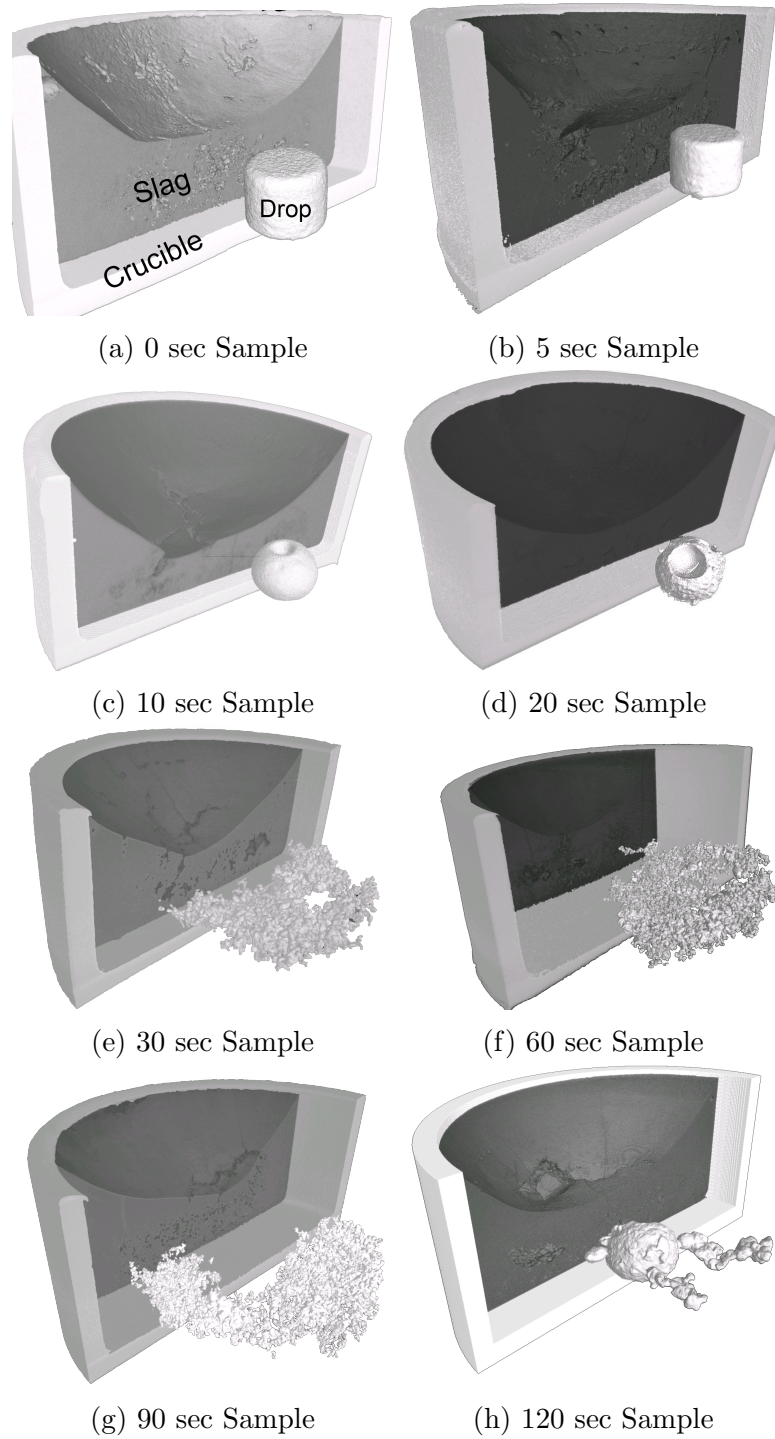


Figure 7.5: Evolution of metal droplet geometry immersed in slag as a function of time for De-P experiments.

Table 7.6: Raw data for surface area measurements.

Time (s)	Surface Area Se- lected ( $\text{mm}^2$ )	Surface Area Max ( $\text{mm}^2$ )	Surface Area Min ( $\text{mm}^2$ )	$A_i/A_0$
0	8.12	8.15	7.93	1
5	8.06	8.11	8	0.99
10	8.84	8.92	8.8	1.09
20	10.56	11.03	10.13	1.3
30	52.95	58.44	44.73	6.52
60	86.85	89.97	77.34	10.7
90	71.03	74.02	61.54	8.75
120	14.32	14.4	14.15	1.76

Table 7.7: Raw data for volume measurements.

Time (s)	Volume Selected ( $\text{mm}^3$ )	Volume Max ( $\text{mm}^3$ )	Volume Min ( $\text{mm}^3$ )	$V_i/V_0$
0	1.82	1.84	1.77	1
5	1.77	1.79	1.74	0.97
10	1.89	1.89	1.87	1.04
20	1.81	1.78	1.81	0.99
30	1.33	1.51	1.17	0.73
60	1.61	1.73	1.43	0.88
90	1.45	1.53	1.26	0.8
120	1.65	1.68	1.65	0.91

### 7.3.3 Chemical Analysis

As previously mentioned on Section 7.2.5, several different analytical techniques were used to quantify P and O in the metal. The original chemical composition of the alloy was analyzed by ICP-MS and LECO and was shown in Table 5.1 back in Chapter 5. Not all samples were analyzed and the summary of the results is shown in Table 7.8.

WDS-SEM was the initially selected tool to analyze the phosphorus content in the metal drops. It is a nondestructive technique and relatively simple to use. WDS offers

Table 7.8: Chemical analysis results for P and O using different techniques.

Reaction Times (s)	(wt.% P)			(wt.% O)	
	ICP-MS	WDS-SEM	LA-ICPMS	LECO	SIMS
Original Alloy	0.201	0.170±0.032	0.0019±0.0001	0.0737	0.213±0.139
0		0.179±0.015			
10		0.002±0.002			
20		0.008±0.005			
30		0.003±0.002			

better peak resolution and separation than EDS and can potentially detect concentrations below 1wt.% with the usage of proper standards. Unlike EDS, the detector reads and counts x-rays generated of a single wavelength at a time that are diffracted by a crystal of proper lattice spacing. In the present study the standards used were pure Fe and GaP for iron and phosphorus respectively. Each of the standards were used to standardize accelerating beam voltages of 25 and 30kV with spot sizes of 6 and 7. The high accelerating voltages and bigger spot sizes were necessary in order to achieve the highest beam current possible in the SEM, which helps in quantifying low concentrations. Table 7.9 shows the individual settings used for each reading of wt.% P.

Table 7.9: WDS results and scan parameters.

Reaction Time (s)	Beam Current (nA)	wt.% P	Area	Mag.	kV	Spot Size	Fe Scan (s)	Fe Bkgd (s)	P Scan (s)	P Bkgd (s)
0	8.66	0.164	Bulk	6500	30	6	60	20	200	60
0	8.70	0.169	Bulk	6500	30	6	60	20	200	60
0	8.70	0.151	Bulk	6500	30	6	60	20	200	60
0	8.70	2.813	Particle	6500	30	6	60	20	200	60
0	7.78	3.147	Particle	6500	30	6	60	20	200	60
0	8.70	2.932	Particle	6500	30	6	60	20	200	60
0	7.78	1.726	Particle	6500	30	6	60	20	200	60
0	8.29	0.187	Bulk	6500	30	6	60	20	200	60
10	9.48	0.000	Bulk	6500	30	6	100	30	400	60
10	10.70	0.001	Bulk	6500	25	6	30	10	60	10
10	10.70	0.006	Bulk	6500	25	6	30	10	60	10
10	10.93	0.000	Bulk	6500	25	7	100	30	300	60
10	8.29	0.006	Bulk	6500	30	6	60	20	200	60
10	8.59	0.002	Bulk	6500	30	6	60	20	200	60
10	8.59	0.001	Bulk	6500	30	6	60	20	300	90
10	8.73	0.002	Bulk	6500	30	6	60	20	300	90
10	8.73	0.001	Bulk	6500	30	6	60	20	300	90
20	10.72	0.010	Bulk	6500	25	6	30	10	60	10
20	10.72	0.016	Bulk	6500	25	6	30	10	60	10
20	10.72	0.004	Bulk	6500	25	6	30	10	60	10
20	10.72	0.003	Bulk	6500	25	7	30	10	60	10
20	8.80	0.007	Bulk	6500	30	6	60	20	300	90
30	10.72	0.006	Bulk	6500	25	6	30	10	60	10
30	10.72	0.001	Bulk	6500	25	7	30	10	60	10
30	11.06	0.003	Bulk	6500	25	7	100	30	300	60
30	11.06	0.003	Bulk	6500	25	7	100	30	300	60

LA-ICPMS is different than a regular ICP-MS in the sense that uses a focused laser beam to ablate a small area of the sample. This technique was used to double check the data acquired by WDS and only one sample was analyzed using this technique. A total of four measurements were taken using ICP-MS across different regions of the metal drop. Each "shot" ablated roughly  $5\mu\text{m}$  in depth with a spot size of  $100\mu\text{m}$  in diameter. The each individual reading is shown in Table 7.10.

Table 7.10: Phosphorus content results from LA-ICPMS for 20s sample.

LA-ICPMS - 20s Sample	
Reading	wt.% P
1	0.0018
2	0.0020
3	0.0019
4	0.0018
Average	0.0019

Table 7.11: Oxygen content results from SIMS for 20s sample.

SIMS - 20s Sample	
Reading	wt.% O
1	0.104
2	0.336
3	0.192
4	0.403
5	0.037
Average	0.214

SIMS was used for the analysis of oxygen for the 20s sample. SIMS uses a focused ion beam to sputter the surface of the sample. As the ion beam "mills" the surface, secondary ions are generated and these ions are analyzed by a mass spectrometer. Quantification was based on a stainless steel 302 standard. A total 5 "shots" were

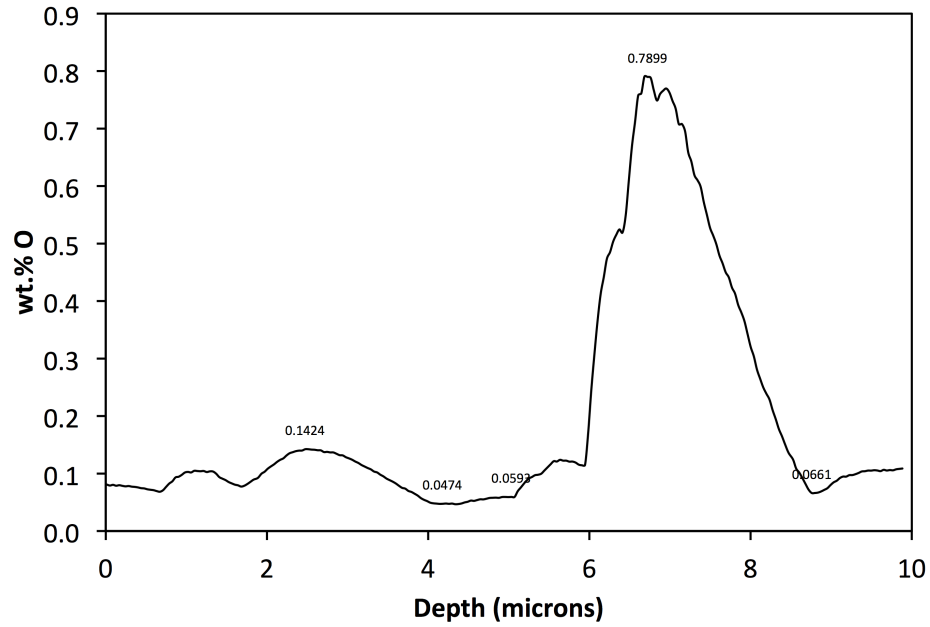


Figure 7.6: Measured oxygen concentration as a function of depth for the 20s sample.

made close to the center of the metal drop. Each shot milled roughly  $10\mu\text{m}$  in depth with a spot size of  $30\mu\text{m}$ . The individual measurements are shown in Table 7.11.

A sixth oxygen measurement was performed using SIMS to generate a depth profile of the oxygen concentration. This is shown in Figure 7.6.

## 7.4 Oxidation Results

### 7.4.1 3D Images

Figure 7.7 shows the evolution of the geometry of the metal droplet as a function of time for all time steps performed for the Oxidation experiments.

The results show a dynamic sequence wherein drops break apart completely at around 90 seconds of reaction time.



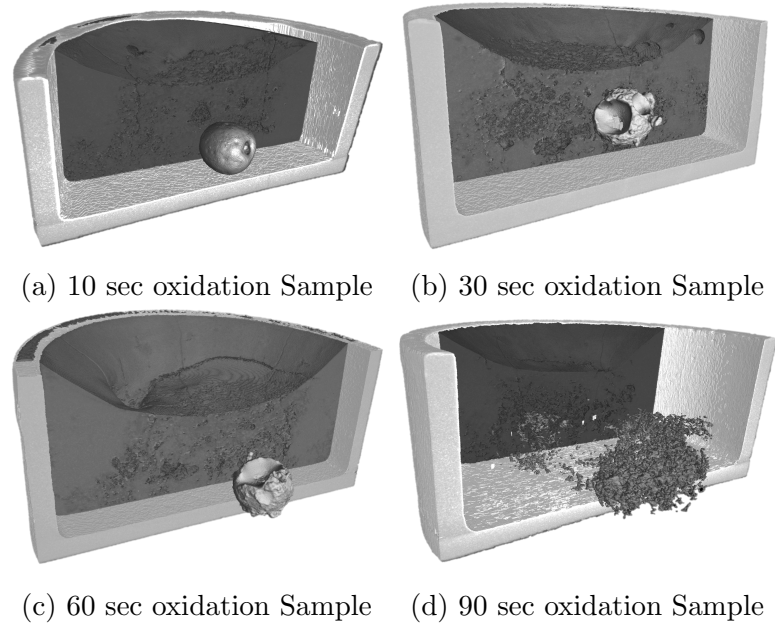


Figure 7.7: Evolution of metal droplet geometry immersed in slag as a function of time for oxidation experiments.

#### 7.4.2 Surface Area and Volume Measurements

Table 7.12 and Table 7.13 show the raw data for surface area and volume respectively for the oxidation experiments. The minimum, maximum and selected surface areas and volumes are based on the manually selected grey values.

Table 7.12: Surface area measurements for oxidation experiments.

Time (s)	Surface Area Se- lected (mm <sup>2</sup> )	Surface Area Max (mm <sup>2</sup> )	Surface Area Min (mm <sup>2</sup> )	$A_i/A_0$
10	6.60	6.60	N.A.	1.00
30	8.37	8.38	8.36	1.27
60	6.84	6.86	6.83	1.04
90	65.75	73.69	58.13	9.96

Table 7.13: Volume measurements for oxidation experiments.

Time (s)	Volume Selected (mm <sup>3</sup> )	Volume Max (mm <sup>3</sup> )	Volume Min (mm <sup>3</sup> )	$V_i/V_0$
10	1.29	1.30	1.28	1.00
30	1.31	1.32	1.30	1.02
60	1.19	1.19	1.18	0.92
90	0.96	1.10	0.83	0.74

## 7.5 Discussion

### 7.5.1 Dynamic Changes in Surface Area

From Figure 7.5, it can be seen that there is a delay in the onset of significant slag/metal reaction due to the time it takes for the sample to melt. Ideally, the 0 second sample would correspond to a fully liquid, spherical metal droplet, if the response time with respect to furnace heating was zero. However, at 0 seconds, the iron button is still in its original solid shape and heat conduction limits the melting of the button. This means that even though the furnace has already achieved the programmed temperature of 1613°C, the temperature in the vicinity of the iron button is still below its melting point. The same behavior is seen for the 5 seconds sample. At 10 seconds the droplet is in fully liquid state and has acquired a spherical shape. Additionally, the surface area has increased by roughly 9%. After 20 seconds the surface of the droplet is considerably rougher and it is possible to see packets of liquid metal almost breaking apart from the surface. At this stage the rate of mass transfer should be increasing and surface tension starts to decrease.

A drastic change in droplet geometry occurs between 20 and 30 seconds suggesting that the reaction is rapid and surface tension has decreased significantly. At this stage spontaneous emulsification has taken place and the main drop has broken apart into

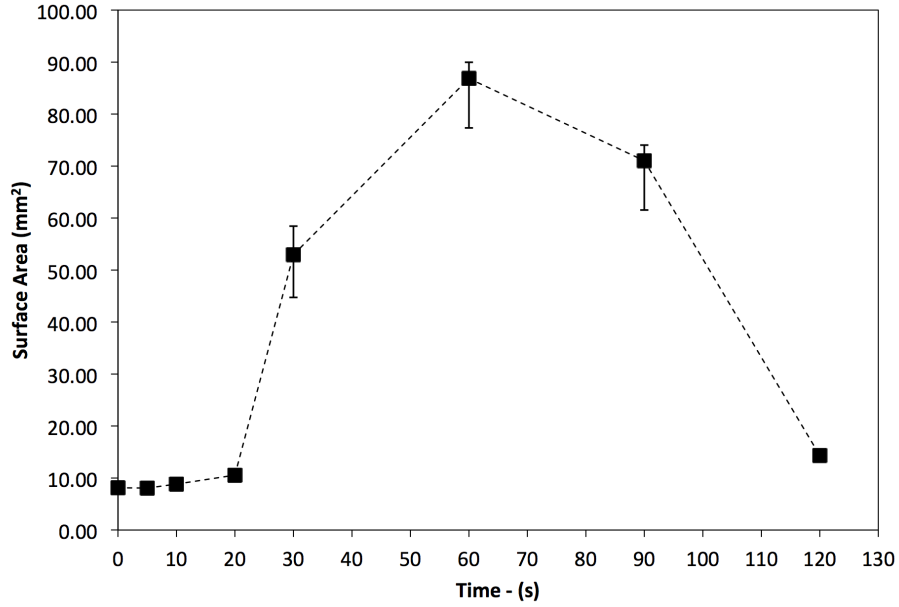


Figure 7.8: Measured surface area of metal droplet for De-P experiments as a function of time.

many small droplets. The surface area increases by a factor higher than 5, going from  $10.56 \text{ mm}^2$  to  $52.95 \text{ mm}^2$ .

From 30 to 60 seconds, the droplets continue to break up and the calculated surface area is over one order of magnitude higher than the original solid droplet. This was the maximum area observed during the experiments. At this stage the surface tension must be close to zero and the mass transfer rate is at its maximum. At 90 seconds the surface area slightly decreases, indicating that mass transfer is slowing down and, after 120 seconds, the droplets have mostly coalesced to a great extent and the calculated surface area reaches a value close to the original liquid droplet. This behavior is graphically shown in Figure 7.8.

The aforementioned results present a degree of emulsification considerably larger than the observed by Rhamdhani et al. [63] where it was reported a maximum increase in interfacial area by a factor of roughly 5. Rhamdhani et al. also studied the

effect of initial droplet size on the amount of observed emulsification. The studied droplet weights ranged from 1.75 to 3.5 grams. They observed that as the droplet size decreased, the total relative change in interfacial area increased. As seen in Figure 7.9, the trend for emulsification does not follow a linear fashion and, as droplets get considerably smaller, the maximum observed change in area drastically increases.

As previously mentioned in Section 3.3, Gaye et al. [7] studied both equilibrium and dynamic properties of several metal-slag combinations. For the study of dynamic interfacial phenomenon, they observed a drastic decrease of dynamic interfacial tension for all systems studied if the initial driving force for a given reaction was high enough. Gaye et al. [7] proposed that, when the oxygen flux across the interface becomes larger than about  $0.1 \text{ g} \cdot \text{atom} \cdot \text{m}^{-2} \cdot \text{s}^{-1}$ , the interfacial tension approaches a value close to zero resulting in an interface of interfacial area. When oxygen flux becomes lower than  $0.01 \text{ g} \cdot \text{atom} \cdot \text{m}^{-2} \cdot \text{s}^{-1}$ , interfacial tension rapidly increases to a value close to the equilibrium tension.

Chung and Cramb [55] studied the dynamic behavior of Fe-Ti alloys and explained the potential mechanisms for spontaneous emulsification by means of fluid flow effects including natural convection and Marangoni flow. They realized that chemical reactions appear to begin locally and would cause local thermal and concentrational gradients that must arise solely due to the reaction since all the experiments were initially isothermal. These local variations caused changes in interfacial tension giving rise to Marangoni flow. The fluid flow at the interface of two liquids of different viscosities will eventually cause the interface to destabilize promoting an increase in interfacial area. Based on the Kelvin-Helmholtz instability, they estimated that if the difference between the velocities of the metal and slag exceeds  $25 \text{ cm/s}$  the interface would be unstable and waves would form. A wavelength of  $0.82 \text{ cm}$  and wave velocity of  $18.4 \text{ cm/s}$  would be generated at the interface when the velocity difference exceeds

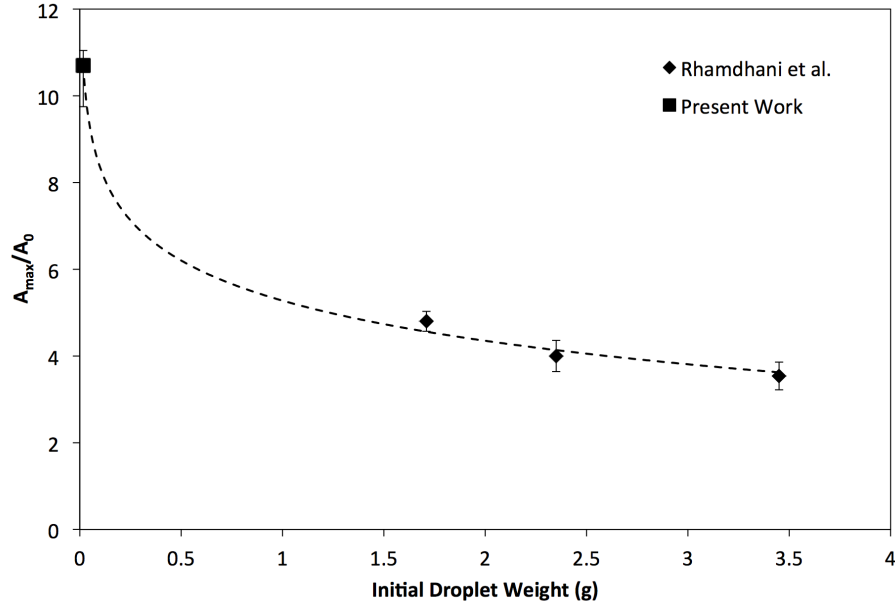


Figure 7.9: Initial droplet weight vs maximum observed change in area.

25cm/s. However, in their study, the majority of the observed wavelengths were less than  $1\mu\text{m}$ , pointing to the fact that the interfacial turbulences greatly exceeded the estimated 25cm/s threshold.

Lopez-Montilla et al. [60] reviewed the various proposed mechanisms for emulsification of immiscible liquids. They include interfacial turbulence; diffusion and stranding; negative interfacial tension; concentration or temperature gradients and Rayleigh instability among other things. The real mechanism for spontaneous emulsification is likely a combination of all the aforementioned observations and some of the proposed mechanisms could be applicable. Nonetheless, the mass transfer of a surface-active element across the metal-slag interface causes local thermal, concentrational and electric potential gradients, which result in local interfacial perturbations. These perturbations give rise to waves at the interface. If mass-transfer is rapid enough, these perturbations can continuously grow and eventually cause spontaneous

emulsification. This would occur more easily if a surfactant is involved. From the dephosphorization reaction, oxygen is involved in the dephosphorization reaction and is a known surfactant. It is also possible that phosphorus itself is a surfactant.

It is important to note that the measured surface areas from Table 7.6 may not correspond to the actual metal/slag interfacial area in the liquid state. Ideally, when both phases are in the liquid state, the interfacial area should be equal to the surface area of the droplets. However, during the quenching of the samples, there are a few factors that can distort the surface area. The shrinkage of the droplets during solidification, for example, could either increase or decrease the surface area depending on the geometry the solidified droplets acquire. Voids can also form around the solidified metal droplets due to this shrinkage. Cracks can also appear in the slag due to the rapid solidification and pores are also commonly observed. These are all factors that make a precise estimate of the true reaction interfacial area a lot more complex. Nonetheless, these measurements provide at least relative area changes that should be closely related to the real interfacial area.

### **7.5.2 The Theories**

Section 7.5.1 discussed in detail the theory behind spontaneous emulsification and how mass transfer of surface active elements are a basic requirement for the observed phenomenon. This section focuses on utilizing the results obtained from Table 7.8 to make better sense of the phenomenon. Several of these results were surprising to the author. Consequently, for each unexpected result, the theory to describe the observed emulsification had to be revised. The following subsections will present a series of theories organized by relevance, each of the theories are critically assessed.

## The Dephosphorization Theory

The experiments discussed in this chapter were originally designed to study the dephosphorization of a metal drop with slag for different reaction times. The starting phosphorus content of the alloy was 0.2wt.% as previously detailed in Table 5.1. The expected equilibrium phosphorus content was expected to be below 50ppm for the slag described in Table 7.1.

It was initially hypothesized that the emulsification behavior discussed in Section 7.5.1 was due to the dephosphorization reaction since it involves the transfer of oxygen across the metal-slag interface to promote the oxidation of phosphorus into phosphate ions and the reduction of FeO into metallic Fe. Continuous emulsification would occur as long as the rate of the reaction was fast. Coalescence would start to occur as the reaction slowed down.

After the dynamic changes in surface area had been properly measured, the next logical step was to quantify the phosphorus content in the metal for each individual sample. As previously mentioned in Section 7.3.3, WDS was the first technique used. Each of the samples were cross-sectioned, mirror polished using diamond suspensions and coated with carbon. Platinum coating was avoided in order to prevent overlapping with phosphorus peaks.

A schematic representation of what was expected from the phosphorus measurements is shown in Figure 7.10. Assuming no phosphorus transfer in solid state, the reaction would start as soon as the metal drop melted, at around 10 seconds, at a fast enough rate to promote emulsification. From 60 to 90 seconds the reaction would start to slow down and at 120 seconds the rate would be very slow as the reaction approached thermodynamic equilibrium. However, this theory proved to be questionable.

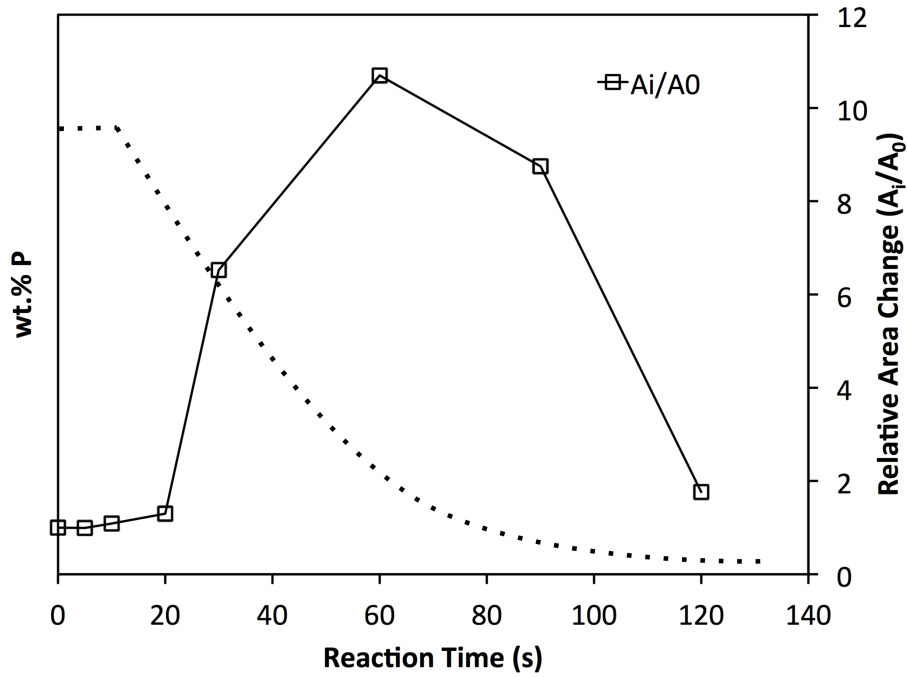


Figure 7.10: Expected phosphorus concentration profile as a function of reaction time. Dotted line is only schematic.

During the analysis of the 0s and 5s samples, SEM images revealed the presence of phosphorus-rich particles all across the metal drop. WDS was used to analyze several of these particles as well as the matrix of the drop. Examples of these particles are shown in Figure 7.11. These particles had phosphorus contents in the range of 1 to 4wt.% as previously shown in Table 7.9. On the other hand, the phosphorus concentration in the matrix of the metal drop was on the range of 0.15 to 0.19wt.%.

Based on these findings, several low magnification pictures were used to estimate the area fraction of the particles. The software ImageJ was used to create binary representations of the images and perform these calculations. An example of how a binary image looks like is shown in Figure 7.12. The particles are identified based on manual settings of threshold and gray values. The software then counts the particles and calculates the individual area of each particle. This information is then used to



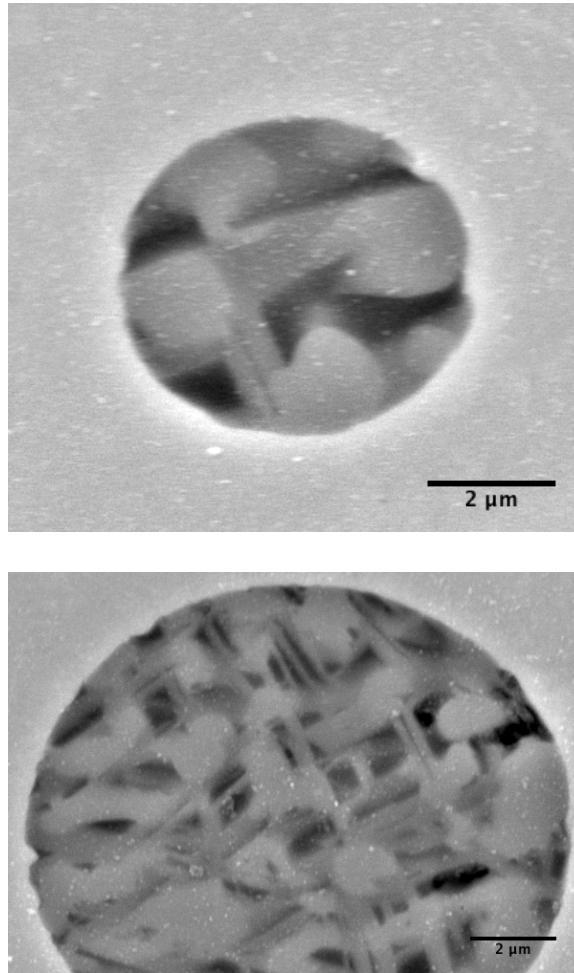
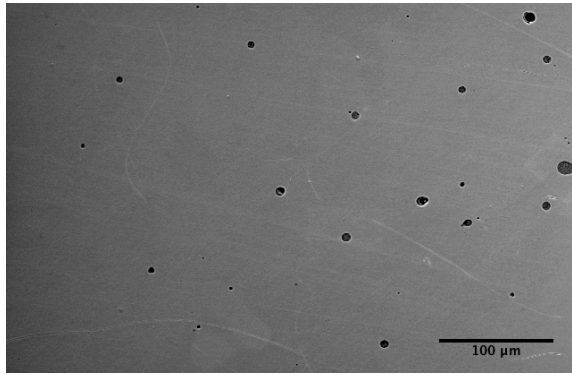
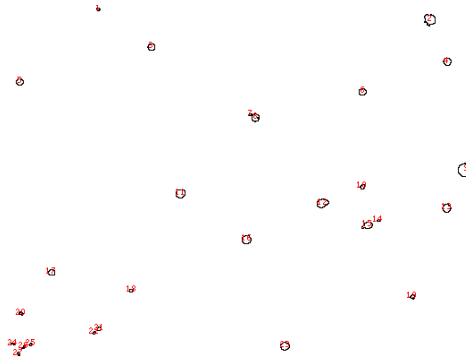


Figure 7.11: Examples P-rich particles found in 0s sample. Secondary electron images taken at 20kV and 8000x.



(a) Low magnification SEM picture of P-rich particles.



(b) Binary image used to calculate area fraction of P-rich particles.

Figure 7.12: Example of image processing to estimate area fraction of particles present in the metal matrix.

estimate the area fraction. Several of these images were used and the calculated area fraction was 0.4%, which is quite small. The results for the 0 second sample, from Table 7.9, were weighted averaged to give the final concentration of  $0.179 \pm 0.015$  wt.% P as previously shown in Table 7.8. This concentration is in reasonable agreement with the *as cast* concentration of the alloy of 0.2 wt.%.

The next samples analyzed by WDS corresponded to reaction times of 10, 20 and 30 seconds. Samples 10s and 20s correspond to spherical drops before emulsification takes place. Sample 30s is the first emulsified sample observed. Surprisingly, all three samples had very similar results: the phosphorus concentration was very low.

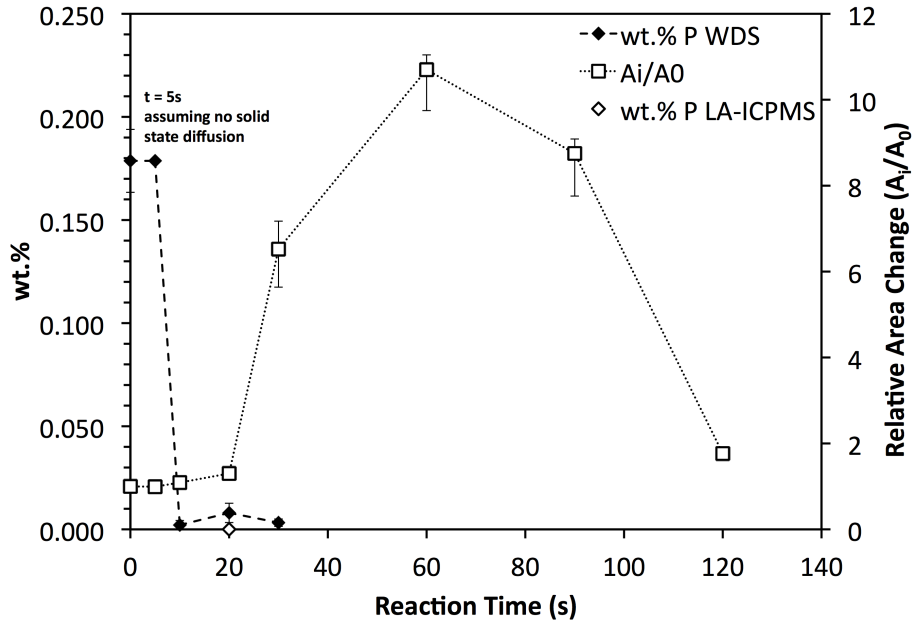


Figure 7.13: Analyzed phosphorus concentration profile as a function of reaction time.

This means that phosphorus from the metal had been removed before the onset of emulsification.

In order to confirm whether these measurements were correct, sample 20s was analyzed by LA-ICPMS and the result was in agreement with the WDS measurement. In face of these findings, it was clear that dephosphorization was *not* responsible for the spontaneous emulsification. Figure 7.13 compiles the results discussed so far.

According to these results, phosphorus appears to have been removed as soon as the metal drop melts. From the XCT images, this must occur somewhere in between 5 and 10 seconds of reaction time, which means phosphorus was removed in less than 5 seconds. Based on these numbers, the author calculated the diffusion coefficients for both static diffusion *and* mass transfer necessary to promote dephosphorization of a sphere for this time scale.

Using Manning's [6] approach previously described on Section 3.3, Equation 7.5

was used to estimate the  $A_T k_0$  parameter for a reaction time of 5 seconds. Table 7.14 shows the values for the variables used and the resulting RHS of the equation.

$$-A_T k_0 t = \frac{W_m}{\rho_m} \frac{1}{1 + \frac{W_m}{L_P W_s}} \ln \left[ \left( 1 + \frac{W_m}{L_P W_s} \right) \frac{[\%P]}{[\%P]_0} - \frac{W_m}{L_P W_s} \right] \quad (7.5)$$

Table 7.14: Results for RHS of Equation 7.5.

Reaction Time (s)	RHS	$W_m$ (g)	$\rho_m$ (g/cm <sup>3</sup> )	$W_s$ (g)	[%P <sub>0</sub> ]	[%P]	Lp
0	0.000	0.017	6.98	0.39	0.179	0.179	370
5	0.011	0.017	6.98	0.39	0.179	0.002	370

It follows that:

$$A_T k_0 = \frac{0.011 - 0.000}{5 - 0} \quad (7.6)$$

$$= 0.002 \frac{cm^3}{s} \quad (7.7)$$

$$\text{but } A_T = 0.088 \text{ cm}^2 \quad (7.8)$$

$$\therefore k_0 = 0.025 \frac{cm}{s} \quad (7.9)$$

Here,  $k_0$  corresponds to the overall mass transfer coefficient and is defined as:

$$k_0 = \frac{1}{\frac{\rho_m}{k_s \rho_s L_P} + \frac{1}{k_m}} \quad (7.10)$$

If we neglect the resistance from the slag,  $k_0 = k_m$ , which is related to a “effective” diffusion coefficient in the metal by Equation 7.11

$$k_m = \frac{D_{eff}}{\delta} \quad (7.11)$$

Where  $\delta$  is the boundary layer thickness in the metal drop. The maximum thick-

ness of the boundary layer in the spherical metal drop is its radius, *i.e.*  $8.4 \times 10^{-2}$  cm. Table 7.15 shows the estimated diffusion coefficients for different boundary layer thicknesses.

Table 7.15: Diffusion coefficient based on mass transfer.

$\delta$ (cm)	$D_{eff}$ (cm <sup>2</sup> /s)
$8.4 \times 10^{-2}$	$2.1 \times 10^{-3}$
$4.2 \times 10^{-2}$	$1.0 \times 10^{-3}$
$2.1 \times 10^{-2}$	$5.2 \times 10^{-4}$
$1.1 \times 10^{-2}$	$2.6 \times 10^{-4}$
$5.3 \times 10^{-3}$	$1.3 \times 10^{-4}$
$2.6 \times 10^{-3}$	$6.5 \times 10^{-5}$
$1.3 \times 10^{-3}$	$3.3 \times 10^{-5}$
$6.6 \times 10^{-4}$	$1.6 \times 10^{-5}$
$3.3 \times 10^{-4}$	$8.1 \times 10^{-6}$

Reasonable values for the diffusion coefficient are only achieved for boundary layer thicknesses below 26 microns. This seems to be a rather small number, but such thin boundary layers are possible if enough convection is present in the system. Convection can occur not only because of pressure, temperature and chemical gradients, but it can also arise from surface tension gradients. This is called Marangoni flow. Chung and Cramb [55] studied the role of Marangoni flow on metal-slag reactions. They proposed that local variations in temperature at the interface caused by a chemical reaction would result in local variations in interfacial tension and Marangoni convection would then take place. They have also proposed that Marangoni flow could be responsible for drop flattening and emulsification. Nonetheless, it is a possibility that Marangoni flow could play a significant role in the convection of the system, resulting in very thin boundary layers ultimately causing rapid mass transfer.

It must be pointed out that the actual reaction time is unknown. However, it must be in the range of 0 to 5 seconds. If, for example, the reaction time was 1 second, the

calculated value of  $k_0$  would be five times larger than 0.025 cm/s, that is 0.125 cm/s. This would require even smaller boundary layer thicknesses than previously discussed. From the available data, the author can only provide a range of the possible mass transfer coefficients, *i.e.*  $10^{-1}$  to  $10^{-2}$  cm/s.

The results for static diffusion in a sphere show unreasonable values for the diffusion coefficient. [64] For a reaction time of 5 seconds, it follows that:

$$\frac{D_{eff} \times t}{l^2} = 0.5 \quad (7.12)$$

$$D_{eff} = \frac{0.5l^2}{t} \quad (7.13)$$

$$D_{eff} = \frac{0.5 \times 0.084^2}{5} \quad (7.14)$$

$$D_{eff} = 7 \times 10^{-4} \text{ cm}^2/\text{s} \quad (7.15)$$

This is the lowest possible value of  $D_{eff}$  for static diffusion but is still one or two orders of magnitude higher than a typical diffusion coefficient for liquids. This points to the fact that it is unlikely that phosphorus was removed due to static diffusion but rather by mass transfer aided by strong convection arising from local gradients in temperature, surface-tension and composition. Further modeling of the fluid dynamic behavior of the system falls outside the scope of the present work, but is encouraged by the author.

In summary, phosphorus removal occurred before the onset of emulsification and thus, does not affect the emulsification behavior of the metal in this particular system. Phosphorus was removed during a time window of 0 to 5 seconds, which corresponds to overall mass transfer coefficients in the order of  $10^{-1}$  to  $10^{-2}$  cm/s. Even if we neglect the resistance from the slag, the required boundary layer thickness in the

metal drop is in the order of micrometers. This means that strong convection is taking place within the metal drop and this convection is a result of temperature, chemical and surface-tension gradients in the drop.

### The Reoxidation Theory

From the previous section, phosphorus was removed from the metal drop before the onset of emulsification. In face of these results, one question still remained: “*What was causing the emulsification?*”.

Phosphorus *and* oxygen should go hand-in-hand in the dephosphorization reaction. If phosphorus was quickly removed from the metal drop, then the dissolved oxygen content in the droplet should also decrease to a low value. This new oxygen content was expected to be well below the Fe-FeO equilibrium and, therefore, oxygen transfer from the slag back into the metal should occur to reestablish the equilibrium oxygen content for the particular slag used in the experiments. This mechanism would follow the following chemical reactions:



Equation 7.16 consumed dissolved oxygen, resulting in a oxygen depleted metal drop that would not be in thermodynamic equilibrium with the oxygen rich slag. At this point, Equation 7.17 would take place in order to *re-oxidize* the metal drop. Since Equation 7.17 involves the transfer of oxygen across the slag-metal interface, it is also a potential candidate to promote emulsification.

The Fe-FeO equilibrium based on the activity of FeO on the master slag used

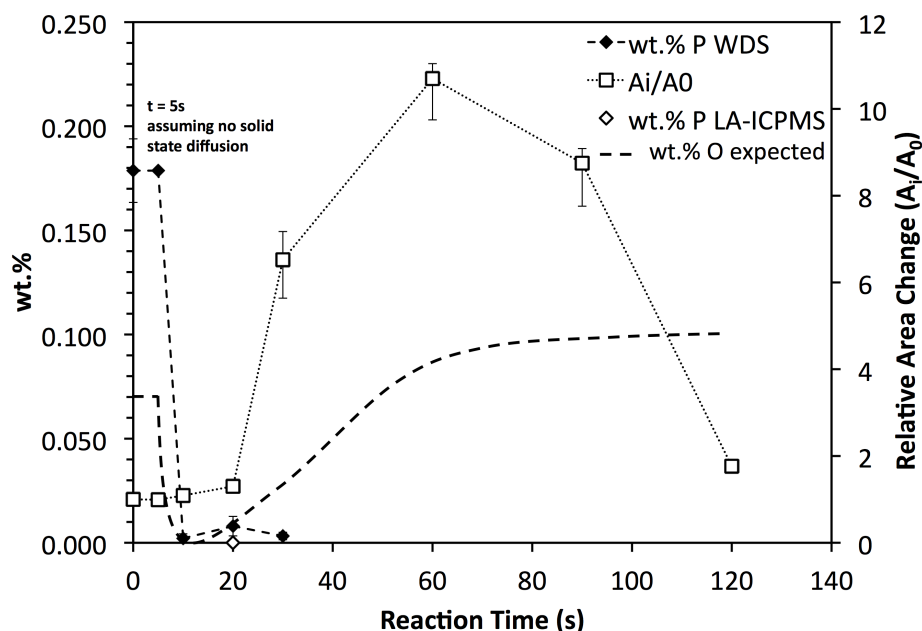


Figure 7.14: Expected oxygen concentration profile as a function of reaction time.

(Table 7.1) was predicted using FactSage. The equilibrium oxygen content in the metal was predicted to be of about 1000ppm.

Based on all the aforementioned points, it was plausible that *reoxidation* was the root cause for emulsification. Figure 7.14 shows a schematic representation of what was expected.

Surprisingly, the SIMS analysis showed oxygen levels with a wide variation as seen in Table 7.11 and Figure 7.6. Based on these results, the average oxygen content was reported to be  $0.213 \pm 0.139$  wt.%. This concentration is significantly higher than the predicted equilibrium oxygen content.

Figure 7.6 also corroborates how heterogeneous the oxygen distribution is across the sample, with values ranging from below equilibrium, *i.e.* 0.047wt.%, to very high concentrations, *i.e.* 0.79wt.%. While SIMS is not commonly used for absolute quantification, it should give values within a factor of 2 with the use of a standard.



Another possibility would be that FeO particles were trapped in the drop. If the ion beam hit a FeO particle, the oxygen concentration would increase and the iron concentration would decrease since FeO has roughly 22wt.% oxygen.

The spot size used for the SIMS analysis had a diameter of  $30\mu\text{m}$ . Based on this information, one can roughly estimate the diameter that a spherical FeO particle must have to cause the peak seen in Figure 7.6. It follows that:

$$\frac{\pi d_{spot}^2}{4} \times 0.79 = \frac{\pi d_{particle}^2}{4} \times 22.3 \quad (7.18)$$

$$d_{particle} = \sqrt{\frac{d_{spot}^2 \times 0.79}{22.3}} \quad (7.19)$$

$$d_{particle} = \sqrt{\frac{30^2 \times 0.79}{22.3}} \quad (7.20)$$

$$d_{particle} \sim 5.6\mu\text{m} \quad (7.21)$$

However, no particles were seen when the sample was observed on the SEM. Also, it appears that the counts per second of iron ions stayed relatively constant across the depth profile as shown in Figure 7.15. If a FeO particle was present, it was expected that the counts for iron ion would decrease *and* coincide with the peak in oxygen concentration. The explanation for the wide variation on the oxygen concentration escapes the author. Figure 7.16 graphically shows the combination of the results discussed so far.

In a last effort to understand if oxygen transfer alone could be responsible for emulsification, the author performed a few oxidation experiments consisting of a low-oxygen drop *and* a phosphorus-free slag as previously mentioned on Section 7.4.

From Figure 7.7 it is clear that oxygen mass-transfer alone is responsible for the break up of the metal drop. The series of images show that emulsification takes place

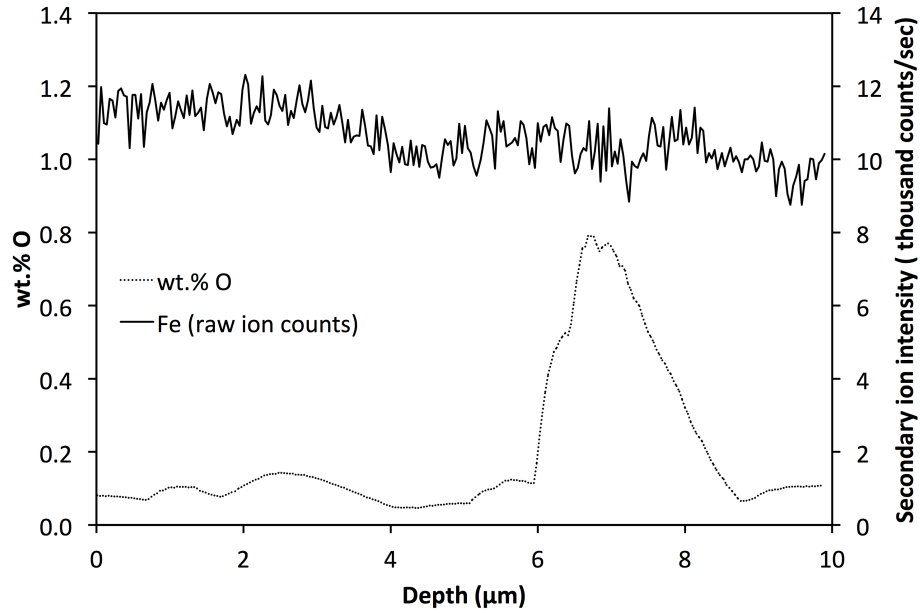


Figure 7.15: Oxygen concentration and iron count rate as a function of depth

between 60 to 90 seconds, which represents a significant delay on the previous series of experiments where emulsification was observed between 20 and 30 seconds. From Table 7.12 it can be seen that the surface area of the drop stays relatively constant for the first 60 seconds of the reaction between 6 to 8 mm<sup>2</sup>. At 90 seconds, the surface area increased by one order of magnitude reaching 65.75 mm<sup>2</sup>. This behavior is graphically shown in Figure 7.17. The relative increase in area is very similar to the one achieved for the 60 seconds sample in the first set of experiments, however, the time on which it occurs differs by up to 30 seconds. This is clear seen if the two normalized area curves are plotted together as shown in Figure 7.18.

In summary, the emulsification seen in the first set of experiments was *not* caused by reoxidation since the oxygen content analyzed by SIMS was well above the equilibrium oxygen for the slag used. It is unclear what caused the metal drop to become over saturated with oxygen however, after it becomes over saturated, it must go

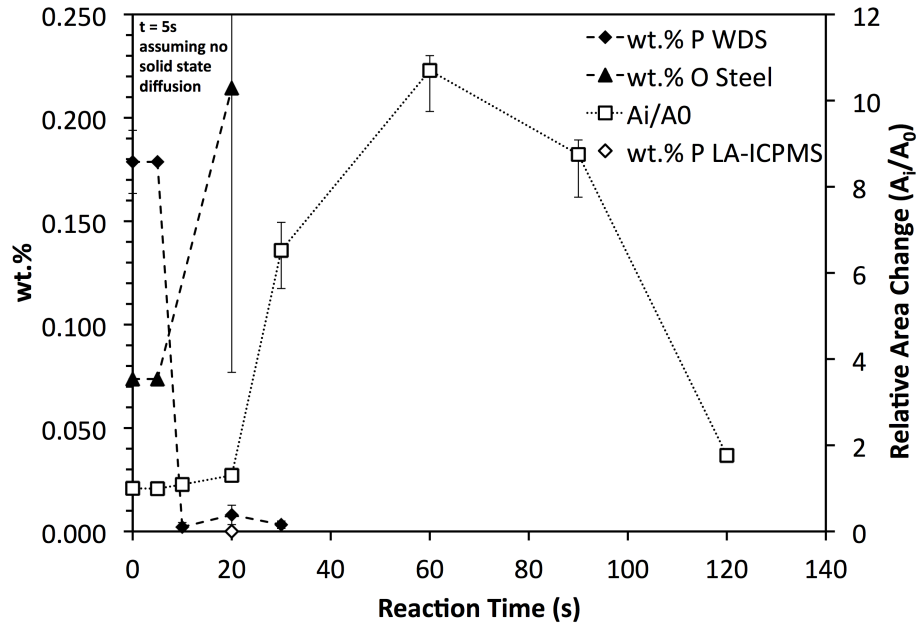


Figure 7.16: Area, phosphorus and oxygen content as a function of reaction time.

through *de-oxidation* to restore the oxygen equilibrium. In this case, oxygen would be transferred from the metal to the slag and emulsification would occur. The second set of experiments transferred oxygen on the opposite direction, *i.e.*, from slag to metal. However, it did validate that oxygen transfer across the metal-slag interface is responsible for spontaneous emulsification. This behavior should occur regardless of the direction of oxygen transfer. Deeper study of de-oxidation or reoxidation of metal falls outside the scope of this project and would take considerable more work. This is again encouraged by the author.

### The Mechanical Removal and Self Dephosphorization Theory

If de-oxidation caused the break up and emulsification of the metal drop for the Fe-P alloy, *how was phosphorus removed so readily from the metal?*

As previously mentioned, phosphorus rich particles were found in the matrix of

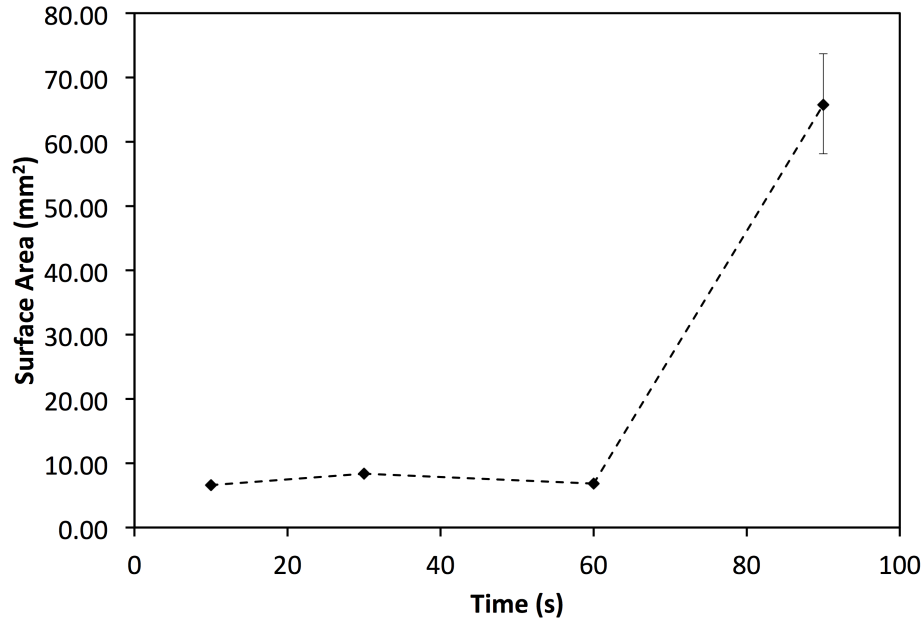


Figure 7.17: Measured surface area of metal droplet as a function of time for oxidation experiments.

the 0 and 5 second samples. These particles had phosphorus contents of up to 3 wt.%. It was also observed that, as soon as the metal drop melts (at 10 seconds) these particles are not present anymore and the phosphorus content had decreased to a value close to equilibrium. If these particles are some form of phosphates, they could be removed from the metal matrix by simple mechanical flotation and buoyancy as soon as the metal drop melts. This flotation would likely occur a lot faster than mass transfer.

However, just the mechanical removal of the P-rich particles cannot explain the total amount of phosphorus that was removed from the drop. The estimated area fraction of the particles is 0.4% and the average phosphorus content in them is 2.65 wt.%. This would account for a decrease in the phosphorus content of the bulk metal of only 0.012 wt.%. The resulting phosphorus content after the mechanical removal of the particles would be 0.168 wt.%

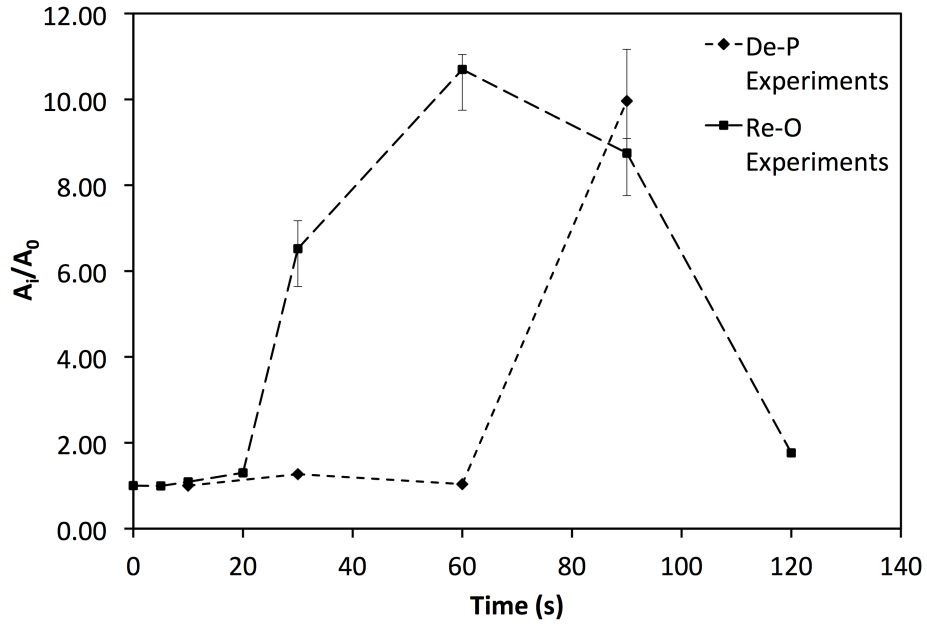


Figure 7.18: Normalized surface area of metal droplet as a function of time for both sets of experiments.

In addition to the mechanical removal of the particles, it was hypothesized that during the heating up of the sample in the CSLM, a film of iron oxide would also form around the solid metal. This "*shell*" would act as a slag so that, as soon as the drop melts, phosphorus would be chemically removed by reacting with the self-created oxide film, or slag. If this is true, the metal drop could go through "self dephosphorization" by two separate mechanisms as summarized below:

- CSLM Heating ramp:
  - During the heating ramp in the CSLM, FeO would form around the solid metal drop.
  - At the same time, the phosphorus rich particles would grow in the metal matrix as some form of a complex phosphate.
- Melting of the metal drop:

- The FeO film around the drop would melt at roughly the same time as the drop melts and would act as a slag to remove dephosphorize the metal.
- In parallel, the particles (possibly in liquid form) would simply float out of the metal drop into the slag and rapidly dissolve.

If the aforementioned mechanism is true, then the metal drop would not need a pre melted slag to undergo dephosphorization. To verify this assumption, an extra experiment was carried by submitting two Fe-P drops to the exact same experimental procedure as before, the only difference being the absence of the powdered, pre melted slag. The holding time used was 20 seconds which is in agreement with the reaction time before emulsification took place *and* after phosphorus had been removed from the metal. The sample was then mounted in epoxy, cross sectioned, mirror polished, coated with carbon and finally analyzed by WDS.

Interestingly enough, both drops had a significant amounts of particles entrapped in the matrix in a very similar fashion than what had been previously observed as shown in Figure 7.19. Moreover, the matrix still had considerable amounts of phosphorus. The WDS results are summarized in Table 7.16.

Based on these results, it is clear that phosphorus cannot be removed just due to mechanical removal and "self-dephosphorization" without the presence of a continuous slag phase. Therefore, phosphorus must have been removed due to mass transfer before the onset of emulsification.

### **Summary of Theories and Likely Mechanism**

Three theories to explain the observed results for the Fe-P experiments were discussed. The first theory explained why dephosphorization was thought to cause emulsification but was debunked as phosphorus had already been transferred to the slag before

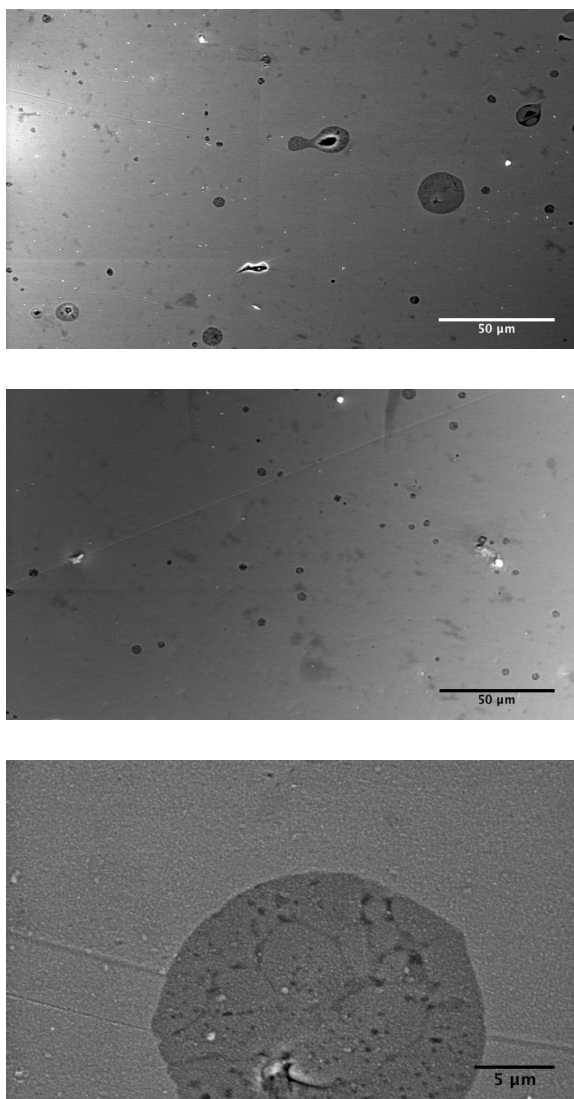


Figure 7.19: Secondary electron images of Fe-P alloy heated in the absence of slag to evaluate the "Self-Dephosphorization" theory.

Table 7.16: WDS results for Self De-P experiments

Sample	wt.% P	Area	kV	Spot Size	Fe Scan (s)	Fe Bkgd (s)	P Scan (s)	P Bkgd (s)
Drop 1	0.153	Bulk	25	6	60	40	100	80
Drop 1	0.139	Bulk	25	6	60	40	100	80
Drop 1	0.113	Bulk	25	6	60	40	100	80
Drop 1	0.157	Bulk	25	6	60	40	100	80
Drop 1	0.194	Bulk	25	6	60	40	100	80
Drop 1	0.786	Particle	25	6	60	40	100	80
Drop 1	2.548	Particle	25	6	60	40	100	80
Drop 1	1.433	Particle	25	6	60	40	100	80
Drop 1	3.321	Particle	25	6	60	40	100	80
Drop 2	0.120	Bulk	25	6	60	40	100	80
Drop 2	0.138	Bulk	25	6	60	40	100	80
Drop 2	0.170	Bulk	25	6	60	40	100	80
Drop 2	0.152	Bulk	25	6	60	40	100	80

emulsification. Phosphorus was removed in less than 5 seconds and based on the calculated interfacial area, it was possible to evaluate the lowest possible mass transfer coefficient of 0.025 cm/s. This value was then used to iteratively calculate the boundary layer thickness that would result in a reasonable “overall” diffusion coefficient. It was found that the boundary layer needed is less than 26 microns. The author then hypothesized how Marangoni flow can aid the other common convection mechanisms in order to achieve small boundary layers and rapid mass transfer.

The second theory examined why emulsification occurred after dephosphorization had already been completed. It was hypothesized that the early removal of phosphorus would also deplete the metal from oxygen. Thus, oxygen dissolution back into the metal would have to occur to restore the oxygen equilibrium between the metal and the slag. However, the SIMS measurements showed that the metal was actually over-saturated with oxygen right after dephosphorization took place. It remains a



mystery why this over saturation occurred in the first place. Nonetheless, this excess oxygen would now diffuse back into the slag which would then cause emulsification. Therefore, emulsification was not caused by *reoxidation* but rather by *de-oxidation*.

The third theory hypothesized that phosphorus was actually removed due to the flotation of the P-rich particles as well as by self-dephosphorization by the iron oxide film formed around the solid metal drop during heating in the CSLM. This FeO film would act as a slag and remove chemically remove phosphorus by means of oxidation. To test this theory the author studies two metal drops that were heated in the absence of slag. It was found that the drops did not “*self-dephosphorize*” neither the particles were removed by flotation. Thus, this theory was not consistent with the experimental results.

In summary, the author believes that the actual mechanism of the studied phenomenon is a combination of the first two theories as follows:

- Dephosphorization occurs rapidly by liquid phase mass transfer. Strong convection caused by a combination of several fluid flow mechanisms yields a very thin boundary that facilitates the phosphorus transport across the interface. It is plausible that Marangoni flow significantly aids the convection of the system in addition to the classic mechanisms of temperature, pressure and composition gradients.
- For an unknown reason, the metal becomes over saturated with oxygen after dephosphorization has happened. Thus, the metal phase de-oxidizes, transferring oxygen back to the slag in order to restore the oxygen equilibrium in the system. During this continuous transfer of oxygen, emulsification takes place. It is unclear why the time scales for De-P and De-O are considerably different.

### 7.5.3 Volume Measurements

The data from Table 7.7 and Figure 7.20 show that there is a total decrease of up to 27% in the initial droplet volume. This is expected, from de-oxidation reaction:



There should be a slight decrease in volume provided that for each atom of oxygen removed from the metal phase, 1 atom of metallic Fe is also removed. However, this decrease in volume is likely being exaggerated by the XCT method and its resolution may be the reason for this. As previously mentioned, the resulting voxel size for the XCT scans was about 5 microns this means that particles below this size will not be detected by XCT. Also, the grey value threshold was carried out on the cautious side. From Figure 7.21, it is possible to see that the iso-surface selected for the surface area and volume calculations cannot identify all small droplets present in the slag, specially when the contrast is not very good and the grey values that define the droplets and the slag are very close to each other. This is especially true for the highly emulsified samples corresponding to holding times of 30, 60 and 90 seconds. For these samples, the total volume is likely being significantly underestimated.

A similar behavior is seen for the oxidation experiments as shown in Figure 7.22, where a very similar volume decrease of 26% was observed. However, in the case of oxidation, it was expected a slight volume increase since both oxygen and iron are entering the metal. It is interesting to notice that the error bars are quite significant for the emulsified samples. Also interesting is that the volume measurements seem to be a lot more sensitive to the manually chosen grey values than the area measurements. This is easy to see just by looking at the size of the error bars for the area and volume measurements.

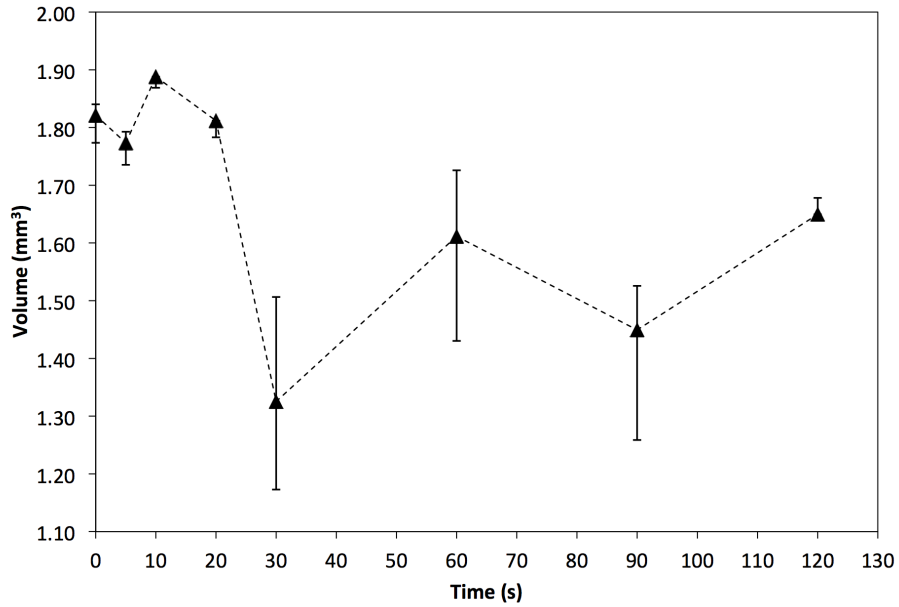
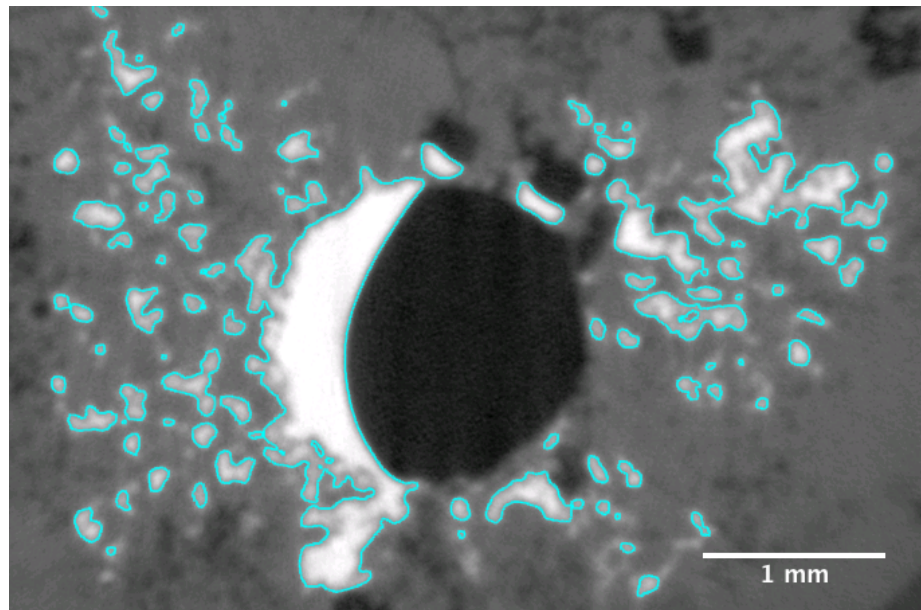


Figure 7.20: Measured droplet volume as a function of time.

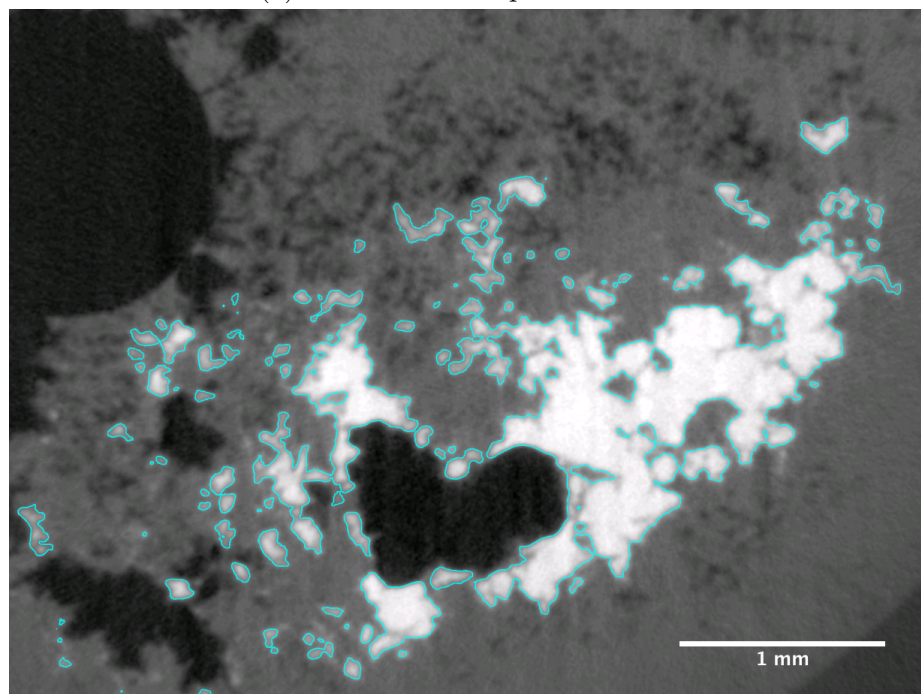
In summary, it seems that volume quantification for emulsified samples is not very reliable. The measured values are a lot more sensitive to the grey thresholds chosen. On the other hand, the area quantification showed error bars a lot more reasonable for the same grey values. The author believes that better volume measurements can be made with further optimization of the XCT parameters. This is encouraged in future studies using XCT.

#### 7.5.4 Coalescence of Emulsion

It is seen that from 60 seconds the dispersed droplets begin to recombine. With a reduction of near  $20 \text{ mm}^2$  in cumulative surface area between 60–90 seconds, and a further reduction of near  $60 \text{ mm}^2$  between 90–120 seconds (as seen in Figure 7.8). This points to the fact that after 60 seconds, the rate of the de-oxidation reaction is continuously decreasing. As the rate decreases, the transport of oxygen across the



(a) 30 Seconds Sample Isosurface



(b) 90 Seconds Sample Isosurface

Figure 7.21: Selected Isosurfaces for (a) 30 seconds sample and (b) 90 seconds sample.

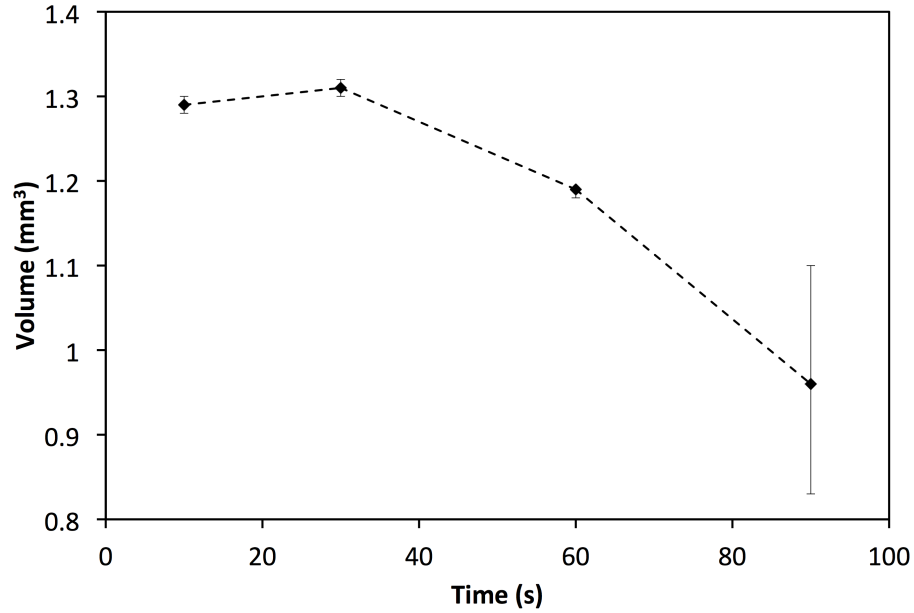


Figure 7.22: Measured droplet volume as a function of time for oxidation experiments.

metal-slag interface slows down and interfacial instabilities become less strong. The interfacial tension of the system gradually starts to increase providing the driving force for the recombination of droplets and minimization of interfacial area.

The surface area change is a clear nonlinear relation with respect to time. Firstly, the reason for this may be that de-oxidation is still occurring while recombination begins to take place, thus inhibiting some amount of coalescence. As well as this, a further contributing factor would be that of smaller droplets having less of an effect on the reduction of surface area than larger droplets when combining, thus as time progresses and larger droplets are present (due to several small droplets coming together), when these large droplets coalesce there will be a bigger change in surface area reduction. This behavioral trend is accounted for by film draining barriers and similarities to DVLO (Derjaguin-Landau-Verwey-Overbeek), which, in simple terms, states the electrostatic forces of smaller droplets force larger droplets to recombine

first. [69]

Similar to the error/gray scale thresholding being a possible explanation for the metal phase volume changes seen in Figure 7.20. This could also be accounted for by random coalescence of sub 5 micron droplets, that would be unable to coalesce before complete equilibrium of oxygen. This would be a purely statistical recombination, assuming this volume change is due to droplets operating under semi colloidal conditions (below the effects of gravity).

The branching recombination seen in Figure 7.5h is at this point thought to be due to local convection caused by coalescence draining, creating a favored and less dense area for the pathway of macro recombination. The discussion of the coalescence behavior of the droplets was made possible by Stephen Spooner.

## **Chapter 8**

# **Industrial Relevance, Conclusions and Potential Future Work**

This final chapter provides a brief discussion on the industrial relevance of the present work and proceeds to review and summarize of the main findings of Chapters 5, 6 and 7 and their respective hypothesis is revisited. The author then proposes potential future work that would help further develop the understanding of the phenomena studied.

### **8.1 Industrial Relevance of the Present Work**

Steel cleanliness is usually thought in terms of oxide inclusions, but the term can also be used when referring to impurities that can exist in solution. As new steel grades continue to be developed, the tolerance limits for impurities will become tighter and tighter. Iron sources containing low phosphorus are becoming less common and more expensive as older mines get used up. The recycling of steelmaking slags is also an attractive practice. In order to keep competitive prices and improve quality,

steelmakers will have to promote dephosphorization in a challenging environment where the process inputs have higher phosphorus but the final product must have even lower phosphorus than usual.

The findings of the present work have enabled better quantification of phosphorus equilibrium partition by the use of a rather simple equation (5.18). This is a valuable tool for the steelmaker in order to evaluate the performance of a furnace and identify possible strategies to enhance phosphorus removal. Additionally, the framework proposed on Chapter 6 can be easily applied to any steelmaking furnace to evaluate the degree of non-equilibrium as well as the influence of solid phases on furnace performance.

The major findings to aid steelmakers in removing phosphorus are as follows:

- Optimize slag compositions to increase the liquid fraction and reduce solid phases.
- Do not rely on simple measurements such as basicity to predict phosphorus removal, *i.e.* CaO has the largest effect on the predicted  $L_P$ .
- Beware that MgO solubility is higher than predicted by solution models.

The summary of findings, conclusions, hypothesis revisited and potential future work is discussed in the next sections.



## 8.2 Summary and Conclusions

### 8.2.1 Phosphorus Equilibrium Between Liquid Iron and CaO-MgO-SiO<sub>2</sub>-FeO-P<sub>2</sub>O<sub>5</sub> Slags

Chapter 5 provided an in-depth look at phosphorus equilibrium between liquid iron and steelmaking slags. The experimental apparatus was described in detail and the considerably longer equilibration time of 10 hours was highlighted. The software FactSage was used to help design the slags and two Fe-P master alloys containing different phosphorus contents were used. Phosphorus was transferred from both sides, *i.e.* from metal to slag and slag to metal, for most of the compositions studied. The conclusions are as follows:

- The new proposed correlation combining Tayeb's [2], the present work data and Suito's data is believed to be a significant improvement over previous correlations.
- The highly basic liquid slags studied are capable of promoting extensive dephosphorization of liquid iron.
- $L_P$  does not appear to be a clear function of binary basicity for ratios above 2.5.
- The effect of P<sub>2</sub>O<sub>5</sub> maybe being overestimated as it was evaluated over a relatively narrow compositional range.
- The impact of FeO as a reactant on  $L_P$  in the present work was found to be relatively small compared to other experimental uncertainties.

- The MgO saturation predicted by FactSage appears to be considerably lower than the ones observed in the present work by up to a factor of 2.

### 8.2.2 Plan Data Analysis

Chapter 6 studied four individual furnaces: one AOD, two BOF's and one Q-BOP or OBM. The data consisted of the turndown metal and slag composition and turndown temperature. FactSage was used to correct the bulk slag compositions for possible solid phases including, CaO and MgO solid solutions and  $2\text{CaO} \cdot \text{SiO}_2$ . In total, close to 1800 heats were studied. The highlights and conclusion are as follows:

- None of the studied furnaces achieved thermodynamic equilibrium with respect to phosphorus.
- The AOD is the reactor closest to equilibrium followed by the Q-BOP, BOF 1 and BOF 2.
- The underestimation of MgO saturation by FactSage was found to be less significant and did not alter the analysis of the results significantly.
- The two extreme cases of the impact of dicalcium silicate showed that, in theory,  $\text{C}_2\text{S}$  could have significant impact on  $L_P$  if thermodynamic equilibrium between the slag and  $\text{C}_2\text{S}$  is achieved. However, it is unlikely that equilibrium is achieved.

### 8.2.3 Studies on Spontaneous Emulsification

Chapter 7 provided some detailed information on a phenomenon that is still not fully understood: spontaneous emulsification. The experimental setup was described and the use of the CSLM as a fast-heating/fast-cooling furnace was explained. Two sets of experiments were carried out: one with a Fe-P alloy and another with a P-free

alloy containing low oxygen. The use of XCT to study the dynamic area changes was proposed and justified based on its excellent resolution and nondestructive characteristics. The highlights and conclusions are as follows:

- Phosphorus was removed from the metal drop before the onset of emulsification; within a period of 0 to 5 seconds.
- Fast phosphorus removal is likely related to strong convection inside the metal droplet as a combination of several fluid flow mechanisms that result in a very thin boundary layer.
- Liquid phase mass transfer of oxygen alone appears to be responsible for spontaneous emulsification in the systems studied, independently of the direction of transfer, *i.e.* de-oxidation or re-oxidation.
- XCT is a suitable technique to quantify surface area in quenched metal-slag samples as long as sufficient difference in contrast between the phases exist.
- Volume measurements from XCT seem to be less relevant than initially thought due to large uncertainties for the emulsified samples.
- The coalescence behavior of the droplets is likely to occur while oxygen transfer is still taking place but at a slower rate.

## 8.3 Hypotheses Revisited

### 8.3.1 Phosphorus Equilibrium

The hypothesis for the equilibrium studies, quoted from Chapter 4, was the following:

*“The disagreements in the available data for phosphorus equilibrium can be resolved by careful study including approaching equilibrium from both sides of the system and ensuring liquid slags.”*

The hypothesis was proven to be mostly correct. Approaching equilibrium from both sides of the reaction is a very good way to analyze whether thermodynamic equilibrium is achieved or not. Good agreement was found for most of the samples as seen in Figure 5.10 and 10 hours of holding time seems to ensure thermodynamic equilibrium. However, the analyzes of very low phosphorus contents in the metal proved to be a challenge and at extreme low concentrations the uncertainty can be larger than the measurement. The phosphorus partition for both directions of phosphorus transfer is not *exactly* the same but reasonably close due to FeO being a reactant. The combination of the present work data, Tayeb’s and Suito’s data has yielded a new correlation designed specifically for EAF- and BOF-type slags and is believed to be a significant improvement on the prediction of the equilibrium phosphorus partition between liquid iron and slags.

### 8.3.2 Plant Data

The hypothesis for the analysis of plant data, quoted from Chapter 4, was the following:

*“Phosphorus equilibrium is not achieved in regular plant operation and it is limited by liquid phase mass transfer.”*

From Figure 6.10, it can be seen that most of the data does not correspond to thermodynamic equilibrium. Liquid phase mass transfer definitely plays a significant role and it is closely linked with the slag composition and the possible undissolved oxides present in the slag. A major factor is they the final liquid slag composition is

not achieved until late in the process. Close monitoring of these two variables should be used for process optimization following the guidelines provided in Section 6.4.

### 8.3.3 Emulsification

From Chapter 4, the hypothesis for the metal droplet behavior portion of the present work was:

*“The kinetics of dephosphorization is limited by liquid phase mass transfer of both metal and slag phases. Due to spontaneous emulsification, the reaction area greatly increases in the early stages of mass transfer.”*

This hypothesis was proved to be inadequate for the experimental observations described in Chapter 7. Phosphorus was removed from the metal before the onset of emulsification and did not play a role in the dynamic interfacial behavior observed in the experiments by XCT. The emulsification behavior was probably the result of oxygen transfer alone due to de-oxidation after the metal drop became over saturated with oxygen by an unknown reason. This was further confirmed by the second set of experiments where re-oxidation was studied in a phosphorus-free system. Thus, phosphorus kinetics was not studied as originally intended, but rather whether oxygen transfer alone could cause spontaneous emulsification.

### 8.3.4 Potential Future Work

The author believes there is a lot of room for further development on understanding the topics discussed in this manuscript. Ideas for future work are only limited by one’s imagination. However, here are a few suggestions for future research projects related to the present work.

- Study of the phosphorus partition between slag and dicalcium silicate in indus-

trial furnaces. As previously discussed in Chapter 6, the effect of  $C_2S$  was shown for the extreme cases, *i.e.* no effect at all and full thermodynamic equilibrium. The real effect on industrial furnaces must be within these two scenarios and is currently unknown.

- Study of slag-path, slag formation and the degree of non-equilibrium with respect to phosphorus in industrial furnaces as a function of time.
- Spontaneous emulsification of in systems without oxygen transfer.
- Spontaneous emulsification as a function of oxygen activity in the slag.
- Effect of alumina on phosphorus equilibrium partition for BOF-type slags.
- Further study on the effect of  $MgO$  on phosphorus equilibrium partition similar to what was done by Ide et al. [27]. This would enable better quantification of the  $MgO$  coefficient on the correlation proposed in Chapter 5.
- Spontaneous emulsification in  $Fe-O-S$  systems to study how the presence of another surface active element could be used to control spontaneous emulsification.
- Study the De-P behavior of a metal drop in smaller time scales. The use of second-by-second experiments would help understand how phosphorus was removed so readily from the metal as previously shown in Chapter 7.
- Spontaneous emulsification as a function of oxygen activity in the slag.

The proposed studies are just a few of many that could evolve from the present work. The author encourages future researches to consider these topics to help further understand high temperature processing and the fundamentals of steelmaking.

# Bibliography

- [1] RJ Fruehan. *The Making, Shaping, and Treating of Steel*. AISE Steel Foundation Pittsburgh, PA, USA, 1998.
- [2] Mohammed A. Tayeb, Richard J. Fruehan, and Seetharaman Sridhar. Dephosphorization in the DRI-EAF Steelmaking and the Effect of Alumina. Technical report, 2014.
- [3] Wordsteel.org. Overview of the Steelmaking Process. <http://www.worldsteel.org/dms/internetDocumentList/bookshop/Steelmaking-poster/document/Overview%20of%20the%20steelmaking%20process.pdf>, May 2013.
- [4] International Monetary Fund. Iron Ore Monthly Price - US cents per Dry Metric Ton. 2011.
- [5] MS Millman, A Kapilashrami, M Bramming, and D Malmberg. *Imphos: Improving Phosphorus Refining*. European Union, Luxembourg, 2011.
- [6] Christopher P Manning and Richard J Fruehan. The Rate of the Phosphorous Reaction Between Liquid Iron and Slag. *Metallurgical and Materials Transactions B*, 44(1):37–44, 2013.

- [7] H Gaye, LD Lucas, M Olette, and PV Riboud. Metal-Slag Interfacial Properties: Equilibrium Values and “Dynamic” Phenomena. *Canadian Metallurgical Quarterly*, 23(2):179–191, 1984.
- [8] K Ogino, S Hara, T Miwa, and S Kimoto. The Effect of Oxygen Content in Molten Steel on the Interfacial Tension between Molten Steel and Slag. *Tetsu-to-Hagane(Journal of the Iron and Steel Institute of Japan)*, 65(14):2012–2021, 1979.
- [9] A Jakobsson, M Nasu, J Mangwiri, KC Mills, and S Seetharaman. Interfacial Tension Effects on Slag-Metal Reactions. *PHILOSOPHICAL TRANSACTIONS-ROYAL SOCIETY OF LONDON SERIES A MATHEMATICAL PHYSICAL AND ENGINEERING SCIENCES*, pages 995–1002, 1998.
- [10] H. Suito, R. INOUE, and M.I. Takada. Phosphorus Distribution between Liquid Iron and MgO Saturated Slags of the System  $\text{CaO-MgO-FeO}_x\text{-SiO}_2$ . *Transactions of the Iron and Steel Institute of Japan*, 21(4):250–259, 1981.
- [11] H. Suito and R. Inoue. Phosphorus Distribution between MgO-saturated  $\text{CaO-Fe}_t\text{O-SiO}_2\text{-P}_2\text{O}_5\text{-MnO}$  Slags and Liquid Iron. *Transactions of the Iron and Steel Institute of Japan*, 24(1):40–46, 1984.
- [12] S Basu, AK Lahiri, and S Seetharaman. Phosphorus Partition Between Liquid Steel and  $\text{CaO-SiO}_2\text{-2-FeO}_x\text{-P-2O}_5\text{-MgO}$  Slag Containing 15 to 25 pct FeO. *Metall Mater Trans B*, 38(4):623–630, 2007.
- [13] S Basu, AK Lahiri, and S Seetharaman. Phosphorus Partition between Liquid Steel and  $\text{CaO-SiO}_2\text{-P}_2\text{O}_5\text{-MgO}$  Slag Containing Low FeO. *Metall Mater Trans B*, 38(3):357–366, 2007.



- [14] BJ Keene, KC Mills, and M Susa. *Slag Atlas*. Dusseldorf, Germany: Verlag Stahleisen, 1995.
- [15] Praxair. Aod Diagram. [http://www.praxair.com/praxair.nsf/7a1106cc7ce1c54e85256a9c005accd7/48740df62f17eb22852569de007457cc!](http://www.praxair.com/praxair.nsf/7a1106cc7ce1c54e85256a9c005accd7/48740df62f17eb22852569de007457cc!OpenDocument) OpenDocument, January 2013.
- [16] Steel University. Bof Diagram. <http://steeluniversity.org/content/html/eng/default.asp?catid=24&pageid=2081272084>, January 2013.
- [17] Steel University. Q-BOP Diagram. <http://steeluniversity.org/content/html/eng/default.asp?catid=24&pageid=2081272084>, January 2013.
- [18] Ryo Inoue and Hideaki Suito. Phosphorous Partition between  $2\text{CaO} \cdot \text{SiO}_2$  Particles and  $\text{CaO} \cdot \text{SiO}_2 \cdot \text{Fe}_t\text{O}$  Slags. *ISIJ international*, 46(2):174–179, 2006.
- [19] William T Lankford. *The Making, Shaping, and Treating of Steel*. Association of Iron & Steel Engineers, Pittsburgh, 1985.
- [20] T. A. Bloom, D. R. Fosnacht, and D. M. Haezebrouck. The Influence of Phosphorus on the Properties of Sheet Steel Products and Methods Used to Control Steel Phosphorus Levels in Steel Product Manufacturing. i. *Iron and Steelmaker*, 17(9):35–41, 1990.
- [21] Rainer Hüsken, Robert Fechner, and Jürgen Cappel. Use of Hot Metal with High Phosphorous Content in Combined Blowing BOF Converters. *Iron & Steel Technology*, Vol. 8, No. 11:46–57, 2011.
- [22] S Basu, AK Lahiri, and S Seetharaman. A Model for Activity Coefficient of  $\text{P}_2\text{O}_5$  in BOF Slag and Phosphorus Distribution between Liquid Steel and Slag. *Isij Int*, 47(8):1236–1238, 2007.

- [23] T Emi. Toward Future Development: Pros and Cons of Ironmaking and Steel-making Slags and Mold Fluxes. *High Temp Mat Pr-isr*, 20(3-4):167–184, 2001.
- [24] H. Ishii and RJ Fruehan. Dephosphorization Equilibria between Liquid Iron and Highly Basic CaO-based slags saturated with MgO. *Iron & steelmaker*, 24(2):47–54, 1997.
- [25] K. Balajiva and P. Vajragupta. The Effect of Temperature on the Phosphorus Reaction in the Basic Steelmaking Process. *J. Iron and Steel Inst*, 155:563–567, 1946.
- [26] T.B. Winkler and J. Chipman. An Equilibrium Study of the Distribution of Phosphorus between Liquid Iron and Basic Slags. *Trans Aime*, 167:111–133, 1946.
- [27] K. Ide and RJ Fruehan. Evaluation of Phosphorus Reaction Equilibrium in Steelmaking. *Iron & steelmaker*, 27(12):65–70, 2000.
- [28] ET Turkdogan and J. Pearson. Activities of Constituents of Iron and Steelmaking Slags. *Jour. Iron and Steel Inst*, 175:393–401, 1953.
- [29] H. Suito and R. Inoue. Effect of Calcium Fluoride on Phosphorus Distribution between MgO Saturated Slags of the System  $\text{CaO-MgO-FeO}_x\text{-SiO}_2$  and Liquid Iron. *Transactions of the Iron and Steel Institute of Japan*, 22(11):869–877, 1982.
- [30] H. Suito and R. Inoue. Effects of  $\text{Na}_2\text{O}$  and  $\text{BaO}$  Additions on Phosphorus Distribution between  $\text{CaO-MgO-Fe}_t\text{O-SiO}_2$  Slags and Liquid Iron. *Transactions of the Iron and Steel Institute of Japan*, 24(1):47–53, 1984.

- [31] XF Zhang, ID Sommerville, and JM Tiger. An Equation for the Equilibrium Distribution of Phosphorus between Basic Slags and Steel. *ISS Transactions*, 6:29–33, 1985.
- [32] H Flood, T Forland, and K Grjotheim. *The Physical Chemistry of Melts*. 1953.
- [33] K Grjotheim and MK Brun. Application of the Flood-Grjotheim Thermodynamic Treatment to the Slag-Metal Equilibria. *Canadian Metallurgical Quarterly*, 16(1):161–165, 1977.
- [34] CM Lee and RJ Fruehan. Phosphorus Equilibrium between Hot Metal and Slag. *Ironmaking & steelmaking*, 32(6):503–508, 2005.
- [35] ET Turkdogan. Assessment of  $P_2O_5$  Activity Coefficients in Molten Slags. *ISIJ international*, 40(10):964–970, 2000.
- [36] CR Taylor and J. Chipman. Equilibria of Liquid Iron and Simple Basic and Acid Slags in a Rotating Induction Furnace. *Trans. AIME*, 154:228–247, 1943.
- [37] Xue-Min Yang, Jian-Ping Duan, Cheng-Bin Shi, Meng Zhang, Yong-Liang Zhang, and Jian-Chang Wang. A Thermodynamic Model of Phosphorus Distribution Ratio between  $CaO-SiO_2-MgO-FeO-Fe_2O_3-MnO-Al_2O_3-P_2O_5$  Slags and Molten Steel during a Top–Bottom Combined Blown Converter Steelmaking Process Based on the Ion and Molecule Coexistence Theory. *Metallurgical and Materials Transactions B*, 42(4):738–770, 2011.
- [38] Ryo Inoue and Hideaki Suito. Mechanism of Dephosphorization with  $CaO-SiO_2-Fe_tO$  Slags Containing Mesoscopic Scale  $2CaO.SiO_2$  Particles. *ISIJ international*, 46(2):188–194, 2006.

- [39] Farshid Pahlevani, Shin-ya Kitamura, Hiroyuki Shibata, and Nobuhiro Maruoka. Distribution of  $P_2O_5$  between Solid Solution of  $2CaO \cdot SiO_2 \cdot 3CaO \cdot P_2O_5$  and Liquid Phase. *ISIJ international*, 50(6):822–829, 2010.
- [40] Hideaki Suito and Ryo Inoue. Behavior of Phosphorous Transfer from  $CaO \cdot Fe_tO \cdot P_2O_5$  ( $-SiO_2$ ) Slag to  $CaO$  Particles. *ISIJ international*, 46(2):180–187, 2006.
- [41] Shin-ya Kitamura, Shinya Saito, Keita Utagawa, Hiroyuki Shibata, and David GC Robertson. Mass Transfer of  $P_2O_5$  between Liquid Slag and Solid Solution of  $2CaO \cdot SiO_2$  and  $3CaO \cdot P_2O_5$ . *ISIJ international*, 49(12):1838–1844, 2009.
- [42] Shin-ya Kitamura, Hiroyuki Shibata, Ken-ichi Shimauchi, and Shin-ya Saito. The Importance of Dicalcium-Silicate on Hot Metal Dephosphorization Reaction. *REVUE DE METALLURGIE CAHIERS D INFORMATIONS TECHNIQUES*, 105(5):263, 2008.
- [43] ET Turkdogan. *Fundamentals of Steelmaking*. Institute of Materials London, 1996.
- [44] Brahma Deo and Rob Boom. *Fundamentals of Steelmaking Metallurgy*. Prentice Hall International New York, NY, 1993.
- [45] AI Van Hoorn, JT Van Konijnenburgh, and PJ Kreijger. The Role of Slag in Basic Oxygen Steelmaking Processes. 1976.
- [46] Neslihan Dogan, Geoffrey A Brooks, and Muhammad Akbar Rhamdhani. Kinetics of Flux Dissolution in Oxygen Steelmaking. *ISIJ international*, 49(10):1474–1482, 2009.

- [47] GA Brooks, KS Coley, and GA Irons. Generation of Droplets in Slag-Metal Emulsions through Top Gas Blowing. *ISIJ international*, 43(7):983–989, 2003.
- [48] Geoffrey Brooks, Yuhua Pan, and Ken Coley. Modeling of Trajectory and Residence Time of Metal Droplets in Slag-Metal-Gas Emulsions in Oxygen Steelmaking. *Metallurgical and Materials Transactions B*, 36(4):525–535, 2005.
- [49] Neslihan Dogan, Geoffrey Brooks, and Muhammad Akbar Rhamdhani. Analysis of Droplet Generation in Oxygen Steelmaking. *ISIJ international*, 49(1):24–28, 2009.
- [50] Qing Lin He and Nicholas Standish. A Model Study of Droplet Generation in the BOF Steelmaking. *ISIJ International*, 30(4):305–309, 1990.
- [51] D-J Min and RJ Fruehan. Rate of Reduction of FeO in Slag by Fe-C Drops. *Metallurgical Transactions B*, 23(1):29–37, 1992.
- [52] Satish C Koria and Klaus W Lange. A New Approach to Investigate the Drop Size Distribution in Basic Oxygen Steelmaking. *Metallurgical Transactions B*, 15(1):109–116, 1984.
- [53] CL Molloyseau and RJ Fruehan. The Reaction Behavior of Fe-C-S Droplets in CaO-SiO<sub>2</sub>-MgO-FeO Slags. *Metallurgical and Materials Transactions B*, 33(3):335–344, 2002.
- [54] BJ Monaghan, RJ Pomfret, and KS Coley. The Kinetics of Dephosphorization of Carbon-saturated Iron using an Oxidizing Slag. *Metallurgical and Materials Transactions B*, 29(1):111–118, 1998.

- [55] Y Chung and AW Cramb. Dynamic and Equilibrium Interfacial Phenomena in Liquid Steel-Slag Systems. *Metallurgical and Materials Transactions B*, 31(5):957–971, 2000.
- [56] Hermann Lux. “acids” and “bases” in a fused salt bath: the determination of oxygen-ion concentration. *Z. Elektrochem. Soc.*, (45):303–310, 1939.
- [57] H Flood and T Förland. The acidic and basic properties of oxides. *Acta Chem. Scand*, 1:592–604, 1947.
- [58] G Tromel, K Koch, W Fix, and N Grosskurth. The Influence of Magnesium Oxide on Equilibrium in the System MgO-CaO-FeO-SiO<sub>2</sub> and on Sulphur Partition at 1600 c. *Archiv. Eisenhutten*, 40(121):969–978, 1969.
- [59] A. N. Assis and R. J. Fruehan. Phosphorus Removal in Oxygen Steelmaking: A Comparison Between Plant and Laboratory Data. *AISTech 2013 Proceedings*, pages 889–895, 2013.
- [60] Juan Carlos López-Montilla, Paulo Emilio Herrera-Morales, Samir Pandey, and Dinesh O Shah. Spontaneous emulsification: mechanisms, physicochemical aspects, modeling, and applications. *Journal of dispersion science and technology*, 23(1-3):219–268, 2002.
- [61] MA Rhamdhani, KS Coley, and GA Brooks. Analysis of the source of dynamic interfacial phenomena during reaction between metal droplets and slag. *Metallurgical and Materials Transactions B*, 36(5):591–604, 2005.
- [62] MA Rhamdhani, KS Coley, and GA Brooks. Kinetics of metal/slag reactions during spontaneous emulsification. *Metallurgical and Materials Transactions B*, 36(2):219–227, 2005.

- [63] MA Rhamdhani, GA Brooks, and KS Coley. Analysis of interfacial area changes during spontaneous emulsification of metal droplets in slag. *Metallurgical and Materials Transactions B*, 37(6):1087–1091, 2006.
- [64] J Crank. *The mathematics of diffusion*. Clarendon Press Oxford, 1975.
- [65] LA Feldkamp, LC Davis, and JW Kress. Practical cone-beam algorithm. *JOSA A*, 1(6):612–619, 1984.
- [66] Jagadeesha Kumar, Alex Attridge, PKC Wood, and Mark A Williams. Analysis of the effect of cone-beam geometry and test object configuration on the measurement accuracy of a computed tomography scanner used for dimensional measurement. *Measurement Science and Technology*, 22(3):035105, 2011.
- [67] *A reference workpiece for voxel size correction in x-ray computed tomography*, volume International Conference on Optics in Precision Engineering and Nanotechnology (icOPEN2013). International Society for Optics and Photonics, 2013.
- [68] Jagadeesha Kumar, Abdul Hadi G Abulrub, Alex Attridge, and Mark A Williams. Effect of x-ray computed tomography scanning parameters on the estimated porosity of foam specimens. *Applied Mechanics and Materials*, 110:808–815, 2012.
- [69] Subir Bhattacharjee, Menachem Elimelech, and Michal Borkovec. Dlvo interaction between colloidal particles: beyond derjaguin’s approximation. *Croatica Chemica Acta*, 71:883–903, 1998.